

# The Stellar Population of h and $\chi$ Persei: Cluster Properties, Membership, and the Intrinsic Colors and Temperatures of Stars

Thayne Currie<sup>1,7</sup>, Jesus Hernandez<sup>2</sup>, Jonathan Irwin<sup>1,3</sup>, Scott J. Kenyon<sup>1</sup>, Susan Tokarz<sup>1</sup>,  
Zoltan Balog<sup>4</sup>, Ann Bragg<sup>5</sup>, Perry Berlind<sup>6</sup>, and Mike Calkins<sup>6</sup>

tcurrie@cfa.harvard.edu, jhernan@umich.edu, jirwin@cfa.harvard.edu

## ABSTRACT

From photometric observations of  $\sim 47,000$  stars and spectroscopy of  $\sim 11,000$  stars, we describe the first extensive study of the stellar population of the famous Double Cluster, h and  $\chi$  Persei, down to subsolar masses. By analyzing optical spectra and optical/infrared photometry, we constrain the distance moduli (dM), reddening (E(B-V)), and ages for h Persei,  $\chi$  Persei and the low-density halo population surrounding both cluster cores. With the exception of mass and spatial distribution, the clusters are nearly identical in every measurable way. Both clusters have E(B-V)  $\sim 0.52$ – $0.55$  and dM = 11.8–11.85; the halo population, while more poorly constrained, likely has identical properties. As determined from the main sequence turnoff, the luminosity of M supergiants, and pre-main sequence isochrones, ages for h Persei,  $\chi$  Persei and the halo population all converge on  $\approx 14$  Myr, thus showing a stunning agreement between estimates based on entirely different physics. From these data, we establish the first spectroscopic and photometric membership lists of cluster stars down to early/mid M dwarfs. At minimum, there are  $\sim 5,000$  members within  $10'$  of the cluster centers, while the entire h and  $\chi$  Persei region has at least  $\sim 13,000$  and as many as 20,000 members. The Double Cluster contains  $\approx 8,400 M_{\odot}$  of stars within  $10'$  of the

---

<sup>1</sup>Harvard-Smithsonian Center for Astrophysics, 60 Garden St. Cambridge, MA 02140

<sup>2</sup>Centro de Investigaciones de Astronomica (CIDA), Apdo. Postal 264, Merida 5101-A, Venezuela

<sup>3</sup>Institute of Astronomy, University of Cambridge

<sup>4</sup>MPIA-Heidelberg

<sup>5</sup>Department of Physics, Marietta College

<sup>6</sup>Fred Lawrence Whipple Observatory

<sup>7</sup>NASA-Goddard Space Flight Center

cluster centers. We estimate a total mass of at least 20,000  $M_{\odot}$ . We conclude our study by outlining outstanding questions regarding the past and present properties of  $\eta$  and  $\chi$  Persei. From comparing recent work, we compile a list of intrinsic colors and derive a new effective temperature scale for O–M dwarfs, giants, and supergiants.

*Subject headings:* stars: pre-main sequence – Galaxy: Open Clusters and Associations: Individual: NGC Number: NGC 869, Galaxy: Open Clusters and Associations: Individual: NGC Number: NGC 884

## 1. Introduction

Known and studied for the past two centuries and perhaps since ancient times, the Double Cluster –  $\eta$  and  $\chi$  Persei – presents a rare opportunity to precisely study multiple stages of stellar evolution. The Double Cluster is located in the Perseus spiral arm and contains an exceptionally high density of evolved stars – red supergiants and B giants/supergiants – and early B-type dwarfs, indicating that the cluster is young,  $\lesssim 30$  Myr old (cf. Humphreys 1978). This huge sample of high-mass stars probes post-main sequence stellar evolution, specifically the main sequence turnoff and the evolution of M supergiants. For any reasonable initial mass function (e.g. Miller-Scalo),  $\eta$  and  $\chi$  Persei must also have thousands of solar/subsolar-mass members, which allow probes of pre-main sequence evolution.

Derived post main sequence and pre-main sequence *ages* for stars in  $\eta$  and  $\chi$  Persei are an acid test for stellar evolution models and critically affect conclusions about planet formation. Because all stars in Gyr-old clusters have reached the main sequence, their ages are derived from comparing the main sequence turnoff and the luminosities of giants/supergiants with predictions from post-main sequence isochrones. In young clusters, high-mass stars are typically too few in number to derive post-main sequence ages. Thus, ages for young,  $\lesssim 50$  Myr-old clusters are almost always derived from fitting pre-main sequence isochrones to color-magnitude diagrams (e.g. Mayne et al. 2007). However, if post and pre-main sequence age estimates for young, populous clusters significantly disagree, it is not clear that either estimate for any cluster should be considered accurate. Furthermore, the lack of a reliable absolute age calibration impedes attempts to use circumstellar disk population statistics for different clusters to constrain planet formation empirically and prevents strong comparisons with solar system chronology and models of planet formation (e.g. Hernandez et al. 2007a; Currie et al. 2010; Castillo-Rogez et al. 2007; Kenyon and Bromley 2009).

An extensive study of  $\eta$  and  $\chi$  Persei from early type, high-mass stars to late type,

low-mass stars also addresses issues specific to the Double Cluster. Chief among these issues is membership: formal lists are currently limited to B type dwarfs, giants, and supergiants; A–K supergiants; some stars showing evidence for circumstellar gas accretion or luminous debris disk emission; and x-ray luminous stars (Uribe et al. 2002; Slesnick et al. 2002; Bragg and Kenyon 2005; Currie et al. 2007b,c, 2008a, 2009a). A more uniform membership list would yield better estimates for the cluster mass function, constrain the spatial distribution of stars, and provide a reliable census from which to constrain models of star and planet formation.

In this paper, we describe the first exhaustive photometric and spectroscopic survey of h and  $\chi$  Persei down to subsolar masses. Comprised of optical photometry for  $\sim 47,000$  stars and spectra for  $\sim 11,000$ , our survey strongly constrains cluster properties – reddening, distance, age, and structure – and produces the first membership list for the Double Cluster that includes main sequence and pre-main sequence stars. §2 describes our data acquisition, image processing, and basic photometry/spectroscopic analysis. §3 yields distance and pre/post-main sequence age estimates for each component of the Double Cluster: the h Persei core, the  $\chi$  Persei core, and the low-density halo population surrounding both cores. In §4, we use the results of previous sections to identify h and  $\chi$  Persei members based on spectroscopy and identify probable members based on photometry. With a membership catalog, we investigate other cluster properties in §5 such as the spatial distribution of members, the cluster mass function, and mass segregation. In §6, we summarize our results, discuss outstanding questions regarding h and  $\chi$  Per, and suggest fruitful future research programs. The Appendix lists a new effective temperature scale and intrinsic colors for O–M dwarfs, giants, and supergiants.

## 2. Data

### 2.1. Optical Photometry

#### 2.1.1. Observations, Image Processing, and Photometry

Optical VI photometry of h and  $\chi$  Persei were taken with the Mosaic Imager at the 4-meter Mayall telescope at the Kitt Peak National Observatory on October 13-16 and 27-30, 2006, as a part of the MONITOR project (Aigrain et al. 2007). Observing conditions were photometric with  $\sim 0.9''$ – $1.0''$  natural seeing in V and I. Exposures in Harris V band and Sloan i' band were taken using 2, 75, and 300 (2 and 75) second integrations with a  $36' \times 36'$  field of view centered on  $2^h 18^m 55.9^s, 57^\circ 8' 25''$  for h Persei and  $2^h 22^m 5.8^s, 57^\circ 8' 43''$  for  $\chi$  Persei. These positions are comparable to the cluster centers determined by

Bragg and Kenyon (2005), which we will adopt in this paper:  $h$  Persei<sub>center</sub> =  $2^h 18^m 56.4^s$ ,  $57^\circ 8' 25''$ ,  $\chi$  Persei<sub>center</sub> =  $2^h 22^m 4.3^s$ ,  $57^\circ 8' 35''$ . Because the clusters are separated by  $\approx 27$  arc-minutes, the total effective area of coverage is slightly smaller,  $\approx 0.6$  square degrees. The 75-second  $i'$  band exposures were repeated 24 times, yielding a total integration time of 1800s, and combined together into an averaged frame with outlier rejection to match the  $i'$  band sensitivity to V band. The data were reduced using the pipeline for the INT wide-field survey (Irwin and Lewis 2001; Irwin et al. 2007), corrected for the effects of cross-talk, bias subtracted, and flatfielded using median-combined twilight flats.

For source detection, we used the crowded field algorithm of Irwin (1985), requiring a minimum of 4 connected pixels lying each  $1.5\sigma$  above the sky. Photometry was performed following the method of Irwin et al. (2007). Aperture photometry is used for unblended sources; a series of aperture radii ranging from  $\sim 1''$  to  $2''$  are used to compute the source flux. Aperture corrections were derived from a curve-of-growth analysis as described in Irwin and Lewis (2001). Photometry for blended sources (sources with overlapping isophotes) is done by simultaneously fitting circular top-hat functions to the overlapping sources. Background estimation is made by computing the background level binned in a  $64 \times 64$  pixel grid using a robust background estimator in each bin, which is then filtered using 2D bilinear and median filters as described in Irwin (1985) and Irwin et al. (2007) and references therein.

Initial photometric calibration was made by observing Landolt standard stars before and after  $h$  and  $\chi$  Per observations. Our method for converting from instrumental to standard magnitudes in the Johnson-Cousins system follows that of Mayne et al. (2007). As an initial guess for color transformations, we chose the V and  $i$  color transformations for the Mosaice II imager, which has an identical Sloan  $i'$  filter and similar V-band filter. To fine-tune the color transformations, we compared photometry taken with M34, observed immediately after  $h$  and  $\chi$  Per, with published  $VI_c$  M34 photometry taken at the Isaac Newton Telescope (Irwin et al. 2006) and VI photometry of  $h$  and  $\chi$  Persei from Mayne et al. (2007). The transformations from  $i_{instr.}$  to I were identical to those for the Mosaic II imager; those for  $V_{instr.}$  to V differed slightly, producing a change in V-I of  $\approx 0.5$ – $5\%$  for stars with V-I  $\sim -1$ – $-3$ . Comparisons between our data and both the Mayne et al. (2007)  $h$  and  $\chi$  Per data and the Irwin et al. (2006) M34 data fail to identify any residual color-dependent offsets indicative of errors in the Harris/Sloan to Johnson-Cousins color transformations for either set.

To identify and correct  $\sim 1\%$  level chip-to-chip offsets, two of us (J.I. and T.C.) cross-correlated photometry for a subsample of 11,000 stars as a function of chip position and exposure time with deep VI photometry of  $h$  and  $\chi$  Persei stars from Mayne et al. (2007) with  $5$ – $10\sigma$  detections. While their photometry is slightly shallower than ours ( $V(5\sigma) \sim 22$ ), their photometry draws from CCD observations with multiple exposure times using a larger

chip area, which allows us to identify small zero-point uncertainties in each exposure time and any systematic offsets due to chip-to-chip variations. The chip-to-chip level offsets were identified and corrected for using a reduced  $\chi^2$  fit.

### 2.1.2. Saturation and Completeness

The initial photometric catalog has roughly 52,000 candidate sources detected in at least one filter for at least one exposure time. To remove sources with bad photometry, we check each star for blending, check stars for contamination from image artifacts (e.g. diffraction spikes from nearby bright stars), and identify stars with point-spread functions indicative of saturation. By comparing the photometry from different exposure times, we empirically identify a saturation limit of  $V \sim 15$  and  $16.5$  for  $t=75s$  and  $300s$  exposures and  $I \sim 15.5$  for  $t=75s$ . The saturation limit for the shortest V band exposures ( $t = 2s$ ) is  $V \sim 11$  (see §2.1.3). Photometry for saturated stars were then flagged and removed from the catalog, while blends and contaminated stars were identified. Priority was given to stars lacking contamination or blending flags regardless of rms errors. Otherwise, the photometry for the final catalog was selected from the exposure that yielded the smallest rms errors.

The final catalog lists 47,060 stars with detections in both filters. Of these, we use photometry derived from the longest exposures (300s for V band, 75s for I band) for  $\sim 90\%$  of the detections in either filter. Other sources are either bright stars saturated in the long exposures or are near bright stars and masked from view in the long exposures. Photometry is chosen from shorter exposures for these sources. Table 1 lists all stars detected at both V and I band.

Figure 1 shows the distribution of V and I magnitudes versus their photometric uncertainties. There are clearly three (two) distributions of V vs.  $\sigma(V)$  (I vs.  $\sigma(I)$ ), which result from the three (two) separate exposure times used. The  $5\sigma$  ( $10\sigma$ ) limits in V band are  $V=21, 23$ , and  $24$  ( $19.5, 22, 23.25$ ) for 2, 75, and 300s exposure times. The corresponding limits in I band are  $I=19.5, 23.5$  ( $19, 23$ ) for 2s and 75s exposures. The number counts in V band plateau at  $V \sim 22-24$  and fall rapidly for fainter magnitudes. The number counts in I band peak at  $I \sim 21$ .

### 2.1.3. Comparisons with Previous Photometric Surveys

To provide a context for our photometry, we cross correlate our source list with catalogs from three major photometric surveys: Mayne et al. (2007), Slesnick et al. (2002), and

Keller et al. (2001). Mayne et al. (2007) is by far the deepest of the three but has a slightly smaller coverage area than our photometry ( $\sim 0.45 \text{ deg}^2$ ). Slesnick et al. (2002) is the shallowest but has a larger coverage ( $\sim 1 \text{ deg}^2$ ), and Keller et al. (2001) is intermediate in depth and has the smallest coverage ( $\sim 0.37 \text{ deg}^2$ ). The Mayne et al. (2007) and Keller et al. (2001) catalogs include I-band photometry; Slesnick et al. (2002) lacks I-band photometry.

To limiting magnitudes of  $V=22$  and  $I = 19.5$ , our photometry agrees very well with data from Mayne et al. (2007). To make this comparison, we consider a broad range of  $V=11\text{--}22$  where our photometry is unsaturated and where the Mayne et al. (2007) data have errors  $\lesssim 0.1 \text{ mag}$ . For this range of  $V$ , the  $V$ - $I$  colors for most stars range from  $\sim 0$  to  $2.5$ . Using a  $1.0''$  matching radius, we find 13,806 common sources brighter than  $V=22$ . Figure 2 (top panels) shows histogram plots of the differences in  $V$  and  $I$  magnitudes binned in units of  $0.02$  magnitudes. The differences in magnitudes are consistent with gaussian distributions that are strongly peaked about zero with full-width half-maxima of  $\approx 0.04$  and  $0.06$  magnitudes for  $V$  and  $I$ .

The agreement between our  $V$ -band photometry and that from Slesnick et al. (2002) is also excellent. The distribution of  $V$  magnitude differences among 1307 common sources has a full-width half-maximum of  $\sim 0.04$  magnitudes (Figure 2, middle panels). For nearly all sources with photometric differences greater than  $\sim 0.1$  magnitudes, we find fainter magnitudes from our photometry. Slesnick et al. (2002) measure stars' brightnesses using aperture photometry whereas as our method deblends overlapping sources. Therefore, the few cases with slightly discrepant photometry were plausibly blended sources in Slesnick et al. (2002) that were deblended with our photometry.

Our  $V$ -band photometry shows good agreement with that from Keller et al. (2001, Figure 2, bottom-left panel). The distribution of magnitude differences from 5355 common sources ( $V \lesssim 21$ ) has a FWHM of  $\sim 0.06$  magnitudes. However, we find substantial disagreement between the Keller et al. (2001) photometry and our  $I$  band photometry (Figure 2, bottom-right panel): there is a  $\sim 0.2$  magnitude zero-point offset and an additional, possibly color-dependent term which results in a wide dispersion (FWHM  $\sim 0.2$  magnitudes). We speculate that this difference may arise because Keller et al. (2001) used a nonstandard  $I$ -band filter or had larger uncertainties in their color transformations.

## 2.2. Optical Spectroscopy

To supplement the optical photometry, we acquired low-resolution optical spectroscopy of 2MASS-detected stars within one square-degree of the cluster centers. For faint ( $J \geq 14.25$ ;

$V \geq 16$ ) stars, we used the multiobject, fiber-fed spectrograph Hectospec (Fabricant et al. 2005) on the 6.5m MMT. Brighter stars were observed with the fiber-fed spectrograph Hydra (Barden et al. 1993) on the 3.5m WIYN telescope at Kitt Peak National Observatory and single-slit FAST spectrograph (Fabricant et al. 1998) on the 1.5m Tillinghast telescope at the Fred Lawrence Whipple Observatory.

### 2.2.1. Spectroscopy Reduction, Survey Coverage, and Completeness

We obtained Hectospec spectra of 9,373 stars with  $V \sim 16-19$ ,  $J \sim 14.25-16.25$ , and  $J-H \sim 0-1.5$  during the Fall 2006 and Fall 2007 observing trimesters in queue mode. Each source was observed in three 10-minute exposures using the  $270 \text{ mm}^{-1}$  grating. This configuration yields spectra at 4000-9000 Å with  $\sim 6 \text{ Å}$  resolution. The data were processed using the standard Hectospec reduction pipeline (Fabricant et al. 2005) and typically have  $S/N \gtrsim 30-50$  at 5000 Å.

We acquired additional spectra of 610 sources with the Hydra multifiber spectrograph on the WIYN 3.5 m telescope at the Kitt Peak National Observatory. Hydra spectra were obtained by A. Bragg and S. Kenyon during two observing runs in November 2000 and October 2001 and include stars with  $V \sim 14-17$  and  $J \sim 12-14.5$ . Exposure times ranged from 30 minutes to 90 minutes, depending on the source brightness and seeing conditions, and yielded spectra with  $S/N \approx 10-30$ . We used the  $400 \text{ g mm}^{-1}$  setting blazed at  $42^\circ$ , with a resolution of  $7 \text{ Å}$  and a coverage of 3600-6700 Å. The standard IRAF task *dohydra* was used to reduce the spectra. We also obtained spectra of 257 bright ( $J \leq 14.25$ ) stars surrounding h and  $\chi$  Per with the FAST spectrograph on the 1.5m Tillinghast telescope at Whipple Observatory. Finally, we added archived data of 1,025 h and  $\chi$  Persei sources from Bragg and Kenyon (2005) and Bragg (2004).

The combined Hectospec, FAST, and Hydra observations yield 11,265 spectra of stars on the h and  $\chi$  Per field. The spatial coverage of the Hectospec, FAST, and Hydra observations are shown in Figure 3. Hectospec and FAST observations cover about one square degree; Hydra observations and archival data focus on regions within  $\approx 15'$  of the cluster centers (black dots).

Our survey comprises a significant fraction of all 2MASS-detected sources on the field, especially those within  $\sim 10-15'$  of the cluster centers. Within the  $\approx 1$  square-degree area surrounding h and  $\chi$  Persei, we obtained spectra for 75% of all the 2MASS detections (11,265/14,951). Because many bright stars with colors suggestive of foreground M stars were not selected for observations with Hydra and FAST, completeness is better at faint

survey limits ( $J \geq 15$ ; 95%) than for brighter stars ( $J < 15$ ; 63%)

Completeness in the cluster-dominated regions ( $r \leq 5\text{--}15'$ ) is good for stars of all magnitudes. Within  $5'$  of both  $\eta$  Persei and  $\chi$  Persei, we have spectra for nearly all stars ( $\gtrsim 98\%$ ). Within  $10'$ , we have spectra for  $> 80\%$  of bright stars ( $J < 14$ ),  $> 95\%$  of faint ( $J \geq 15$ ) stars, and  $> 90\%$  of all stars. The majority (60%–70%) of bright stars at  $10\text{--}15'$  away from the cluster centers are detected. Thus, our spectroscopic survey comprises the vast majority of stars in the cluster-dominated regions, is unbiased within  $10'$  of the cluster centers, and is not biased for faint stars regardless of radial distance from the cluster centers.

### 2.2.2. Spectral Classification

The large number of spectra observed and the large number of stars earlier than K/M - which can be difficult to spectral type - makes manual, spectral classification inefficient. To spectral type stars, we employ the semi-automatic quantitative spectral-typing code **SPTCLASS**<sup>1</sup>, an IRAF/IDL code based on the method described in Hernandez et al. (2004).

**SPTCLASS** calculates the spectral types of stars using spectral indices, comparing the line flux of spectral features which are sensitive to stellar effective temperature (Payne 1924, 1925, and later references). Three independent spectral typing modules are included in SPTCLASS: indices that characterize early (OBA, 44 indices), intermediate (FG, 11 indices), and late spectral type (KM, 16 indices) stars. Each index is based on the equivalent width for each spectral feature which is obtained by measuring the decrease in flux due to line absorption from the continuum that is expected when interpolating between two adjacent bands. Indices measured by this procedure are largely insensitive to reddening as long as the wavelength coverage of each band is relatively small. Three spectral type estimates are then calculated by averaging the indices characterizing early, intermediate, and late-type stars. In general, visual inspection of the spectrum and the dispersion of individual results indicate which of these three results is the correct one for the star. The errors in these estimates are computed from the dispersion in spectral types for individual indices weighted by their correlation functions.

Typically, the most important lines were Ca II (3933Å), the G band (4305 Å), and Na I (5890 Å) for mid A to mid G stars and the TiO bands for later stars (Payne and Williams 1929; Gray and Corbally 2009). The spectral types as determined from individual indices for each of the three modules usually showed strong agreement. In cases where scatter was

---

<sup>1</sup>See [www.astro.lsa.umich.edu/~hernandj/SPTclass/sptclass.html](http://www.astro.lsa.umich.edu/~hernandj/SPTclass/sptclass.html) for more information

large (e.g., greater than 2-3 subclasses), we manually smoothed the spectra with `splot` and measured the indices for highly correlated lines listed above as a check on the computed spectral type.

For O, B, and early A stars, the strongest lines are the Balmer lines and the He I lines (e.g. Payne and Williams 1929, and later references). Because accreting pre-main sequence stars and Be stars can have Balmer line emission, spectral types based on the Balmer lines are produced by SPTCLASS but are not explicitly included in the semiautomated estimates. However, no B to mid A stars show accretion signatures; the Be star population is well known (e.g., Slesnick et al. 2002; Bragg and Kenyon 2002; Currie et al. 2008a). The absence of Balmer lines in the final spectral type determination may then introduce errors, especially for stars earlier than B5, where strengths of the important Mn I and Fe I lines become uncorrelated with spectral type. Therefore, we slightly modified our approach for early-type stars (B1–A2, as identified by SPTCLASS), basing the spectral types solely on the Balmer indices and He I indices. We selected lines that yielded a minimal scatter in the empirical HR diagram ( $V$  vs. spectral type), specifically  $H_\beta$ ,  $H_\gamma$ ,  $H_\delta$ , He I 4026 Å, and He I 6678 Å. The median average of the spectral types determined from each of these indices was chosen as the star’s spectral type; the standard deviation in these spectral types is identified as the uncertainty in spectral type. While this method produced essentially identical results for B5–A2 stars compared to the nominal SPTCLASS calculation, it significantly tightened the HR diagram locus for earlier stars, thus improving precision. Of the 11,265 stars with spectra, 10,934 were assigned spectral types. Stars without spectral types either had extremely low signal-to-noise or were cases where the Hectospec or Hydra fibers failed to center on the stars, possibly because of small astrometric errors.

We applied a final correction for the spectral types of the earliest stars by cross-correlating our source list with the spectroscopic survey of Slesnick et al. (2002). There are 108 stars in common. Agreement in spectral types determined from Slesnick et al. (2002) and those determined from SPTCLASS is typically good, within 1 subclass. However, as noted by many authors (Slesnick et al. 2002; Bragg and Kenyon 2005; Schild 1965, 1967),  $\eta$  and  $\chi$  Persei contains a large population of B supergiants, giants, and subgiants. Differences in luminosity classes for the earliest stars imply differences in surface gravities. Surface gravities affect line strengths and thus induce scatter in determining spectral types from these line strengths if the index-spectral type relationship is derived primarily from main sequence/pre-main sequence dwarfs. Therefore, we identify all stars listed by Slesnick et al. (2002) as having luminosity class I–IV and replaced our spectral types with those determined by Slesnick et al. (2002). Aside from shifting several stars initially classified as O9.5–O9.9 to slightly later types (B0–B1.5) (see also Bragg 2004), this correction yields inconsequential changes in the spectral type distribution and thus has a negligible impact on our later

analysis. Figure 4 displays a spectral type sequence from our sample.

Finally, we added 44 stars in the Slesnick et al. (2002) spectroscopic catalog that were not targeted with our survey (see Figure 3 for spatial distribution). These stars were predominantly optically and infrared bright B giants and supergiants, infrared bright red supergiants, and likely foreground dwarfs. Spectral type uncertainties for these 44 stars were set to two subclasses, consistent with the maximum dispersion in spectral types for early-type stars implied by comparing the Slesnick et al. (2002) results to SPTCLASS and previous literature measurements.

Because SPTCLASS does not determine luminosity classes, we manually analyzed the spectra of stars to identify giants and supergiants. Our identification criteria follow Gray and Corbally (2009) and Walborn (1971). For early-type stars, we measured the Si III 4552/He 4387 I line ratio as a primary indicator with the Si 4116 IV/He 4121 I line ratio and the O II 4415–4417 line strength as secondary indicators, using spectra from Gray and Corbally (2009) as standards. For M stars, we use the strength of the Ca I 4226 line and the shape of the TiO lines to identify giants and supergiants. Our analysis confirms the identification of giants and supergiants from Slesnick et al. (2002) and adds 30 more for a total of 103 giants and supergiants. Our primary spectra selection criteria ( $J > 14$ ) removes many foreground FGK stars (likely giants/supergiants) from our target list. Moreover, our spectroscopic survey is most complete for regions close to the cluster centers, where we expect the ratio of cluster stars to background/foreground stars to be the highest. Thus, the overwhelmingly large number of dwarfs assuredly overestimates the true ratio of dwarfs to giant stars on the field. Figure 5 displays a luminosity class sequence for early B stars.

Our final catalog contains 11,309 stars of which 10,983 have spectral types. Figure 6 shows the distribution of spectral types. The sample contains 1 O6.5 dwarf star, 914 B stars, 1,330 A stars, 4,362 F stars, 2,525 G stars, 1,300 K stars, and 551 M stars. Thus, a large fraction of our sample are either F stars or G stars. Because later-type stars at a given age correspond to lower-mass stars, the large number of FG stars compared to OBA stars is likely a consequence of the initial mass function. Only 2MASS sources were selected for our Hectospec observations. Cluster sources with JHK<sub>s</sub> magnitudes near the 2MASS sensitivity limit ( $J \sim 15.7$ ) likely have spectral types between G0 and K0 (Currie et al. 2007a, see also Baraffe et al. 1998). Therefore, the 2MASS sensitivity limits are likely responsible for the low number of detected mid G, K, and M stars.

The distribution of uncertainties in spectral types is shown in Figure 7. Most stars have  $\sigma(\text{ST}) \sim 2\text{--}2.5$  subclasses, which indicates that the dispersion in spectral types determined from individual indices is small for the vast majority of our sample. Stars with spectral types between O5 and F0 and K0–M5 have the smallest uncertainties ( $\sim 1$  sub-

class); stars with spectral types between F5 and G5 have the largest uncertainties ( $\sim 2.5$ – $3$  subclasses). Intermediate spectral type stars have higher uncertainties because they have fewer lines whose indices strongly correlate with spectral type. The deep Balmer lines and He I lines make spectral typing early-type stars robust; spectral typing later-type stars is aided by the TiO lines, whose strengths correlate extremely well with spectral type for stars later than K0. Table 2 lists the properties of stars with spectra. Each spectra taken with Hectospec, Hydra, and FAST is downloadable from the Telescope Data Center website: <http://tdc-www.cfa.harvard.edu/instruments/hectospec/progs/HXP/> for Hectospec, <http://tdc-www.cfa.harvard.edu/instruments/hectospec/progs/Hydra/> for Hydra, and <http://tdc-www.cfa.harvard.edu/instruments/FAST/> (Programs 83 and 170).

### *2.2.3. Optical Color-Magnitude Diagrams, HR Diagrams, and the Combined Photometric and Spectroscopic Catalog*

Figure 8 shows the V/V-I color-magnitude diagram for all stars in our optical catalog. To better identify trends in the V/V-I distribution, we use a Hess diagram, which plots the density of stars in color-magnitude diagrams, using bin sizes of 0.03 magnitudes in V-I and 0.06 magnitudes in V. The densest (darkest) region is located within the range of colors and magnitudes consistent with main sequence field stars with a wide range of distances, spectral types, and reddenings (e.g. Mayne et al. 2007).

Exceptional among nearly all young open clusters, the locus of  $h$  and  $\chi$  Persei stars is obviously distinguishable from the background star population by eye. An extremely narrow ( $\delta(V-I) \sim 0.25$ ) distribution of stars with bluer colors than the background field star population defines the Hess diagram for  $V < 17$ . Equally striking is the distribution of stars extending from  $V \sim 19$ ,  $V-I \sim 1.75$  to  $V \sim 24$ ,  $V-I \sim 3.5$ , which has a far more narrow dispersion in color for a given magnitude than the field star population:  $\delta(V-I) \sim 0.5$  at  $V = 19$  to  $\delta(V-I) \sim 0.75$  at  $V = 24$ . These distributions are consistent with a single narrow locus of young cluster stars.

Using a 1" matching radius, there are 7,465 sources with spectral types, near-IR photometry, and optical photometry from either our VI survey or from Slesnick et al. (2002). Thus, a substantial percentage ( $\sim 68\%$ ) of stars with spectra have optical data. For our combined photometric and spectroscopic catalog, we adopt our optical photometry in a first iteration. Our V-band photometry show excellent agreement with that of Slesnick et al. (2002) over a wide magnitude range; our V-band data saturates at  $V < 11$ - $12$ . Therefore, we adopt the Slesnick et al. (2002) V-band photometry for stars brighter than  $V=12$ .

Sources with both optical photometry and spectroscopy show a clear distribution from early to late-type stars (Figure 9). Nearly all stars brighter than 16th magnitude and blueward of  $V-I = 1$  have spectral types between B0 and A5. Similarly, stars from  $V = 16$  to 19 become progressively later (A5 to K0). Comparing both panels of Figure 9 clearly reveals foreground and interloping stars, whose spectral types are discrepant compared to other stars located in the same regions in  $V/V-I$  space. Table 3 lists the 7,465 stars with optical photometry and spectroscopy. Our study focuses on these stars and on the  $\sim 47,000$  with optical photometry.

#### *2.2.4. Determining Effective Temperature Scale and Intrinsic Colors of Dwarfs, Giants, and Supergiants*

Deriving the physical properties of cluster stars from spectroscopy requires adopting a spectral type-effective temperature ( $T_e$ ) scale and identifying the intrinsic colors of stars as a function of  $T_e$ . Our adopted effective temperature scales and intrinsic colors are described and justified in Appendix A. Briefly, the effective temperature scale for dwarfs is drawn from analyses of O5–B0 stars (Massey et al. 2005); B0.2–A0 stars (Humphreys and McElroy 1984; De Jager and Nieuwenhuijzen 1987; Bessell et al. 1998); and cooler main sequence stars (Kenyon and Hartmann 1995; Gray and Corbally 2009). For O giants and supergiants we adopt the relations from Massey et al. (2005). For B–M giants we adopt the scale from Gray and Corbally (2009); we use a combination of Humphreys and McElroy (1984), De Jager and Nieuwenhuijzen (1987) and Gray and Corbally (2009) for B supergiants, Gray and Corbally (2009) alone for A–K supergiants, and Gray and Corbally (2009) and Levesque et al. (2005) for M supergiants.

To derive intrinsic colors of stars as a function of effective temperature, we follow the methods of the Padova stellar evolution group (e.g. Girardi et al. 2002; Marigo et al. 2008). We use colors derived from the corrected ATLAS9 spectra (Castelli and Kurucz 2003) for O–K dwarfs and supergiants/giants (see also Kurucz 1992; Castelli and Kurucz 1997). For cooler dwarfs, we use colors from the PHOENIX "BDDUSTY99" stellar atmosphere models (Allard et al. 2000a,b). We supplement the ATLAS9/PHOENIX grid for the coolest dwarfs ( $T_e < 3400$  K) with empirically calibrated dwarf colors from the BaSeL stellar library (Lejeune et al. 1998). For M supergiants, we adopt the corrected colors from the empirical M giant spectra of Fluks et al. (1994). Table 7, 8, and 9 list the intrinsic  $UBVI_cJHK$  Johnson-Cousins-Glass colors of stars as a function of  $T_e$ , spectral type, and luminosity class.

### 2.2.5. *Measuring Reddening and Extinction*

To derive the reddening ( $E(B-V)$ ) for each source, we compare the observed optical/near-IR colors with intrinsic colors for the star’s spectral type. We first convert our 2MASS photometry into the Johnson-Cousins-Glass system as formulated by Bessell (1990) using an updated version<sup>2</sup> of the color transformations from Carpenter (2001). From our effective temperature scale, we identify  $T_e$  for each star based on its spectral type. We calculate the star’s intrinsic colors by interpolating between values on the ATLAS9/BDDUST99/BaSeL/Fluks grid for a given  $T_e$ .

To constrain reddening for dwarfs and hot giants/supergiants, we use the long-baseline V-J, V-H, and V-K colors. From the equations of Cardelli et al. (1989), the wavelength zeropoints from Bessell and Brett (1988) and Bessell (1990), and for  $R_V = A_V/E(B-V) = 3.12$  we use:

$$E(B - V)_J = E(V - J)/2.20 \tag{1}$$

$$E(B - V)_H = E(V - H)/2.55 \tag{2}$$

$$E(B - V)_K = E(V - K)/2.76. \tag{3}$$

Because our I band data saturate at much fainter magnitudes than either the Slesnick et al. (2002) V band photometry or 2MASS, we do not derive  $E(B-V)$  from I band photometry. The difference between the reddening derived from individual colors and the mean reddening has a gaussian distribution with a full-width half maximum  $\lesssim 0.03$  mags centered on 0–0.01. To minimize photometric errors whose propagation leads to errors in reddening, we median combine the three values together to derive a final  $E(B-V)$  for each star<sup>3</sup>

For M supergiants, we determine reddening solely from the J-K colors. Most M supergiants in  $\eta$  and  $\chi$  Persei undergo significant radial pulsations (e.g. Levesque et al. 2005) which change their effective temperatures by tens to 100s of K. Because the Johnson BVI bands fall along the Wien tail of M stars’ spectral energy distributions, these temperature changes produce large changes in the stars’ V-J, H, and K colors. Furthermore, the long-baseline colors (in particular, V-J) are very sensitive to surface gravity. The J-K colors are only weakly affected by pulsation and photometric errors:

$$E(B - V) = E(J - K)/0.56. \tag{4}$$

---

<sup>2</sup><http://www.astro.caltech.edu/~jmc/2mass/v3/transformations/>. These values are similar to but supercede those published in Carpenter (2001). Their republication in Bessell (2005) contains a typographical error for the J–K color transformation.

<sup>3</sup>We choose the median reddening instead of the mean because it is less sensitive to photometric errors in one filter.

Thus, measuring  $E(B-V)$  for all stars on the field, we deredden their photometry in each passband using extinction relations from Cardelli et al. (1989):

$$V_o = V_{obs} - 3.12 \times E(B - V) \quad (5)$$

$$I_o = I_{obs} - 1.87 \times E(B - V) \quad (6)$$

$$J_o = J_{obs} - 0.92 \times E(B - V) \quad (7)$$

$$H_o = H_{obs} - 0.57 \times E(B - V) \quad (8)$$

$$K_o = K_{obs} - 0.36 \times E(B - V) \quad (9)$$

These relations agree with those from Bessell and Brett (1988) to within  $\sim 3\%$ . To verify that these equations deredden the data well, we compare the dereddened and intrinsic colors for our B–M dwarfs. The systematic offsets in V-I, V-J, V-H, and V-K vs. spectral type and  $T_e$  are 0.005–0.02 magnitudes in all cases, less than the uncertainties in intrinsic colors and reddening.

Figure 10 shows the distributions of reddening vs. spectral type for stars in the core-dominated regions ( $r_{core} < 10'$ ) and the low-density halo population. Most stars on the field have  $E(B-V) \approx 0.45$ – $0.65$  (top-left panel), but closer analyses reveal systematic differences in the reddening distribution as a function of location (top-right panel). Specifically, the h Persei core has a slightly higher median reddening among B3–F9 stars<sup>4</sup> than the  $\chi$  Persei core, though its dispersion in reddening is essentially identical:

$$E(B - V)_{hPer} \sim 0.55 \pm 0.10 \quad (10)$$

$$E(B - V)_{\chi Per} \sim 0.52 \pm 0.10. \quad (11)$$

The low-density halo has approximately the same median reddening for B3–A9 stars,  $E(B-V) \sim 0.52 \pm 0.1$ , though the far heavier field star contamination prevents robust conclusions about the median reddening for stars earlier than G0 as with the cluster-dominated regions. These results show exceptional agreement with those from Slesnick et al. (2002) who determined  $E(B-V)$  for stars earlier than B3–B5.

In contrast to results from Bragg and Kenyon (2005), there is no evidence for a spectral type-dependent reddening in either core region through G0 (bottom panels). The population of G0–K0 stars with high reddening is almost completely drawn from stars whose positions on both observed and dereddened color-magnitude diagrams place them foreground to the

---

<sup>4</sup>We determined the median cluster reddening from spectral type range because it puts us safely out of the range of Be stars and nearly all supergiants on the bright, early end and nearly all of the background field stars on the late, faint end.

clusters. The core region stellar population later than G0 is diluted by a combination of survey incompleteness and mass segregation. A substantially non-solar metallicity would be the most likely cause of any spectral-type dependent reddening, because the colors for a given  $T_e$  would be different, especially for stars later than A spectral type. Thus, our data show no clear evidence that h and  $\chi$  Persei are significantly metal poor or metal rich.

As shown by Figure 11, dereddening stars makes an already narrow and populous upper main sequence even better defined. Both the dereddened V/V-J color-magnitude diagram and the V vs. spectral type Hertzsprung-Russell diagram show a thin, dense locus of probable cluster stars from  $V_o = 10$  to  $V_o = 14.75$  that is clearly separable from a second, low-density distribution that presumably contains mostly field stars. Comparing Figure 11 with Figure 8 indicates that the distribution of spectroscopically examined stars widens at  $V_o = 15.5$ – $16.75$ , F5–G5 as the cluster locus runs above the background field star distribution. The distribution thins out for stars later than G0–G5 because many late-type stars were too faint to be selected for spectroscopic observations.

### 3. Analysis: The Distance Moduli and Ages of h and $\chi$ Persei

We now combine the optical photometric and spectroscopic data of all stars on the field to constrain the mean distance moduli and ages of h and  $\chi$  Persei. First, we analyze the dereddened V-band magnitudes of main sequence stars in cluster-dominated regions as a function of spectral type and V-J, V-H, and V-K colors to infer distance moduli for both clusters. We then constrain their post-main sequence ages by identifying the main sequence turnoffs and analyzing the luminosities of the clusters’ M supergiants. Finally, we analyze the deep optical data alone to measure ages derived from fitting isochrones to pre-main sequence stars and compare these estimates with post-main sequence ages to pinpoint the true mean age and dispersion in age for h and  $\chi$  Persei.

For both clusters, we successfully derive robust and self-consistent values for cluster properties. Even though  $\chi$  Persei is less populous (see Section 5 and Slesnick et al. 2002; Bragg and Kenyon 2005; Currie 2008), its parameters have the smallest uncertainties (see also Mayne et al. 2007). Stars within the h Persei core ( $< 10'$  of the center) exhibit a wider dispersion in properties. Analysis of stars in the low-density halo regions surrounding both cores is plagued by sample incompleteness and slightly higher levels of field star contamination. Thus, in each section we discuss properties of  $\chi$  Persei first, h Persei second, and the low-density halo region third to illustrate how our analysis constrains cluster properties.

### 3.1. The Distance to h and $\chi$ Persei

We now measure the distance moduli to h and  $\chi$  Persei by "main sequence fitting". This approach slightly differs from that by other authors (e.g. Slesnick et al. 2002) who argue that main sequence fitting must be done with post-main sequence and pre-main sequence isochrones. Although certainly true with previous, shallower h and  $\chi$  Per spectroscopic surveys, the colors and magnitudes of dereddened stars from our larger dataset define a tight locus for much later spectral types, where stars are on the main sequence for a wide range of ages.

Simple arguments demonstrate that the mean age of h and  $\chi$  Persei is most likely between  $\approx 10$  Myr and  $\approx 30$  Myr. The field includes only one O star (HD 14434), which is likely an interloping field star (Slesnick et al. 2002). Otherwise, the earliest stars in the cluster are later than B0. Between B0 and B2.5, stars are predominately giants and supergiants: dwarfs only clearly dominate the stellar population later than B3–B4. Because the main sequence lifetime of early B stars is at least  $\sim 10$  Myr (cf. Bertelli et al. 1994; Schaller et al. 1992), the clusters are likely at least 10 Myr old. The main sequence lifetime of B4–B5 stars is  $\lesssim 30$  Myr; thus, the lack of giants among mid-B stars implies an upper age limit of 30 Myr.

Figure 12 illustrates the age independence of the luminosity and temperature of B5–A5 stars for over the 10–30 Myr age range. We plot the predicted V vs. V-J loci for 10 and 20 Myr-old pre-main sequence stars from the Siess evolutionary tracks (Siess et al. 2000) and D’Antona and Mazzitelli tracks (D’Antona and Mazzitelli 1994)<sup>5</sup>, using our conversions from  $T_e$  to colors. The leftmost point for each pre-main sequence track corresponds to the highest mass, bluest star yet to reach the main sequence. We also overplot the 10–30 Myr Padova post-main sequence evolution tracks (Marigo et al. 2008) and zero-age main sequence. Over a significant range in  $M_V$  and V-J color, there is substantial agreement between all pre-main sequence and post-main sequence tracks regardless of age. In particular, stars with  $M_V = 0.5$ –2, V-J = -0.3–0.15 ( $\sim$  B5 – A5 stars) are all on the main sequence. If we consider only the D’Antona and Mazzitelli (1994) pre-main sequence tracks, agreement expands to  $M_V = 2.5$ , V-J = 0.5 ( $\sim$  A9 stars).

Motivated by these comparisons, we measure the distance modulus primarily by identifying where the zero-age main sequence lines up with B5–A5 stars (i.e. where the density of stars on the ZAMS is highest). Additionally, because stars contract *onto* the main sequence from the pre-main sequence (losing luminosity), the zero-age main sequence cannot lie above

---

<sup>5</sup>This is the only place in the paper where we use the Siess et al. (2000) and D’Antona and Mazzitelli (1994) tracks. We do not use the Baraffe et al. (1998) tracks here because they do not extend to sufficiently high masses.

the locus of later-type stars. We divide stars on the field into three groups: those within 10' of the  $\chi$  Persei center, those within 10' of the h Persei center, and those in the low-density halo region.

### 3.1.1. The Distance to $\chi$ Persei

The results of our main sequence fitting are listed in Table 4 and illustrated in Figures 13 and 14. Figure 13 reveals that main sequence fitting of  $\chi$  Persei stars can determine the cluster's distance modulus with high precision. In particular, the V vs. spectral type distribution (top panel) defines a sharp locus for nearly all stars earlier than G0, including main sequence B5–A5 stars. While slightly more dispersed, the positions of stars in V/V-J (bottom panel) as well as V vs.  $\log(T_e)$ , V/V-H, and V/V-K (not shown) also define very narrow distributions. Distance moduli measured from spectral types,  $T_e$ , and the three infrared colors are essentially identical.

From main sequence fitting, we derive a median distance modulus to  $\chi$  Persei (thick line)  $dM_{\chi Per} = 11.85$ , which we calculate by taking the median value for the four individual estimates. The main sequence locus for  $dM = 11.85$  clearly runs through the middle of the main distribution of B5–A5  $\chi$  Per stars. By comparison, loci for  $dM = 11.77$  and  $11.93$  (thin dashed lines) lie above and below the main distribution of B5–A5 stars in most cases. We cannot clearly identify disagreement between the observed distribution and main sequence loci for distance moduli between these extrema (e.g., 11.82, 11.88). Therefore, we consider our mean distance modulus determination to be accurate within 0.08 mag. Thus,

$$dM_{\chi Per} = 11.85 \pm 0.08 \quad (d = 2344_{-85}^{+88} pc). \quad (12)$$

### 3.1.2. The Distance to h Persei

Though the locus of h Persei stars shows a wider dispersion as a function of spectral type and color, main sequence fitting yields a precise estimate for its median distance modulus,

$$dM_{h Per} = 11.80 \pm 0.08 \quad (d = 2290_{-82}^{+87} pc). \quad (13)$$

Thus, the cluster is slightly foreground to  $\chi$  Persei. While the uncertainty in distance modulus is sufficiently large that formally h and  $\chi$  Persei are at the same distance (within errors), h Persei is systematically foreground by the same amount as inferred from each of the four estimates by identical amounts (see Table 4 and Figure 14). Moreover, because the

distance modulus is derived from analyzing main sequence stars, not post-main sequence stars, h Persei’s offset cannot be due to subtle differences in its evolved star population.

The difference in distance modulus is plausibly real because the difference is systematic and also because it is consistent with some previous independent analysis performed using completely separate methods. Using the Q method<sup>6</sup>, Mayne et al. (2008) also found a small but systematic difference in distance modulus nearly identical to ours. The distance moduli derived by Mayne et al. (2008) – 11.78 for h Persei and 11.82 for  $\chi$  Persei – are within 0.02–0.03 mags of our estimates. Our dM estimates also agree with those from Slesnick et al. (2002, dM = 11.85 for both clusters). Because their spectroscopic survey was limited to early-to-mid B stars, they were unable to measure a clear difference in dM for the two clusters. The main sequence steeply rises in  $M_V$  for a given spectral type for B stars; the main sequence is more horizontal for late B stars/early A stars, which makes differences in distance modulus stand out more.

### 3.1.3. Distance to the halo population of h and $\chi$ Persei

Our most unique contribution regarding the distance to h and  $\chi$  Persei stars is a first precise estimate for stars in the halo population. Figure 15 plots our fits. The huge density change between the population of stars earlier and later than B5 is solely a reflection of our survey bias: the earlier stars were too bright to be selected for Hectospec observations, were derived solely from FAST observations which were fewer in number, while Hectospec data covers later stars. To more clearly present the empirical locus of main sequence stars, we shrink the symbol sizes by 30 %. The upper main sequence of halo stars (B5–A5) is separable from the field star population despite the higher level of contamination.

Interestingly, we find that stars in the halo population have a well defined locus implying a distance modulus essentially identical to that of the core region stars, especially  $\chi$  Persei’s:

$$dM_{halo} = 11.85 \pm 0.08 (d = 2344pc^{+88pc}_{-85pc}). \quad (14)$$

The halo stars with spectra are drawn from throughout the  $\sim 1$  square degree region surrounding both clusters. At the distance of h and  $\chi$  Persei, the projected size of the halo is  $\approx 41$  pc, which is comparable to the difference in distance modulus between the cluster cores. If the halo region has a roughly spherical shape, it may surround both cluster cores. Previous estimates for the halo population’s distance modulus place it within 30% of the core

---

<sup>6</sup>The Q method determines the mean cluster extinction iteratively by using relationships between optical reddening laws and the intrinsic colors of O and B stars (see Johnson and Morgan 1953).

regions (Slesnick et al. 2002). Our analysis indicates that stars in the low-density regions surrounding both cores *that are most plausibly associated with the cores* are at distances within  $\sim 5\%$  of the cores’ distances.

### 3.1.4. *Uncertainties in Distance Modulus*

To evaluate the origin of the uncertainties in our estimates for the distance modulus, we now consider each point in the process. Table 4 indicates that uncertainties in dereddening infrared photometry from filter to filter contribute a negligible level of uncertainty in distance modulus estimates. A more important source of uncertainty is the assumed ratio of optical extinction to reddening in B-V. We adopt the standard value of  $R_V = 3.12$ , appropriate for reddening due primarily to interstellar dust. Diffuse mid-IR nebular emission, expected in dark cloud regions where  $R_V$  is large, is minimal in the Spitzer IRAC and MIPS mosaics of the Double Cluster (Currie et al. 2010); Slesnick et al. (2002) also argue that reddening is likely entirely due to line-of-sight extinction from the ISM. Our assumed  $R_V$  brackets previous estimates of  $R_V = 3.0 \pm 0.1$  and  $R_V = 3.2 \pm 0.04$  by Johnson (1965) and Uribe et al. (2002) for cluster stars. Over this range in  $R_V$ , the distance moduli formally have a systematic uncertainty of  $\approx 0.06$  mags. However, considering data from Slesnick et al. (2002) and Currie et al. (2010), the evidence for deviations from the standard  $R_V$  is far from convincing.

Slightly more important is the error in determining the dereddened V band magnitude by uncertainties in  $E(B-V)$ . As noted in §2, the dispersion in  $E(B-V)$  derived in each optical/IR color is  $\lesssim 0.03$  mags. This uncertainty results in a maximum dereddening error of  $\delta V_o \approx 0.09$ .  $E(B-V)$  derived for most sources show even better internal consistency; the distributions of  $E(B-V) - E(B-V)_{J,H,K}$  show a gaussian distribution centered on 0.00-0.01. Therefore, uncertainties in  $E(B-V)$  simply widen the dereddened V vs. spectral type/ $\log(T_e)$  and V vs. J/H/K loci, and do not systematically shift the position of the locus.

The primary source of uncertainty in distance modulus (and other parameters derived later) is metallicity, which affects the luminosity of stars at a given age. Throughout the paper, we assume that h and  $\chi$  Persei has an approximately solar metallicity. While the research literature shows significant disagreement over the Double Cluster’s metallicity, we explain why a solar metallicity is more likely in Appendix B.

### 3.2. The Post-Main Sequence Ages of h and $\chi$ Persei

We now estimate the post-main sequence ages of h and  $\chi$  Persei stars via two methods. Identifying the location of the main sequence turn off, where stars of increasing luminosity become cooler as they evolve to become giants, provides a robust age estimate for massive clusters. We measure the location of the main sequence turnoff by comparing the spectral types and colors of stars of a given V magnitude to predictions from the Padova stellar evolution models (Girardi et al. 2002; Marigo et al. 2008). Isochrones whose spectral types/colors bisect the stellar population at a given V magnitude at the turnoff best reflect the clusters’ main sequence turnoff age. Figures 13 and 14 imply that the turnoff occurs at  $V \approx 8$  for both clusters. The main sequence turnoff age is the source of nearly all previous age estimates for h and  $\chi$  Persei (e.g. Keller et al. 2001; Slesnick et al. 2002; Bragg 2004). With our large spectroscopic survey, we can strengthen previous constraints on the Double Cluster’s main sequence turnoff age(s).

The luminosities and colors of M supergiants also constrain the ages of h and  $\chi$  Persei. Between 10 and 20 Myr, stars with masses  $\approx 10\text{--}15 M_{\odot}$  reach the M supergiant phase and rapidly evolve in luminosity; M supergiants dim by nearly an order of magnitude over this age range (e.g. Bertelli et al. 1994; Schaller et al. 1992). Because the temperature of the reddest supergiants also varies with age *and* metallicity (Bertelli et al. 1994; Marigo et al. 2008), combining V-band luminosities and long-baseline colors (e.g., V-J, V-H, and V-K) provides a sensitive probe of the stars’ ages and may constrain the clusters’ metallicities (see Appendix B). Because isochrones did not extend to very cool temperatures thought to characterize M supergiants (e.g. Slesnick et al. 2002), most previous investigations did not infer cluster ages from these stars. However, the recent recalibration of the M supergiant  $T_e$  scale to systematically higher temperatures by Levesque et al. (2005) makes age estimates possible. Table 5 summarizes our results, which are described in more detail below.

#### 3.2.1. Ages from the Main Sequence Turnoff

Figure 16 and 17 plot V vs. spectral type and V vs.  $\log(T_e)$  for stars within 10’ of the cluster cores against the Padova post main sequence isochrones for 10 Myr and 20 Myr and one intermediate age, which varies from panel to panel. In each figure, we assume the distance moduli derived in previous sections. If the cluster’s age and distance spread is minimal, nearly all stars should deredden to a single, well-defined locus. However, Be stars, which are abundant in h and  $\chi$  Persei (e.g., Bragg and Kenyon 2002; Currie et al. 2008a), can have intrinsically red near-IR colors (Dougherty et al. 1991, 1994) due to circumstellar gas/dust shells. Therefore, we do not consider these stars in locating the main sequence

turnoff.

Adopting a solar metallicity and the Padova stellar evolution models, the main sequence turnoff age of  $\chi$  Persei is about 14 Myr. In Figure 16, the agreement between the 14 Myr isochrone (solid line, top panels) and the observed turnoff is unambiguous. The curve in the isochrone at  $V_o \sim 7.5\text{--}9.5$  clearly rules out a 10 Myr age because almost all sources lie to the right in both spectral type and  $\log(T_e)$  space. Similarly, a 20 Myr age is ruled out because the vast majority of stars in both panels lie to the left of its isochrone. The 14 Myr isochrone bisects the stars’ positions in both top panels, especially in  $V_o$  vs. spectral type space.

The HR diagram in  $V_o\text{--}\log(T_e)$  space allows a firmer constraint on the age of  $\chi$  Persei. The 12 Myr isochrone (lower left panel of Figure 16) clearly overestimates the temperatures of the earliest B stars at the turnoff by  $\sim 0.05$  dex and overpredicts the temperatures at a given  $M_V$  for all bright cluster stars except for the Be stars. Conversely, the 16 Myr isochrone plotted in the lower right panel generally predicts too cool temperatures, including at the turnoff ( $\sim 0.05$  dex too cool). Though we consider the 14 Myr isochrone to provide the best visual fit, isochrones for 13 Myr and 15 Myr also correctly predict the temperature at the MS turnoff. Therefore,  $\chi$  Persei has a formal MS turnoff age of

$$t_{\chi Per, MS\text{turnoff}} = 14 \pm 1\text{Myr}. \quad (15)$$

Figure 17 reveals that the main sequence turnoff for h Persei is nearly indistinguishable. For h Persei, both the 13 Myr (shown) and 14 Myr (not shown) isochrones correctly predict the turnoff temperature and follow the distribution of cluster stars from  $V_o = 6.5$  to 10. Given the larger photometric and spectroscopic scatter for h Persei, it is impossible to choose confidently between the two isochrones. Thus, we average them for our best-fit value. Compared to  $\chi$  Persei, h Persei’s range of possible turnoff ages may be very slightly shifted towards younger ones. Comparing the bottom panels of Figures 16 and 17, the 12 Myr isochrone does not overpredict the turnoff temperature as badly for h Persei as it does for  $\chi$  Persei. However, because the intrinsic dispersion of  $V_o$  vs.  $\log(T_e)$  is much larger for h Persei, we interpret this observation to mean that the age uncertainty is larger. Our adopted MS turnoff age for h Persei is:

$$t_{h Per, MS\text{turnoff}} = 13.5 \pm 1.5\text{Myr}. \quad (16)$$

Because our spectroscopic sample is very incomplete for B stars in the low-density halo regions surrounding the cluster cores, our turnoff age estimate for the halo population is formally more uncertain. However, as Figure 18 suggests, the likely turnoff age for h and  $\chi$  Persei halo stars is about the same as the core dominated regions. The shape of the

observed turnoff clearly rules out both the 10 Myr and 16 Myr isochrones; isochrones with intermediate ages are plausibly consistent. Therefore, our derived turnoff age for the halo population is:

$$t_{halo,MSturnoff} = 13 \pm 2\text{Myr} \quad (17)$$

Thus, within our measurement uncertainties the turnoff ages for all regions of h and  $\chi$  Persei are  $\sim 14$  Myr determined from  $V_o$  vs. spectral type and  $\log(T_e)$ . While differences in cluster loci for different ages are more pronounced for  $V_o$  vs.  $\log(T_e)$ , the loci are also more prone to random errors. Specifically, in Figures 16 through 18 the distribution of  $V_o$  vs.  $\log(T_e)$  for h and  $\chi$  Per stars exhibits a larger dispersion about the 14 Myr locus than they do in  $V_o$  vs. spectral type space. Taken at face value, the V band magnitudes and temperatures for some bright, hot stars are more consistent with the 20 Myr isochrone. We cannot definitively rule out the existence of a small population of 20 Myr-old stars. However, the tight clustering in  $V_o$  vs. spectral type indicates that uncertainties in  $\log(T_e)$  provide a more simple explanation for this larger dispersion than a true age spread.

### 3.2.2. Ages Determined from M supergiants

The red supergiants provide additional evidence for an age of  $\approx 13$ –14 Myr. In each panel of Figure 19, we plot the predictions for 10 Myr and 16 Myr isochrones as dashed lines; the solid line represents the intermediate age isochrone, which is varied between 12 Myr and 14 Myr. Because there are no M supergiants within 10' of h Persei, we can only estimate ages for  $\chi$  Persei and the halo population.

Inspection of the panels clearly rules out 10 Myr and 16 Myr as the ages for  $\chi$  Per and the halo region. From the positions of M supergiants relative to the isochrones, 13 Myr and 14 Myr are equally plausible ages for both the  $\chi$  Per core and halo regions. The 12 Myr isochrone slightly overpredicts the maximum luminosity of M supergiants and underpredicts the maximum V-J color. The 15 Myr isochrone (not shown) slightly underpredicts the typical luminosities and overpredicts the maximum V-J color. Therefore, we consider the best-estimate ages for  $\chi$  Persei and the halo population as:

$$t_{\chi Per, Msupergiants} = 13.5 \pm 1.5\text{Myr} \quad (18)$$

$$t_{halo, Msupergiants} = 13.5 \pm 1.5\text{Myr} \quad (19)$$

### 3.3. The Pre-Main Sequence Ages of $\eta$ and $\chi$ Persei

As shown by Figure 8, our new optical photometry reveals faint, low-mass stars plausibly associated with  $\eta$  and  $\chi$  Persei whose  $V$  band luminosity at a given color is significantly higher than that of the background field star population. The photometry extends over 14 magnitudes in  $V$ : over this range the positions of solar/subsolar-mass stars in  $V$  vs.  $V-I$  color-magnitude diagrams are a sensitive function of stellar age (e.g. Baraffe et al. 1998). We now derive the pre-main sequence age of  $\eta$  and  $\chi$  Persei stars by comparing their color-magnitude diagram positions to predictions from the Baraffe et al. (1998) isochrones.

Even though a plausible cluster locus is clearly observable and can be fit from visual inspection of Figure 8, we follow a slightly more statistical approach to obtain a more robust pre-main sequence age. Field star contamination is larger for fainter stars. A Hess diagram of all stars on the field will have an increased density in regions occupied by fainter cluster stars (at a given color), which may artificially dim the apparent cluster locus. Thus, to be conservative, we must subtract out the background field star population near the cluster locus.

Our method is as follows. We construct Hess diagrams of stars within the  $\eta$  and  $\chi$  Persei cores ( $r < 7'$ )<sup>7</sup> and halo region (10'–20' away from both cluster centers). Next, we construct a Hess diagram of the 'background', which we obtain from stars greater than 21' distant from both cluster centers. The cluster and halo Hess diagrams are box-car smoothed by two resolution elements; the background diagram is smoothed by four resolution elements, essentially yielding an 'unsharp mask' of the background  $V/V-I$  distribution. Finally, we scale the background diagram to the densities of the core/halo diagrams and subtract the background from the core/halo diagrams. We determine the pre-main sequence age by overplotting solar metallicity Baraffe et al. (1998) isochrones, assuming a mixing length parameter of  $1.9 H_p$  and distance moduli/reddenings equal to those found in previous sections.

Figures 20, 21, 22 illustrate our results. In each figure, the black line (dash-three dots) identifies the main sequence/post-main sequence locus from the Padova isochrones. The solid dark grey line identifies the Baraffe et al. (1998) isochrone position for  $0.6 M_\odot$  (lower right end) to  $1.4 M_\odot$  (upper left end) stars. In Figures 20 and 21, the entire cluster locus is plainly visible. The background has been almost completely subtracted out. The halo population is more poorly defined (Figure 22): the locus of cluster stars is entirely absent in some regions ( $V-I \sim 1.5\text{--}1.6$ ). This poorer definition probably occurs because even regions  $> 20'$  away

---

<sup>7</sup>This radius is adopted instead of 10' because it yields a cleaner background subtraction. We obtain identical results for the pre-MS age with a 10' radius.

have some small population of halo stars, so the halo population is partially subtracted out. However, both the upper main sequence and the pre-main sequence redder than  $V \sim 1.7$ –2 are clearly visible and well separated from the background field star population. Comparing both panels of Figure 22 demonstrates that the apparent cluster locus in the subtracted diagram is real.

Assuming that the faintest h and  $\chi$  Per stars ( $V \sim 23.5$ –24) are as reddened as the bright, spectroscopically observed stars analyzed in the previous section, they typically have intrinsic  $V-I \sim 3$ . According to Table 7 and Baraffe et al. (1998), these stars likely have  $T_e \approx 3000$  K and masses  $\sim 0.1 M_\odot$ . Although these determinations are highly uncertain, *it is possible that the faintest cluster stars detected in our survey have masses approaching the hydrogen burning limit*. At the very least, cluster stars with  $V \sim 23$ –24 likely probe well into the M dwarf spectral type range.

Comparing the distribution of h and  $\chi$  Per stars to the Baraffe et al. (1998) isochrones clearly shows that the pre-main sequence ages for all three components of the Double Cluster are nearly identical to the post-main sequence ages:

$$t_{pre-MS,\chi Per} = 14_{-1.4}^{+1.9} \text{Myr} \quad (20)$$

$$t_{pre-MS,h Per} = 14_{-1.4}^{+1.9} \text{Myr} \quad (21)$$

$$t_{pre-MS,halo} = 14_{-1.4}^{+1.9} \text{Myr}. \quad (22)$$

In all cases, the 14 Myr isochrone best bisects the densest regions of the cluster loci: isochrones for 12.6 Myr overpredict the V band luminosity at a given color, while the 15.9 Myr isochrone underpredicts the luminosity. Moreover, the slope of the 14 Myr Baraffe et al. (1998) isochrone accurately tracks the observed locus. This agreement is remarkable considering that the important processes driving post-main sequence evolution for high-mass stars – changes in internal structure fundamentally due to nuclear reaction rates and the lack of hydrogen and helium in the stellar core – are not the same as those driving pre-main sequence evolution for low-mass stars: Kelvin-Helmholtz contraction and the onset of hydrogen burning as a star follows a radiative or convective track onto the main sequence.

### 3.4. Pre-Main Sequence Age Estimates Based Off of the D’Antona and Mazzitelli (1994) and Siess et al. (2000) isochrones

The Baraffe et al. (1998) isochrones are only one of many that are often used to determine cluster ages from the observed loci of pre main sequence stars. To compare the Baraffe et al. isochrones with others, we overplot 10–20 Myr isochrones from D’Antona and Mazzitelli (1994, 1997) and Siess et al. (2000) on the color-magnitude diagram for  $\chi$  Persei in Figures

23 and 24. For both sets of isochrones, we transform the computed luminosities and effective temperatures into V band magnitudes and V-I color using our effective temperatures and intrinsic colors. We display isochronal positions for stars more massive than  $0.5 M_{\odot}$ .

While neither set of isochrones yields ages less than 10 Myr or greater than 20 Myr, they show a clear disagreement with 14 Myr Baraffe et al. (1998) locus and a failure to accurately reproduce the shape of the observed pre-main sequence locus. The slope of both sets of isochrones are systematically steeper than the Baraffe et al. (1998) isochrones. The mismatch between the D’Antona and Mazzitelli (1994, 1997) isochrones and the observed locus is particularly striking. The 10 Myr isochrone overpredicts the luminosities of  $1.5\text{--}2 M_{\odot}$  stars ( $V\text{-}I \sim 1\text{--}1.5$ ) but underpredicts the luminosities of slightly redder stars ( $V\text{-}I \sim 1.5\text{--}2$ ). The 20 Myr isochrone underpredicts the luminosity of cluster stars redder than  $V\text{-}I \sim 1$ . The D’Antona and Mazzitelli (1994, 1997) grid lacks published entries at intermediate ages. However, unless only the  $1.5\text{--}2 M_{\odot}$  stars fade in V while at a constant temperature (unlikely), isochrones at intermediate ages would not clearly provide a better match to the observed locus. Thus, we cannot derive a best-fit pre-main sequence age based off of these isochrones.

Compared to the D’Antona and Mazzitelli (1994, 1997) isochrones, the Siess et al. (2000) isochrones show slightly better agreement with the observed locus, especially for stars redder than  $V\text{-}I \sim 1.5$ . In particular, the 14 Myr and 16 Myr isochrones (dashed lines) show reasonably good agreement for  $V\text{-}I \sim 1.75\text{--}2.5$ . In contrast, the 12 Myr and 18 Myr isochrones systematically overpredict and underpredict the luminosities of cluster stars over this range in V-I. Thus, based on the Siess et al. (2000) isochrones for stars with  $V\text{-}I \sim 1.75\text{--}2.5$ ,  $\chi$  Persei has an age of  $\approx 14\text{--}16$  Myr, though this estimate is somewhat uncertain given the poorer fidelity that the isochrones have to the slope of the locus for  $V\text{-}I = 1.5\text{--}2.5$ .

For bluer, earlier stars ( $V\text{-}I \sim 0.75\text{--}1$ ), all Siess et al. (2000) isochrones systematically overpredicts luminosities. Based solely on the apparent position of the pre-main sequence ”turn on” – where the observed locus first becomes brighter than the main sequence – the Siess et al. isochrones would yield an age greater than 20 Myr, which is inconsistent with all other age estimates. Moreover, Siess et al. predicts that over a narrow color range the V band luminosities of cluster stars *increase* with redder color and thus with decreasing mass. We find no clear evidence for such a trend in the data. Likewise, none of the Baraffe et al. (1998) isochrones for  $0.6\text{--}1.4 M_{\odot}$  stars and ages of 1–20 Myr have this trend: it is likely a unique feature of the Siess et al. (2000) models.

In summary, comparing the photometric data with isochrones from D’Antona and Mazzitelli (1994, 1997) and Siess et al. (2000) constrains the age of h and  $\chi$  Persei to be between 10 Myr and 20 Myr. However, the shape of these isochrones in V vs. V-I for any age provide a

significantly poorer match to the observed locus. These comparisons justify our choice of the Baraffe et al. (1998) isochrones to determine pre-MS ages, given their far stronger agreement with the observed cluster locus shape for a wide range of color. Adopting the Baraffe et al. tracks as our benchmark, the D’Antona and Mazzitelli tracks are inaccurate for redder pre-MS stars. They are potentially accurate for bluer, higher-mass pre-MS stars, though this is uncertain given their sparse age sampling. The Siess et al. (2000) tracks yield reasonable age estimates for redder pre-MS stars but are inaccurate for bluer, higher-mass pre-MS stars. If these trends are indicative of the isochrones for all ages, we caution against estimating cluster ages from the main sequence turn-on from the Siess et al. (2000) tracks and against deriving ages from the observed locus of red pre-MS stars from the D’Antona and Mazzitelli (1994, 1997) tracks.

#### 4. Membership in h and $\chi$ Persei

Despite the huge volume of research devoted to studying the Double Cluster, essentially no studies formally list h and  $\chi$  Persei’s main sequence/pre main sequence members. Most membership lists consist of post-main sequence B stars and red supergiants on the cluster field identified by visual inspection, spectroscopy, and proper motions (e.g. Slesnick et al. 2002; Uribe et al. 2002). There has been far less progress in identifying (pre) main sequence cluster members. Nearly all work focused on such stars simply identifies candidate cluster members in different color-color diagrams, without listing these members, or it focuses on particularly x-ray luminous members (Currie et al. 2007a, 2009a).

As demonstrated in previous sections, our spectroscopic and photometric data reveal loci of post-main sequence, main sequence and pre-main sequence stars that are clearly separated from the population of older field stars. These data allow us to identify likely members from optical spectroscopy and VI photometry, greatly expanding upon previous studies. In this section, we determine the first catalog of h and  $\chi$  Persei members that includes main sequence and pre-main sequence stars.

##### 4.1. Method of Membership Determination

Using the dereddened V vs. spectral type HR diagram, we first establish a spectroscopically determined list of h and  $\chi$  Persei members. Because each component of h and  $\chi$  Per has an identical post main sequence and pre-main sequence age, we define the locus of cluster members by joining together the Padova 14 Myr post main sequence isochrone and

the Baraffe 14 Myr pre-main sequence isochrone. The width of the cluster locus is determined by a) the physical extent of the cluster, b) binarity, and c) uncertainties in spectral types. Including the halo population, the h and  $\chi$  Per region extends to at least  $\approx 20\text{--}25'$  away from either cluster center. Assuming a distance modulus of  $\approx 11.8\text{--}11.85$  and spherical distribution of cluster and halo stars, the h and  $\chi$  Persei region is  $\approx 52.5$  pc in diameter, which translates into  $\delta(dM) = \pm 0.05$ . The typical dispersion in  $E(B-V)$  as determined from the V-J, V-H, and V-K colors is  $\lesssim 0.03$ . This uncertainty in  $E(B-V)$  leads to a formal error in the dereddened V magnitude of  $\approx 0.09$  ( $\approx 0.1$ ) for each source, which is larger than the  $\delta(dM)$  from the clusters' physical sizes and slightly widens the  $V_o$  vs. spectral type locus. The uncertainty in the distance modulus is  $\approx 0.08$  (see §3). Equal mass binaries in h and  $\chi$  Per may be up to 0.75 mags more luminous than the cluster locus for single stars. Finally, we compute the median formal spectral type uncertainties as a function of V magnitude and define the width of the locus from left to right by these uncertainties. The uncertainties are  $\approx 2$  subclasses for most spectral types. Therefore, we identify cluster stars in a locus centered on the 14 Myr Padova-Baraffe isochrone with boundaries of -0.75 and +0.2 in V magnitude above and below the isochrone and typically  $\pm 2$  subclasses in spectral type. Figure 25 illustrates.

Second, we identify probable photometric members from the V vs. V-I color-magnitude diagram again using the 14 Myr Padova-Baraffe isochrone reddened by the median average cluster reddenings. The upper bound defining the cluster locus is the same as before; for the lower bound, we choose the larger of 0.05 (the physical size of the clusters in mags) and the V band uncertainty. We choose the boundaries in color assuming that the dispersion in reddening ( $\approx 0.1$  mag) and photometric errors in V-I color ( $(\sigma_V^2 + \sigma_I^2)^{0.5}$ ) widen the locus. The dispersion in  $E(B-V)$  translates into a dispersion of 0.125 mags in V-I. The median errors in color range from  $\lesssim 0.01$  mags at  $V \leq 10\text{--}12$  to 0.08 mags at  $V = 23$ . Therefore the widening of the left/right boundaries of the locus from these two sources of error bound of the locus increases from  $\sim 0.125$  mags for bright stars to  $\sim 0.2$  mags for faint stars. Figure 26 illustrates the region within which we identify probable members.

## 4.2. Membership Estimates

**Spectroscopic Membership** –Based on our selection criteria, we identify a total of 4,702 stars as spectroscopic members:  $\sim 63\%$  of the 7,465 spectroscopically observed stars with V-band photometry. The frequency of members is highest for the cluster-dominated regions. Within  $10'$  of the h Persei center, 71% (1138/1606) of stars are members. Within  $10'$  of the  $\chi$  Persei center, 68% (906/1330) of stars are members. The slightly lower membership

frequency of 59% (2676/4529) in the low-density halo regions is consistent with the region’s greater level of field star contamination.

**Photometric Membership** – The number of photometric candidate members is substantial: 14,307 stars, or  $\sim 30\%$  of the 47,060 stars on the field. Over half of these stars reside in the low-density regions surrounding the cluster cores (8,817, or 62% of the total population). The other candidates are almost evenly split between those within  $10'$  of the h Persei center (2,724) and  $10'$  of the  $\chi$  Persei center (2,766). Within both core-dominated regions, about 40% of stars are probable members: 2724/6519 for h Persei and 2766/6674 for  $\chi$  Persei. As with the spectroscopic sample, field contamination is far heavier in the halo region:  $\sim 26\%$  of halo-region stars are consistent with membership (8817/33867).

Taken at face value, these results seem to contradict Currie et al. (2007a) and Currie (2008) who argue that the core-dominated regions have as many stars as the halo. Furthermore, they conflict with previous studies showing that h Persei is  $\sim 30\%$  more massive/populous than  $\chi$  Persei (e.g. Slesnick et al. 2002; Bragg 2004; Bragg and Kenyon 2005). The first difference is one of semantics: both papers identify the halo region with stars at distances greater than  $15'$  away from either cluster center and extending to  $25'$  distant, not  $10'$  as in this paper. Adopting the previous definition of the core and halo regions yields much more similar results. For example, the number of photometric members would be 4808 (out of 14567) for the h Persei core, 4993 (out of 15,026), for the  $\chi$  Persei core, and 4283 (out of 17,467) for the h and  $\chi$  Per halo population. We primarily adopt  $10'$  as the core boundary because the density of stars is low (Currie et al. 2007a) and our spectroscopic survey is unbiased within this radius, though we consider either definition to be reasonable.

The conflicting results for cluster richness are probably due to survey incompleteness near the h Persei core. The h Persei core has a higher density of early, bright stars (e.g. Currie et al. 2007a; Bragg and Kenyon 2005; Slesnick et al. 2002). The scattered light from these stars reduces the contrast between faint, low-mass stars and the background, which restrict source detection to a brighter limit than for the  $\chi$  Persei core. Restricting our analysis to brighter stars recovers previous results. For example, we identify 607 stars brighter than  $V = 16$  – likely earlier than A2 (see Figure 9)– within the h Persei core as photometric members but only 469 within the  $\chi$  Persei core as members. Adopting these criteria implies that h Persei is  $\sim 30\%$  more massive, in complete agreement with previous results. Assuming the standard h Per to  $\chi$  Per mass ratio, there are 700 more lower-mass h Per stars unaccounted for by our survey, bringing the total number to  $\sim 3424$ .

### 4.3. Membership Estimates Corrected for Field Star Contamination

Some stars identified as members are likely interlopers. In the HR diagrams and color-magnitude diagrams presented here, the locus of cluster stars intersects the main locus of field stars around G spectral types. Thus, we expect some field star contamination among G stars. The increasing scatter of the colors of field stars with increasing V probably also leads to some contamination along the lower boundary of the pre-main sequence locus in V/V-I. We cannot subtract a field star population from the cluster population and estimate the number of interlopers, because the halo region fills the entire optical survey.

Comparing the membership results for stars based on photometry and spectroscopy yields an estimate of the field star contamination in the photometric member list. There are 3,984 stars identified as candidate photometric members *and* spectroscopic members; 763 stars identified as candidate members from photometry are rejected as members based on spectroscopy. Therefore, about  $\sim 16\%$  of the photometric member list is comprised of interloping field stars, not bona fide cluster members. Even though field contamination is greater for fainter magnitudes, analysis in §3.3 demonstrates that the region defining the locus of low-mass h and  $\chi$  Per stars ( $V \sim 18\text{--}24$ ,  $V\text{-I} \sim 1.5\text{--}4$ ) is less contaminated than the region ( $V \sim 16.5\text{--}17.5$ ,  $V\text{-I} \sim 1\text{--}1.5$ ) comprising most of our spectroscopically observed members.

The number of B stars can also be used to estimate contamination. Because early to mid B dwarf stars identified as members above cannot be old field stars, they are highly likely to be young cluster members. Assuming a cluster mass function (e.g. Miller-Scalo), the number of B stars yields an expected number of total cluster stars. By comparing the ratio of the expected number of members to the derived number of members, we estimate the number of field stars misclassified as members/candidate members. We choose the B0–B6 star population in the halo as our reference, assume that the B0–B6 star population extends to  $V \sim 13.45$  (cf. Figure 9) and assume that the field star density is independent of position. Main sequence B6 stars should have masses of  $\approx 4 M_{\odot}$  (or  $\log(M_{\star}/M_{\odot}) \approx 0.6$ )<sup>8</sup>. We assume that our survey reaches stars with masses  $\approx 0.2 M_{\odot}$  ( $\log(M_{\star}/M_{\odot}) \sim -0.7$ ): this lower limit is higher than that determined in §3.3 ( $\sim 0.1\text{--}0.15 M_{\odot}$ ) but is chosen to be conservative. We derive the expected number of cluster stars using Table 9 in Miller and Scalo (1979).

The halo population includes 217 candidate members brighter than  $V = 13.45$ , so it should contain about 7,380 stars total. Compared to the 8,817 stars listed as candidate

---

<sup>8</sup>The Padova isochrones list  $T_e \sim 14,600$  K for  $4 M_{\odot}$  main sequence stars, which places at a spectral type of  $\approx B5.75$  on our  $T_e$  scale.

members, the percentage of interloping field stars is also  $\sim 16\%$ , which is essentially identical to the estimate derived by comparing membership lists. Because the area of the photometric survey consisting of the halo region is  $\approx 0.43$  square degrees –  $0.6 \text{ sq. deg} - 2 \times \pi 10'^2$  – the density of interloping field stars is  $\sim 3,381 \text{ deg}^{-2}$ , which yields  $\sim 295$  interlopers in each core region. Thus, within our 0.6 square-degree field there are probably 3,129 cluster members for h Persei, 2,471 for  $\chi$  Persei, and 7,380 for the low-density halo, yielding a total of 12,980 stars in h and  $\chi$  Persei. If lower-mass halo stars associated with the halo cover one square degree on the sky, consistent with our spectroscopic membership results for higher-mass stars, *then h and  $\chi$  Persei may contain up to  $\approx 20,000$  members.*

Several other factors indicate that our membership estimate is reasonable and conservative. First, the color-magnitude diagram boundaries identifying photometric members assume that all h and  $\chi$  Per stars have  $E(B-V)$  within 0.1 mag of the derived median values for each core region and the halo. However, our spectroscopic membership list clearly identifies some members with reddening outside this range. It is plausible that other members lacking spectroscopic data lie outside the photometric membership boundaries but would deredden to the cluster locus. Second, analysis in §3.3 indicates that our survey may have reached close to the hydrogen burning limit ( $\approx 0.1 M_{\odot}$ ). If so, then the expected number of cluster stars determined from extrapolating the cluster IMF from the B star population will be slightly greater than derived in this section. Because more cluster stars are expected, the number of interlopers drops. Third, because the regions identifying members are defined purely by analysis uncertainties, we implicitly assume that all 13,000–20,000 stars in h and  $\chi$  Persei formed simultaneously. Analysis in §3 indicates that the median age of h and  $\chi$  Per stars is 14 Myr with no evidence for a substantial age spread. However, our analysis cannot preclude the existence of smaller, 1–2 Myr age spreads (see also discussion in Slesnick et al. 2002). Even 1–2 Myr age spreads would widen the cluster loci and cause us to underestimate the true number of members.

#### 4.4. Combined Membership List

After removing the 763 candidate photometric members rejected by spectroscopy, we compile a final membership list of 14,160 stars including both types of members. For each entry, we list ID numbers, the position, optical photometry, spectral types, and reddening. Table 6 lists the members of h and  $\chi$  Persei.

## 5. The Mass and Structure of $\eta$ and $\chi$ Persei

Using our membership lists, we can explore other bulk properties of the Double Cluster: its mass and spatial distribution. Following previous investigations (Slesnick et al. 2002; Bragg and Kenyon 2005), we estimate the total cluster mass by determining the total mass in stars above some mass limit and extrapolating to lower masses by assuming a cluster mass function. The spatial distribution of photometric members reveals complex structure in the regions with a high density of cluster stars. By comparing the number of stars with different masses, we probe the clusters’ mass segregation, which yields information in their formation histories.

### 5.1. Cluster Mass

With a list of spectroscopically confirmed members, we estimate the total mass of  $\eta$  and  $\chi$  Persei and probe the spatial distribution of cluster stars in core-dominated regions. To determine the mass, we add up the derived masses of stars earlier than B6 ( $4 M_{\odot}$ ), assume a Miller-Scalo IMF, calculate the masses of the core regions, and use the ratio of members in the core and halo to determine the total mass. We use the spatial density of cluster stars to investigate mass segregation.

From these assumptions, we derive a mass of  $4,704 M_{\odot}$  for the  $\eta$  Persei core and  $3,699 M_{\odot}$  for the  $\chi$  Persei core. Assuming the ratio of the core populations to the halo ( $5600/7380$ ), the halo population has a total mass of  $11,074 M_{\odot}$ . Not including the halo regions beyond our photometric coverage, the total mass of  $\eta$  and  $\chi$  Persei is  $\approx 19,477 M_{\odot}$ : an order-of-magnitude larger than the Orion Nebula Cluster and the Pleiades.

Our deep spectroscopic survey supports the conclusion of Slesnick et al. (2002) that the  $\eta$  and  $\chi$  Persei region is unique in mass and structure among nearby ( $d < 3$  kpc) regions and much more similar to other massive ‘double clusters’ such as NGC 1818 in the Large Magellanic Cloud (Johnson et al. 2001) and massive single clusters such as the Arches cluster near the galactic center (Figer et al. 1999).

### 5.2. Mass Segregation

Mass segregation also probes cluster structure. Dynamical mass segregation occurs because cluster members gravitationally attract one another, exchanging kinetic energy and momentum, which tends to drive the system into energy equipartition. As the cluster ages,

this process leaves more massive cluster stars more concentrated in the cluster core and less massive stars concentrated in lower-density regions. Alternatively, clusters may exhibit *primordial* mass segregation, which occurs as an outcome of the cluster formation process.

To probe mass segregation, we compute the relative number of B star members to A and F star members as a function of distance from the cluster centers. If the clusters lack mass segregation, then the ratio of B stars to A/F members should be nearly constant with distance. Clusters with mass segregation should have a decreasing ratio with cluster-centered distance.

As shown in Figure 27, both clusters exhibit some evidence for mass segregation. The strongest evidence is for h Persei stars (top) within  $\approx 3\text{--}4'$  of the cluster center. Within this region, the relative number of B stars to A stars drops from  $\sim 4.5$  within  $1'$  to  $\sim 2$  for larger distances. The ratio of A stars to F stars is also highest within  $2'$  and reaches a constant level ( $\sim 0.5\text{--}1$ ) by  $\sim 3'$ . The ratio of the number of B stars to F stars, comparing a wider range in masses ( $\geq 2.2 M_{\odot}$  to  $1.35\text{--}1.5 M_{\odot}$ ), varies the most, exceeding 22 within  $1'$  and reaching constant levels at distances greater than  $4'$ . In all cases, the high number of B stars to later stars implies that higher-mass stars are preferentially concentrated in the cluster centers, consistent with the cluster being mass segregated.

For  $\chi$  Persei, the extent of mass segregation and the physical scale over which it occurs may be comparatively smaller. The ratio of B stars to F stars is high ( $\sim 4\text{--}14$ ) within  $2'$  of the cluster center and drops to a constant level by  $3'$ . The ratios of B stars to A stars and A stars to F stars is high for stars within  $2'$  of the cluster center after which they reach constant levels. These trends are qualitatively similar to those found for h Persei. However, the smaller B/F star ratio in the cluster center and slightly smaller radius beyond which the ratio is constant ( $3'$  vs.  $4'$  for h Per) indicates that mass segregation in  $\chi$  Persei is not as strong as it is in h Persei (see also Slesnick et al. 2002; Bragg and Kenyon 2005).

Comparing the dynamical mass segregation timescales with cluster ages determines whether mass segregation must be primordial or dynamical. Dynamical mass segregation occurs on relaxation timescales (Binney and Tremaine 1987), which for h and  $\chi$  Persei is:

$$t_{relax} \sim \frac{1.8 \times 10^{10} yr}{\ln \Lambda(r)} \left[ \frac{\sigma(r)}{10 km s^{-1}} \right]^3 \left( \frac{1 M_{\odot}}{m} \right) \left[ \frac{10^3 M_{\odot} pc^{-3}}{\rho(r)} \right], \quad (23)$$

where  $\Lambda$  is the number of stars interior to radius  $r$ ,  $\sigma$  is the velocity dispersion,  $m$  is the typical stellar mass ( $0.63 M_{\odot}$ ), and  $\rho(r)$  is the stellar density. Bragg and Kenyon (2005) compute a relaxation timescale of  $\sim 15$  Myr for h Persei at a core radius of  $2.8'$  and  $\sim 20$  Myr for  $\chi$  Persei at a core radius of  $3.5'$ . The age of h Persei is almost identical to its relaxation timescale at  $2.8'$  from the cluster center. While the age of  $\chi$  Persei is 5 Myr less than its

relaxation timescale, the cluster only clearly exhibits mass segregation at distances within 2'–3' from the cluster center. Because the relaxation timescale is inversely proportional to stellar density and the natural log of the number of stars, the relaxation timescale for regions interior to 2'–3' is much less than 20 Myr. Conversely, even though the relaxation timescale rises well above 15–20 Myr for distances greater than 3'–4', there is little evidence for mass segregation at these separations. Thus, it is not clear whether mass segregation in h and  $\chi$  Persei must be primordial. Similarly, for the Arches cluster it is not clear whether mass segregation is primordial or dynamical.

## 6. Summary and Future Work

### 6.1. Summary of Analysis and Major Findings

This paper describes the first extensive photometric and spectroscopic survey of main sequence and pre-main sequence stars in h and  $\chi$  Persei. By analyzing optical photometry for 47,000 stars and spectroscopy of 11,000 stars, we derived the median reddening, distance modulus, and age for each component of h and  $\chi$  Per. We then constructed the first extensive membership list of h and  $\chi$  Per stars, ranging from massive B–M supergiants to pre-main sequence stars whose masses are likely comparable to the hydrogen burning limit. Our study yields the following major results:

- The median reddening values for the h Persei core,  $\chi$  Persei core, and halo region are comparable:  $E(B-V) \sim 0.55$ ,  $E(B-V) \sim 0.52$ , and  $E(B-V) \sim 0.52$ , respectively.
- The distance moduli for h Per,  $\chi$  Per, and the halo region are also nearly identical:  $dM_{hPer} = 11.8$ ,  $dM_{\chi Per} = 11.85$ , and  $dM_{halo} = 11.85$ .
- Ages for all three components of h and  $\chi$  Persei are identical:  $\sim 14$  Myr. Moreover, post-main sequence ages and pre-main sequence ages for each component are identical. Thus, the properties of h and  $\chi$  Persei are consistent with the coeval cores and the low-density halo population emerging from a single, explosive star-forming event.
- Within 10' of the two cluster centers, the Double Cluster contains at least  $\sim 5,000$  stars; h Persei is about 30% more populous than  $\chi$  Persei. The halo region contains at least  $\sim 7,000$  stars and as many as 15,000 stars, bringing the total number of stars in h and  $\chi$  Persei to  $\sim 20,000$ . The estimated masses for h Persei,  $\chi$  Persei, and the halo region are  $\sim 4,700 M_{\odot}$ ,  $\sim 3,700 M_{\odot}$ , and  $\sim 11,000 M_{\odot}$ .

- Both clusters show clear evidence of mass segregation within 3' of the cluster centers, though it is stronger for h Persei. The relaxation timescales for both clusters are comparable to or less than their ages within 3'. Therefore, mass segregation may either be primordial or dynamical.

These results support and extend recent studies of h and  $\chi$  Per conducted by Currie et al. (2009a), Mayne et al. (2007), Currie et al. (2007a), Bragg and Kenyon (2005), Slesnick et al. (2002), and Keller et al. (2001). Remarkably, four mutually exclusive sets of authors using different techniques converge on essentially the same properties for the clusters' reddening, distance, and age. Combined with previous work, our results clearly refute earlier claims that the Double Cluster and its environs have a substantial age spread (Wildey 1964; Marco and Benabean 2001), have a substantially different age (Schild 1965, 1967; Marco and Benabean 2001), or are located at substantially different distances (Schild 1967; Kharchenko et al. 2005). All indications are that the different components of h and  $\chi$  Persei substantially differ only by spatial distribution and mass.

## 6.2. Future Research on the Stellar Population of h and $\chi$ Persei

In addition to advancing our understanding of h and  $\chi$  Persei properties, this study clearly identifies advances needed to paint a more complete picture of the Double Cluster. We highlight several promising areas of future research below:

- **Wide-Field Optical Photometry/Deep Optical Spectroscopy** – Simple wide-field optical photometric surveys can easily expand our membership list and amplify the scientific output of our work. The mismatch in survey area between our spectroscopy ( $\sim 1$  square degree) and photometry ( $\sim 0.6$  square degrees) leaves  $\sim 3500$  stars with spectroscopy but no photometry. Our results demonstrate the need for high-quality photometry to measure reddening and to establish membership. Because nearly all of these stars are bright ( $V \lesssim 19$ ), they are easily accessible by wide-field cameras on 1–2 meter-class telescopes.

The upper main sequence of halo stars is undersampled largely because of our selection criteria for Hectospec targets ( $J \geq 14$ ). Added to our existing survey, the entire upper main sequence of h and  $\chi$  Persei can probably be probed after a few additional Hectospec or Hydra fiber settings. Because these stars are extremely bright, obtaining high signal-to-noise spectra will be trivial.

Furthermore, our optical photometry identifies many probable cluster members that are beyond the 2MASS detection limit but clearly within range of Hectospec for integration

times of  $\sim 1$ – $2$  hours ( $V \lesssim 21$ – $22$ ). A survey establishing the spectral types for many of these stars would provide valuable information on the luminosity and temperatures of pre-main sequence stars at  $\approx 14$  Myr. Other multi-object spectrographs coming online in the near future (e.g. MODS on the Large Binocular Telescope, Binospec on the MMT) can probe even further down the cluster mass function.

- **Robust Membership Determinations from *SIM* and *GAIA*** –

Proper motion studies are the most definitive method for determining h and  $\chi$  Per membership. Unfortunately, at  $\sim 2.3$  kpc distant, h and  $\chi$  Per stars exhibit tiny proper motions, the size of which render ground-based campaigns to verify our membership list hopeless. However, space-based interferometric missions – specifically *SIM* and *GAIA* – are easily capable of detecting the  $\sim \mu$ -arc second motions of pre-main sequence cluster stars. *SIM*'s and *GAIA*'s clear ability to yield definitive catalogs of members for h and  $\chi$  Persei and other distant, populous clusters would have an enormous impact on studies of these clusters and stellar evolution in general.

- **Metallicity** – Clearly, the greatest source of systematic error in constraining the clusters' properties is metallicity. While we argue that h and  $\chi$  Per likely have a near-solar metallicity, it is possible that the sources whose properties support our contention are not indicative of the clusters' stars as a whole. To address metallicity, at least three avenues of research should be explored. First, sophisticated stellar atmosphere modeling of stars in a variety of evolutionary states should constrain the photospheric chemical abundances (e.g. Dufton et al. 1990; Smartt and Rolleston 1997; Venn et al. 2002) and help to define the typical chemical composition. Second, high-resolution echelle spectra of cluster stars (e.g. with Hectochelle), especially G-type pre-main sequence members, should not only constrain the clusters' velocity dispersions (and thus aid membership identification) but will also be capable of yielding metallicity estimates. Third, building upon work by Southworth et al. (2004a,b), metallicities can be estimated by comparing masses and radii of eclipsing binaries to model predictions. In this regard, results from the MONITOR program (Aigrain et al. 2007) may be crucial for ending the debate on metallicity.

- **Effective Temperatures** – As described in Appendix A, the  $T_e$  scale for early B dwarfs and evolved B stars is more poorly constrained than for O stars and A–M stars. Non-LTE modeling of the many early B stars in h and  $\chi$  Persei may provide better constraints on the  $T_e$  scale. More specifically, determining  $T_e$  for individual B stars strengthens our ability to derive accurate post-main sequence ages. As was argued by Slesnick et al. (2002) and can be seen in Figures 16–18, the binning of B stars into discrete  $T_e$  values for their spectral type potentially introduces a spurious spread in

$T_e$  at a given  $V$  magnitude brightness, which could be misinterpreted as a spread in age. Individual measurements for  $T_e$  will tighten the locus of cluster stars at the main sequence turnoff. Accurate  $T_e$  estimates may be especially important for cluster Be stars, which are often difficult to spectral type because of their Balmer line emission. A large campaign to derive atmospheric properties of Be stars in  $h$  and  $\chi$  Persei is underway (Marsh et al. 2010).

- **The Halo Population** – While our results confirm previous claims (e.g. Currie et al. 2007a) that  $h$  and  $\chi$  Persei contains a large halo population, it is possible that the halo extends beyond 25–30' from either cluster center, or even well beyond the square-degree field covered by our spectroscopic survey. A more spatially extended survey of stars would yield a better estimate for the total mass of the halo population. A more complete census of young stars within  $\approx 5$  degrees of the  $h$  and  $\chi$  Persei cores better reveals the large star formation history within which  $h$  and  $\chi$  Per emerged, including the Double Cluster's relationship to other nearby young clusters such as W3, W4, and W5 located several degrees away. Specifically, it may be possible to address the relationship between  $h$  and  $\chi$  Persei and the Perseus OB1 association, determining if the core and halo populations have properties completely distinct from Per OB1, if  $h$  and  $\chi$  Per represents a unique epoch in star formation that propagated through the present day Per OB1 region, or if its properties are characteristic of the Per OB1 association as a whole (e.g. Slesnick et al. 2002; Lee and Lim 2008).
- **The Circumstellar Disk Population: Constraints on Planet Formation** – Finally, the large sample of stars now confirmed as  $h$  and  $\chi$  Persei members can be used to investigate planet formation by using Spitzer and (later) the James Webb Space Telescope. New Spitzer observations reveal an order-of-magnitude increase in the number of stars detected at 3.6–8  $\mu m$  (Currie et al. 2010). Combined with membership information derived here, Spitzer data will yield constraints on the disk population from a sample size easily dwarfing that of the *FEPS* and *Cores-to-Disks* Legacy Programs combined and thus providing far superior statistical reliability.

This fundamentally different kind of dataset allows robust probes of planet formation that are impossible with other samples, providing estimates of the frequency of long-lived protoplanetary disks; warm, terrestrial planet-forming debris disks; and extremely luminous cold debris disks. Combined with data from 5–25 Myr-old clusters – e.g. NGC 2362, Upper Scorpius, Orion OB1, NGC 1960, and NGC 2232 (Currie et al. 2009b; Carpenter et al. 2006; Hernandez et al. 2007b; Balog et al. 2010; Currie et al. 2008b) – it is possible to reconstruct the time history of terrestrial, gas giant, and icy planet formation to compare with our solar system's chronology and models of planet formation (e.g. Kenyon and Bromley 2009; Castillo-Rogez et al. 2007).

We thank the MMT CfA Time Allocation Committee and the MMT director Faith Vilas for their enthusiastic, unwavering support for this project over the past 3 years. The MMT staff, telescope operators, and Hectospec instrument team — especially Nelson Caldwell and Dan Fabricant — provided superb technical support. We thank Doug Mink for constructing a searchable public archive of our Hectospec data. Our work is deeply indebted to the sound advice of many experts in the field of stellar atmospheres and evolution. In particular, we thank Phil Massey for patiently and rapidly answering many questions posed by the lead author regarding effective temperatures of OB main sequence stars, giants, and supergiants. We also thank Robert Kurucz for many detailed, valuable discussions concerning the sensitivities of observed colors and luminosities to chemical abundances, surface gravities, and evolutionary states. Finally, we thank Steven Cranmer for sharing his nearly encyclopedic knowledge of effective temperature scales from the past 30 years of research literature.

## REFERENCES

- Aigrain, S., et al., 2007, *MNRAS*, 375, 29
- Allard, F., et al., 2000a, in *Proc. of From Giant Planets to Cool Stars*, ed. C. A. Griffith, & M. S. Marley, *ASP Conf. Ser.* 212, 127
- Allard, F., Hauschildt, P. H., Schwenke, D., 2000b, *ApJ*, 540, 1005
- Balog, Z., Currie, T., Rieke, G., et al., 2010, *ApJ* in prep.
- Baraffe, I., et al., 1998, *A&A*, 337, 403
- Barden, S., et al., 1993, *PASP*, 37, *Fiber Optics in Astronomy II*, ed. P. M. Gray (San Francisco: ASP), 185
- Bertelli, G., et al., 1994, *A&AS*, 106, 275
- Bessell, M., 1979, *PASP*, 91, 543
- Bessell, M., Brett, J., 1988, *PASP*, 100, 1134
- Bessell, M., 1990, *PASP*, 102, 1181
- Bessell, M. S., et al., 1998, *A&AS*, 77, 1
- Bessell, M. S., 2005, *ARA&A*, 43, 293
- Binney, J & Tremaine, S., 1987, *Galactic Dynamics* (Princeton: Princeton Univ. Press)

- Bohm-Vitense, E., 1981, *AJ*, 19, 295
- Bragg, A. & Kenyon, S., 2002, *AJ*, 124, 3289
- Bragg, A., 2004, Ph.D. thesis, Harvard University
- Bragg, A. & Kenyon, S., 2005, *AJ*, 130, 134
- Capilla, G. & Fabregat, J., 2002, *A&A*, 394, 479
- Cardelli, J., et al., 1989, *ApJ*, 345, 245
- Carpenter, J., 2001, *AJ*, 121, 2851
- Carpenter, J., et al., 2006, *ApJ*, 651, 49L
- Castelli, F., Kurucz, R. L., 1994, *A&A*, 281, 817
- Castelli, F., Kurucz, R. L., 2003, arXiv:0405087
- Castillo-Rogez, J., Matson, D., Sotin, C., Johnson, T. V., Lunine, J., Thomas, P., 2007, *Icarus*, 190, 179
- Claret, A., 1995, *A&AS*, 109, 441
- Code, A., et al., 1976, *ApJ*, 203, 417
- Crowther, P., 1997, *IAU Symposium*, 189, 137
- Crowther, P., Lennon, D. J., Walborn, N. R., 2006, *A&A*, 446, 279
- Currie, T., et al., 2007, *ApJ*, 659, 599
- Currie, T., et al., 2007, *ApJ*, 663, 105L
- Currie, T., et al., 2007, *ApJ*, 669, 33L
- Currie, T., 2008, Ph. D. thesis, University of California-Los Angeles
- Currie, T., et al., 2008, *ApJ*, 672, 558
- Currie, T., Plavchan, P., Kenyon, S. J., 2008, *ApJ*, 688, 597
- Currie, T., Evans, N. R., et al., 2009, *AJ*, 137, 3210
- Currie, T., Lada, C. J., et al., 2009, *ApJ*, 698, 1

- Currie, T., 2009, ApJ, 694, 171L
- Currie, T., Kenyon, S. J., 2009, AJ, 138, 703
- Currie, T., Rieke, G. H., Kenyon, S. J., et al., 2010, ApJ, in prep
- D’Antona, F., Mazzitelli, I., 1994, ApJS, 90, 467
- D’Antona, F., Mazzitelli I., 1997, Memorie della Societa Astronomia Italiana, Vol. 68, p. 807
- de Jager, C., Nieuwenhuijzen, H., 1987, A&A, 177, 217
- Dougherty, S., et al., 1991, AJ, 102, 1753
- Dougherty, S., et al., 1994, A&A, 290, 609
- Dufton, P.L., Brown, P.J.F., Fitzsimmons, A., Lennon, D.J., 1990, A&A, 232, 431
- Fabricant, D., et al., 1998, PASP, 110, 79
- Fabricant, D., et al., 2005, PASP, 117, 1411
- Figer, D., et al., 1999, ApJ, 525, 750
- Fitzpatrick, E. L., Massa, D., 2005, AJ, 129, 1642
- Fluks, M. A., et al., 1994, A&AS, 105,311
- Girardi, L., et al., 2002, A&AS, 391, 195
- Gray, R. O., Corbally, C. J., 1994, AJ, 107, 742
- Gray, R. O., Corbally, C. J., 2009, Stellar Spectral Classification (Princeton, NJ: Princeton Univ. Press)
- Hernandez, J., et al., 2004,AJ, 127, 1682
- Hernandez, J., et al., 2007a, ApJ, 662, 1067
- Hernandez, J., et al., 2007b, ApJ, 671, 1784
- Humphreys, R., 1978, ApJS, 38, 309
- Humphreys, R., McElroy, D., 1984, ApJ, 284, 565
- Indebetouw, R., et al., 2005, ApJ, 619, 931

- Irwin, M., 1985, MNRAS, 214, 575
- Irwin, M., Lewis, J., 2001, New Astronomy, 45, 105
- Irwin, J., et al., 2006, MNRAS, 370, 954
- Irwin, J., Irwin, M., Aigrain, S., Hodgkin, S., Hebb, L., Moraux, E., 2007, MNRAS, 375, 1449
- Jacoby, G., et al., 1984, ApJS, 56, 257
- Johnson, H. L., Morgan, W. W., 1953, ApJ, 117, 313
- Johnson, H. L., 1965, ApJ, 141, 923
- Johnson, R., Beaulieu, S., and Gilmore, G., MNRAS, 324, 367
- Keller, S.C., et al., 2001, AJ, 122, 248
- Kenyon, S., Bromley, B., 2009, ApJ, 690, 140L
- Kenyon, S. & Hartmann, L., 1995, ApJS, 101, 117
- Kharchenko, N. V., et al., 2005, A&A, 438, 1163
- Kilian, J., et al., 1992, A&A, 262, 171
- Kurucz, R. L., in The Stellar Populations of Galaxies, in IAU Symposium 149, edited by B. Barbuy and A. Renzini (Kluwer, Dordrecht), p. 225
- Lee, H-T., Lim, J., 2008, ApJ, 679, 1352
- Lejeune, Th., et al., A&AS, 1998, 130, 65
- Levesque, E., et al., 2005, ApJ, 628, 973
- Marigo, P., Girardi, L., Bressan, A., Groenewegen, M. A. T., Silva, L., Granato, G. L., 2008, A&A, 482, 883
- Marsh, A., McSwain, V., Currie, T., 2010, arXiv:0910.0275
- Marco, A. & Benabeau, 2001, A&A, 372, 477
- Massey, P., et al., 2005, ApJ, 627, 477
- Mathis, J., 1990, ARA&A, 28, 37

- Mayne, N. J., Naylor, T., Littlefair, S. P., Saunders, E. S., Jeffries, R. D., 2007, MNRAS, 375, 1220
- Mayne, N. J., Naylor, T., 2008, MNRAS, 386, 261
- Miller, G., & Scalo, J., 1979, ApJS, 41, 513
- Payne, C. H., 1924, Nature, 113, 783
- Payne, C. H., 1925, Ph.D. thesis, Radcliffe College
- Payne, C. H., Williams, E. T. R., 1929, MNRAS, 89, 526
- Schaller, G., et al., 1992, A&AS, 96, 269
- Schild, R., 1965, ApJ, 142, 979
- Schild, R., 1967, ApJ, 148, 449
- Schmidt-Kaler, Th., 1982
- Siess, L., et al., 2000, A&A, 358, 593
- Slesnick, C., et al., 2002, ApJ, 576, 880
- Smartt, S., Rolleston, W. R., 1997, ApJ, 481L, 47
- Southworth, J., Maxted, P.F.L., Smalley, B., 2004, MNRAS, 349, 547
- Southworth, J., Zucker, S., Maxted, P. F. L., Smalley, B., 2004, MNRAS, 355, 986
- Uribe, A., et al., 2002, PASP, 114, 233
- Venn, K., et al., 2002, ApJ, 565, 571
- Vrancken, M., Lennon, D. J., Dufton, P. L., Lambert, D. L., 2000, A&A, 358, 639
- Willey, R., 1964, ApJS, 8, 439
- Wolf, N. J., Stein, W. A., Strittmatter, P. A., 1970, A&A, 9, 252
- Walborn, N., 1971, ApJS, 23, 257

Table 1. Optical Photometry Catalog

Running Number	RA	DEC	$t_{int.,V}$	V	$\sigma(V)$	Photometry Flag (V)	$t_{int.,I_c}$	I <sub>c</sub>	$\sigma(I_c)$	Photometry Flag (I <sub>c</sub> )
1	35.6018	57.1095	2	7.8257	0.0001	-9	2	6.3208	0.0000	-9
2	35.7515	57.3870	2	7.1912	0.0000	-9	2	6.5893	0.0000	-9
3	34.7691	57.1355	2	7.1731	0.0000	-9	2	6.6876	0.0000	-9
4	35.4814	57.2429	2	7.2686	0.0000	-9	2	6.7332	0.0000	-9
5	35.2484	57.1583	2	7.7409	0.0001	-9	2	6.7185	0.0000	-9

Note. — The photometry flags have the following meanings: -1 = unsaturated, uncrowded, -2 = crowded, PSF fitting used, -9 = likely saturated.

Table 2. Spectroscopy Catalog

Running Number	Source	RA	DEC	Numerical Spectral Type	Spectral Type Uncertainty	J	$\sigma(J)$	H	$\sigma(H)$	$K_s$	$\sigma(K_s)$
1	2	35.4850	57.1471	29.00	3.00	13.3940	0.0450	13.2400	0.0380	13.0114	0.1614
2	2	35.6214	57.2132	29.00	3.00	13.8380	0.0420	13.7570	0.0490	13.5912	0.0256
3	2	35.0118	57.0850	38.50	2.00	11.0890	0.0270	10.8950	0.0210	10.7218	0.0433
4	2	34.8023	57.1390	35.00	3.00	13.2410	0.0420	13.1680	0.0390	12.8050	0.0170
5	2	35.3507	57.2118	22.00	1.90	13.3940	0.0410	13.3100	0.0420	13.1569	0.0821

Note. — The numerical spectral type has the following formalism: 10=B0, 11=B1 ... 68=M8. The spectral type uncertainty is given in subclasses. The **Source** column refers to the source of the spectroscopic data: Hectospec (1), Hydra (2), FAST (3), or Slesnick et al. (2002) (4).

Table 3. Combined Catalog for Stars with Optical Photometry and Spectroscopy

ID Number	RA	DEC	Numerical Spectral Type	Spectral Type Uncertainty	E(B-V)	Luminosity Class	J	$\sigma(J)$	H	$\sigma(H)$	$K_s$	$\sigma(K_s)$	V	$\sigma(V)$	$I_c$	$\sigma(I_c)$
1	35.4684	56.9050	6.50	2.00	0.479	5	8.5170	0.0100	7.6218	0.0001	8.1270	0.0270	8.1320	0.0420	8.1240	0.0260
2	34.7945	57.0249	10.50	1.60	0.532	1	9.8700	0.0100	8.6622	0.0002	9.2100	0.0270	9.1150	0.0290	9.1350	0.0210
3	34.6782	57.0726	10.50	1.50	0.610	3	10.6020	0.0100	9.6145	0.0004	9.8270	0.0250	9.8030	0.0290	9.7900	0.0230
4	34.3963	57.0857	10.50	1.80	0.437	5	9.9250	0.0100	8.6521	0.0002	9.5030	0.0240	9.5510	0.0300	9.5290	0.0220
5	34.7768	57.1261	11.00	1.50	0.594	5	9.8200	0.0100	-99.0000	0.0000	9.0430	0.0320	8.9980	0.0320	8.9740	0.0200

Note. — The luminosity class has the following meaning: 1= Class I supergiant, 3 = Class III giant, and 5 = Class V dwarf.

Table 4. Distance Moduli for h and  $\chi$  Persei from this work and from previous work

Cluster Properties Used	h Persei distance	$\chi$ Persei distance	Halo distance
This Work			
$V_o$ vs. Spectral Type	11.80	11.85	11.85
$V_o$ vs. $\log(T_e)$	11.80	11.85	11.85
$V_o$ vs. $V_o-I_o$	11.82	11.87	11.87
$V_o$ vs. $V_o-J_o$	11.80	11.85	11.85
$V_o$ vs. $V_o-H_o$	11.79	11.84	11.84
$V_o$ vs. $V_o-K_o$	11.82	11.86	11.87
average value	11.80	11.85	11.85
Literature Estimates			
Mayne et al. (2008)	11.78	11.82	–
Slesnick et al. (2002)	11.85	11.85	11.08–12.42
Uribe et al. (2002)	11.84	11.84	–
Capilla and Fabregat (2002)	11.70	11.70	–
Keller et al. (2001)	11.75	11.75	–
Marco and Benabeau (2001)	11.66	11.56	–

Table 5. Stellar Age Estimates for h and  $\chi$  Persei

Method	Isochrones	Cluster Properties Used	h Persei age (Myr)	$\chi$ Persei age (Myr)	Halo age (Myr)
This Work					
Main Sequence Turnoff (B stars)	Padova post-MS $V_o$ vs. $\log(T_e)$ /Spectral Type		$13.5 \pm 1.5$	$14 \pm 1$	$13 \pm 1$
M supergiants	Padova post-MS $V_o$ vs. V-J and $\log(T_e)$		–	$13.5 \pm 1.5$	$13.5 \pm 1.5$
Pre-Main Sequence (FGKM stars)	Baraffe pre-MS V vs. V-I		$14 +2, -1.4$	$14 +2, -1.4$	$14 +2, -1.4$
median average value			$13.75 \pm 1$	$14 \pm 1$	$13.5 \pm 1$
Literature Estimates					
Mayne et al. (2008), Main Sequence Turnoff			13	13	
Slesnick et al. (2002), Main Sequence Turnoff			12.8	12.9	10–20

Note. — For the Baraffe pre-main sequence isochrones we assumed a mixing length parameter of  $L_p = 1.9 H_p$ , which is required to reproduce the observed luminosity and temperature of the Sun.

Table 6. Combined List of  $h$  and  $\chi$  Persei Members

Member ID Number	Photometry Running Number	Spectroscopy Running Number	Membership Type	RA	DEC	Numerical Spectral Type	V	$\sigma(V)$	I	$\sigma(I_c)$
1	3	0	1	34.7691	57.1355	-99.0000	7.1731	0.0000	6.6876	0.0000
2	12	0	1	34.7946	57.1306	-99.0000	7.7561	0.0001	7.2290	0.0001
3	16	60	3	34.6173	57.2084	11.5000	7.7866	0.0001	7.3575	0.0001
4	17	11	3	34.5962	57.0102	10.7000	7.8288	0.0001	7.4510	0.0001
5	21	0	1	34.7917	57.1270	-99.0000	8.1324	0.0001	7.5498	0.0001

Note. — The membership type has the following meaning: 1 = Spectroscopic Members, 2 = Photometric Members, 3 = Spectroscopic and Photometric Members. A zero for either the photometry or spectroscopy running number means that the source lacks either optical photometric or spectroscopic data.

Table 7. Effective Temperatures and Optical/Infrared Colors for Dwarfs

ST	$T_e$	U-B	B-V	V- $I_c$	V-J	V-H	V-K
O5.0	41000	-1.165	-0.310	-0.324	-0.731	-0.864	-0.978
O5.5	39500	-1.160	-0.306	-0.321	-0.727	-0.859	-0.972
O6.0	38250	-1.154	-0.302	-0.320	-0.724	-0.856	-0.968
O6.5	37000	-1.148	-0.298	-0.318	-0.721	-0.852	-0.964
O7.0	36000	-1.143	-0.295	-0.317	-0.719	-0.850	-0.960
O7.5	34750	-1.137	-0.291	-0.315	-0.716	-0.846	-0.956
O8.0	33750	-1.126	-0.287	-0.313	-0.711	-0.840	-0.949
O8.5	32750	-1.114	-0.282	-0.312	-0.706	-0.834	-0.942
O9.0	31750	-1.103	-0.278	-0.310	-0.701	-0.828	-0.935
O9.5	30750	-1.091	-0.273	-0.308	-0.696	-0.822	-0.928
B0.0	30000	-1.078	-0.269	-0.303	-0.686	-0.809	-0.914
B0.2	28100	-1.044	-0.257	-0.291	-0.658	-0.776	-0.876
B0.5	25400	-0.983	-0.239	-0.270	-0.613	-0.722	-0.813
B1.0	24150	-0.954	-0.231	-0.260	-0.591	-0.697	-0.784
B1.5	21800	-0.882	-0.214	-0.238	-0.543	-0.637	-0.715
B2.0	20700	-0.846	-0.206	-0.226	-0.519	-0.608	-0.681
B3.0	18700	-0.771	-0.186	-0.201	-0.466	-0.546	-0.612
B4.0	17200	-0.707	-0.168	-0.181	-0.422	-0.495	-0.554
B5.0	15400	-0.613	-0.146	-0.154	-0.364	-0.427	-0.477
B6.0	14100	-0.526	-0.126	-0.134	-0.316	-0.371	-0.414
B7.0	13000	-0.434	-0.107	-0.115	-0.268	-0.316	-0.353
B8.0	11800	-0.310	-0.081	-0.091	-0.206	-0.242	-0.270
B9.0	10700	-0.179	-0.047	-0.061	-0.134	-0.158	-0.176
A0.0	9886	-0.078	-0.005	-0.027	-0.064	-0.076	-0.082
A1.0	9500	-0.036	0.023	0.000	-0.015	-0.018	-0.020
A2.0	8970	0.017	0.069	0.044	0.061	0.074	0.076
A3.0	8720	0.029	0.098	0.076	0.110	0.133	0.138
A4.0	8460	0.038	0.130	0.113	0.167	0.203	0.209
A5.0	8200	0.028	0.167	0.160	0.238	0.291	0.298
A7.0	7850	0.009	0.219	0.228	0.341	0.422	0.431
A8.0	7580	-0.008	0.259	0.285	0.427	0.531	0.541
A9.0	7390	-0.020	0.289	0.327	0.493	0.617	0.628
F0.0	7200	-0.031	0.318	0.370	0.558	0.702	0.715

Table 7—Continued

ST	$T_e$	U-B	B-V	V-I <sub>c</sub>	V-J	V-H	V-K
F1.0	7050	-0.036	0.347	0.403	0.613	0.774	0.788
F2.0	6890	-0.041	0.377	0.440	0.671	0.851	0.867
F3.0	6740	-0.039	0.409	0.474	0.727	0.927	0.944
F4.0	6590	-0.034	0.443	0.509	0.785	1.004	1.023
F5.0	6440	-0.020	0.480	0.545	0.845	1.084	1.105
F6.0	6360	-0.011	0.501	0.564	0.877	1.128	1.150
F7.0	6280	-0.001	0.522	0.583	0.910	1.171	1.195
F8.0	6200	0.015	0.544	0.603	0.944	1.217	1.242
F9.0	6115	0.039	0.569	0.625	0.981	1.267	1.294
G0.0	6030	0.062	0.594	0.646	1.018	1.318	1.346
G1.0	5945	0.086	0.620	0.667	1.056	1.368	1.398
G2.0	5860	0.113	0.645	0.689	1.094	1.420	1.452
G3.0	5830	0.127	0.655	0.698	1.109	1.440	1.472
G4.0	5800	0.140	0.665	0.706	1.123	1.460	1.493
G5.0	5770	0.153	0.675	0.714	1.138	1.480	1.513
G6.0	5700	0.185	0.697	0.734	1.172	1.526	1.561
G7.0	5630	0.216	0.720	0.753	1.206	1.572	1.609
G8.0	5520	0.276	0.757	0.787	1.266	1.653	1.693
G9.0	5410	0.341	0.793	0.822	1.328	1.739	1.782
K0.0	5250	0.435	0.847	0.874	1.419	1.863	1.911
K1.0	5080	0.548	0.903	0.944	1.537	2.024	2.079
K2.0	4900	0.670	0.962	1.021	1.668	2.201	2.263
K3.0	4730	0.783	1.021	1.105	1.804	2.383	2.453
K4.0	4590	0.873	1.072	1.186	1.932	2.551	2.629
K5.0	4350	0.996	1.158	1.345	2.170	2.839	2.934
K6.0	4205	1.047	1.209	1.457	2.328	3.014	3.121
K7.0	4060	1.066	1.247	1.588	2.505	3.180	3.302
M0.0	3850	1.100	1.300	1.856	2.857	3.470	3.633
M1.0	3720	1.168	1.356	2.000	3.048	3.631	3.824
M2.0	3580	1.295	1.445	2.137	3.238	3.812	4.038
M3.0	3470	1.367	1.497	2.272	3.430	3.991	4.230
M4.0	3370	1.435	1.543	2.412	3.632	4.183	4.430
M5.0	3240	1.471	1.623	2.655	4.014	4.572	4.837

Table 7—Continued

---

---

ST	$T_e$	U-B	B-V	V-I <sub>c</sub>	V-J	V-H	V-K
----	-------	-----	-----	------------------	-----	-----	-----

---

---

Table 8. Effective Temperatures and Optical/Infrared Colors for Giants (III)

ST	$T_e$	U-B	B-V	V- $I_c$	V-J	V-H	V-K
O5.0	41000	-1.162	-0.304	-0.320	-0.724	-0.855	-0.968
O5.5	39500	-1.162	-0.304	-0.320	-0.724	-0.855	-0.968
O6.0	38250	-1.159	-0.300	-0.314	-0.715	-0.844	-0.956
O6.5	37000	-1.155	-0.296	-0.310	-0.709	-0.837	-0.948
O7.0	36000	-1.149	-0.293	-0.310	-0.709	-0.837	-0.948
O7.5	34750	-1.141	-0.290	-0.311	-0.709	-0.838	-0.948
O8.0	33750	-1.134	-0.287	-0.311	-0.709	-0.838	-0.948
O8.5	32750	-1.126	-0.284	-0.309	-0.706	-0.834	-0.943
O9.0	31750	-1.117	-0.279	-0.306	-0.700	-0.827	-0.935
O9.5	30750	-1.114	-0.272	-0.299	-0.686	-0.811	-0.918
B0.0	30000	-1.106	-0.268	-0.295	-0.679	-0.802	-0.907
B1.0	24500	-1.043	-0.232	-0.247	-0.589	-0.695	-0.785
B2.0	21050	-0.969	-0.203	-0.208	-0.515	-0.605	-0.684
B3.0	16850	-0.821	-0.167	-0.155	-0.404	-0.472	-0.533
B5.0	14800	-0.715	-0.142	-0.116	-0.325	-0.378	-0.429
B7.0	13700	-0.672	-0.117	-0.085	-0.271	-0.313	-0.358
B8.0	13150	-0.602	-0.119	-0.082	-0.252	-0.292	-0.333
B9.0	11731	-0.488	-0.092	-0.044	-0.175	-0.199	-0.233
A0.0	10000	-0.273	-0.054	0.005	-0.054	-0.057	-0.077
A2.0	9000	-0.142	-0.008	0.058	0.054	0.072	0.063
A3.0	8500	-0.064	0.024	0.091	0.122	0.154	0.152
A5.0	8000	0.030	0.061	0.128	0.202	0.251	0.257
A7.0	7750	0.080	0.091	0.156	0.256	0.315	0.327
A9.0	7450	0.143	0.130	0.198	0.332	0.407	0.426
F0.0	7350	0.165	0.142	0.215	0.363	0.445	0.466
F1.0	7200	0.199	0.162	0.241	0.409	0.502	0.526
F2.0	7050	0.233	0.190	0.271	0.461	0.566	0.594
F3.0	6850	0.281	0.263	0.331	0.554	0.682	0.714
F5.0	6630	0.333	0.344	0.396	0.656	0.810	0.847
F7.0	6330	0.404	0.455	0.486	0.795	0.984	1.028
F8.0	6220	0.430	0.495	0.519	0.846	1.048	1.094
F9.0	6020	0.478	0.569	0.578	0.939	1.164	1.215
G0.0	5800	0.563	0.668	0.652	1.056	1.315	1.369

Table 8—Continued

ST	$T_e$	U-B	B-V	V-I <sub>c</sub>	V-J	V-H	V-K
G1.0	5700	0.624	0.724	0.691	1.119	1.398	1.454
G2.0	5500	0.745	0.837	0.770	1.246	1.564	1.623
G5.0	5200	0.926	1.006	0.887	1.437	1.814	1.877
G8.0	4950	0.843	1.019	0.996	1.623	2.107	2.171
K0.0	4810	0.747	0.999	1.059	1.731	2.285	2.350
K1.0	4585	0.875	1.075	1.189	1.936	2.556	2.633
K2.0	4390	0.982	1.145	1.315	2.126	2.790	2.881
K3.0	4225	1.040	1.202	1.443	2.307	2.989	3.095
K5.0	3955	1.076	1.271	1.706	2.659	3.310	3.449
M0.0	3845	1.102	1.302	1.863	2.866	3.477	3.642
M1.0	3750	1.145	1.338	1.976	3.016	3.601	3.788
M2.0	3655	1.224	1.396	2.060	3.131	3.710	3.918
M3.0	3560	1.314	1.458	2.159	3.267	3.839	4.070
M4.0	3460	1.373	1.502	2.285	3.449	4.010	4.249
M5.0	3355	1.445	1.549	2.433	3.662	4.212	4.460

Table 9. Effective Temperatures and Optical/Infrared Colors for Supergiants (I)

ST	$T_e$	U-B	B-V	V-I <sub>c</sub>	V-J	V-H	V-K
B0.0	30000	-1.078	-0.269	-0.303	-0.686	-0.809	-0.914
B0.2	26300	-1.014	-0.247	-0.275	-0.628	-0.741	-0.835
B0.5	23100	-0.988	-0.226	-0.240	-0.568	-0.668	-0.754
B1.0	20260	-0.907	-0.208	-0.212	-0.508	-0.598	-0.673
B1.5	19400	-0.881	-0.200	-0.201	-0.485	-0.570	-0.643
B2.0	18000	-0.837	-0.185	-0.180	-0.444	-0.520	-0.585
B5.0	13600	-0.628	-0.127	-0.094	-0.276	-0.319	-0.363
B8.0	11000	-0.423	-0.073	-0.020	-0.125	-0.141	-0.168
A0.0	9900	-0.256	-0.052	0.007	-0.046	-0.049	-0.067
A2.0	9000	-0.118	-0.017	0.048	0.049	0.066	0.057
A3.0	8400	-0.005	0.013	0.085	0.134	0.168	0.168
A5.0	8100	0.049	0.036	0.109	0.184	0.228	0.235
A7.0	7800	0.117	0.063	0.142	0.250	0.308	0.320
F0.0	7200	0.223	0.160	0.249	0.430	0.528	0.552
F1.0	7050	0.247	0.195	0.283	0.484	0.596	0.623
F3.0	6770	0.285	0.272	0.354	0.594	0.733	0.765
F5.0	6570	0.302	0.349	0.417	0.689	0.855	0.890
F7.0	6280	0.345	0.459	0.505	0.827	1.033	1.073
F8.0	6180	0.360	0.498	0.536	0.874	1.095	1.136
F9.0	5980	0.422	0.577	0.596	0.967	1.212	1.259
G0.0	5590	0.542	0.757	0.735	1.191	1.513	1.565
G1.0	5490	0.592	0.807	0.771	1.250	1.593	1.645
G2.0	5250	0.734	0.932	0.858	1.398	1.791	1.849
G5.0	5000	0.949	1.080	0.953	1.565	2.012	2.076
G8.0	4700	1.198	1.232	1.066	1.784	2.314	2.390
K0.0	4500	1.426	1.336	1.158	1.958	2.549	2.640
K1.0	4200	1.816	1.493	1.332	2.262	2.956	3.072
K2.0	4100	1.949	1.549	1.414	2.392	3.125	3.252
K7.0	3840	2.180	1.686	1.695	2.829	3.664	3.821
M0.0	3790	2.225	1.719	1.758	2.927	3.781	3.945
M1.0	3745	2.182	1.726	1.838	3.052	3.923	4.092
M2.0	3660	1.858	1.686	2.082	3.436	4.341	4.513
M3.0	3605	1.616	1.651	2.245	3.690	4.616	4.789

Table 9—Continued

ST	$T_e$	U-B	B-V	V-I <sub>c</sub>	V-J	V-H	V-K
M5.0	3450	1.167	1.584	2.716	4.472	5.438	5.625

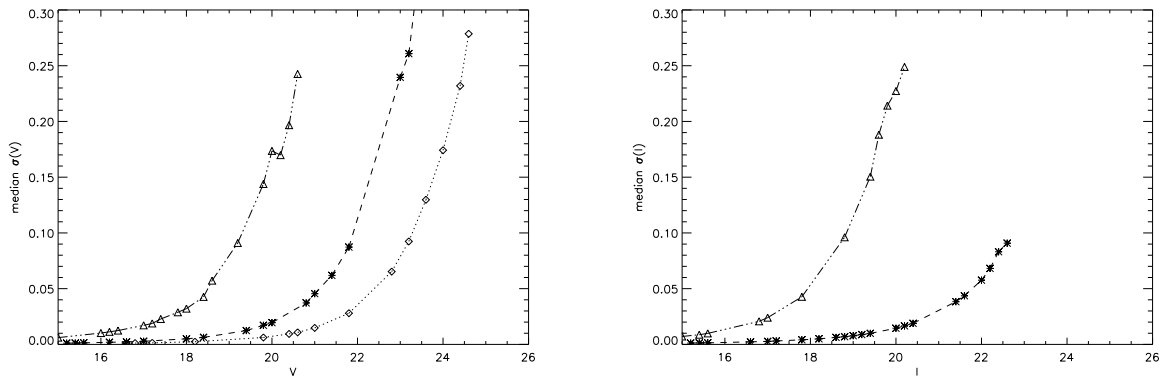


Fig. 1.— Median V and I magnitude uncertainties as a function of V and I. The median uncertainties were computed in bins of 0.2 magnitudes.

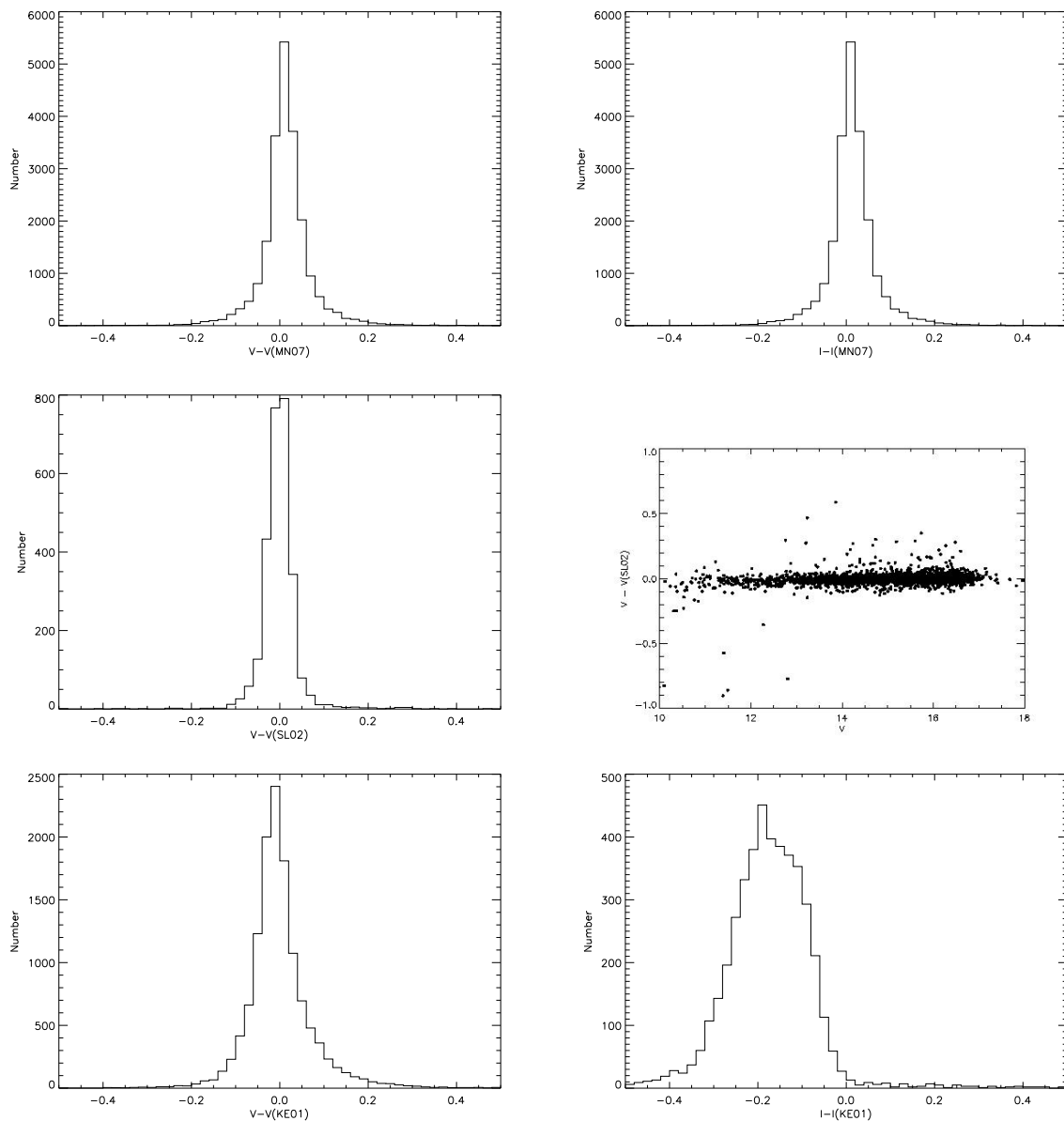


Fig. 2.— Differences between our optical photometry and previous work by Mayne et al. (2007), Slesnick et al. (2002), and Keller et al. (2001). (Top) Histogram plots of the magnitude differences in V and I band between our photometry and that from Mayne et al. (2007). (Middle Row) Histogram plot (left) comparing our V band photometry with Slesnick et al. (2002) and the photometric difference plotted against our V magnitudes (right). (Bottom) Histogram plots comparing our V and I photometry with that from Keller et al. (2001).

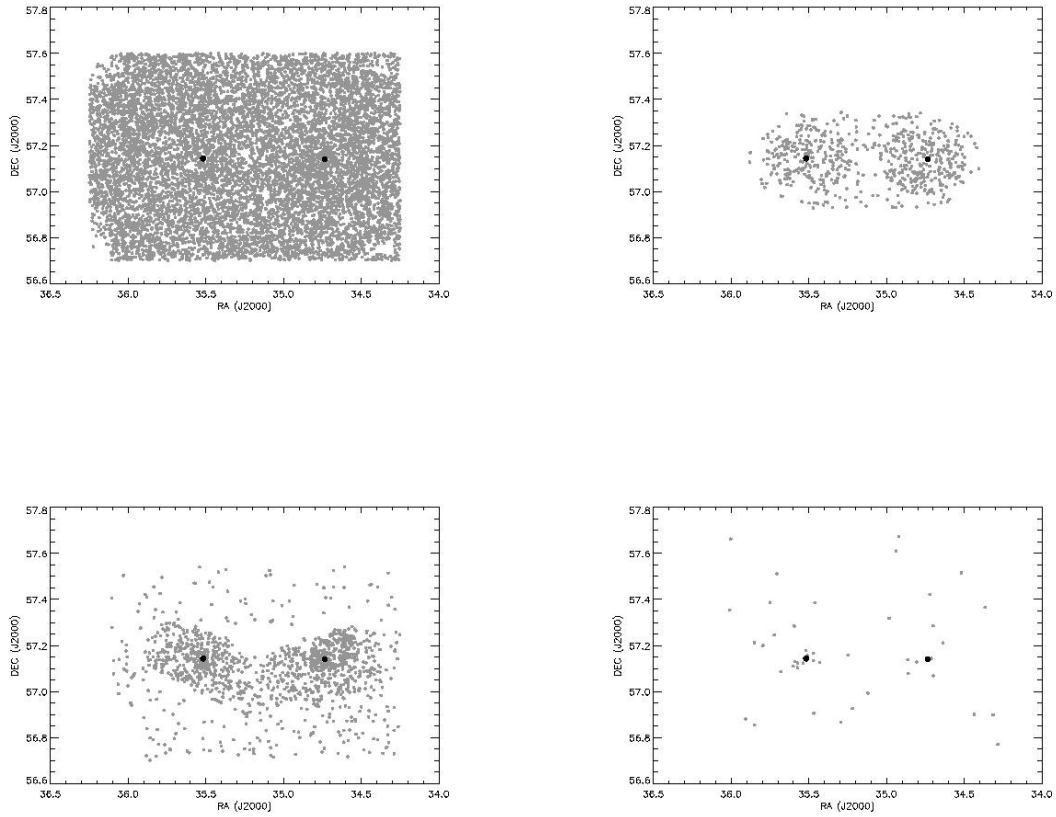


Fig. 3.— Coverage map of spectroscopy surveys from Hectospec (top-left), FAST (bottom-left), Hydra (top-right), and Slesnick et al. (2002) (bottom-right). The centers of h Persei and  $\chi$  Persei are shown as the right and left dots, respectively

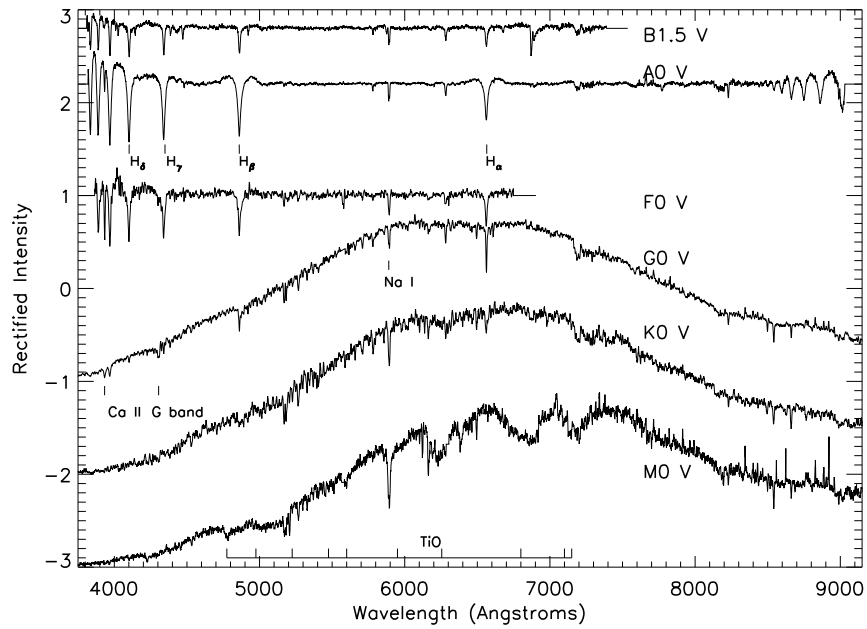


Fig. 4.— Spectral type sequence from B1.5 V (top) to M0 (bottom) showing the change in line strengths with spectral type/effective temperature. The IDs of these stars in Table 3 are (from top to bottom) ID-82, ID-912, ID-2056, ID-4905, ID-6457, and ID-7180. We follow the convention of Gray and Corbally (2009) by displaying the continuum flux of BAF stars as a constant, while displaying the normalized spectra of GKM stars.

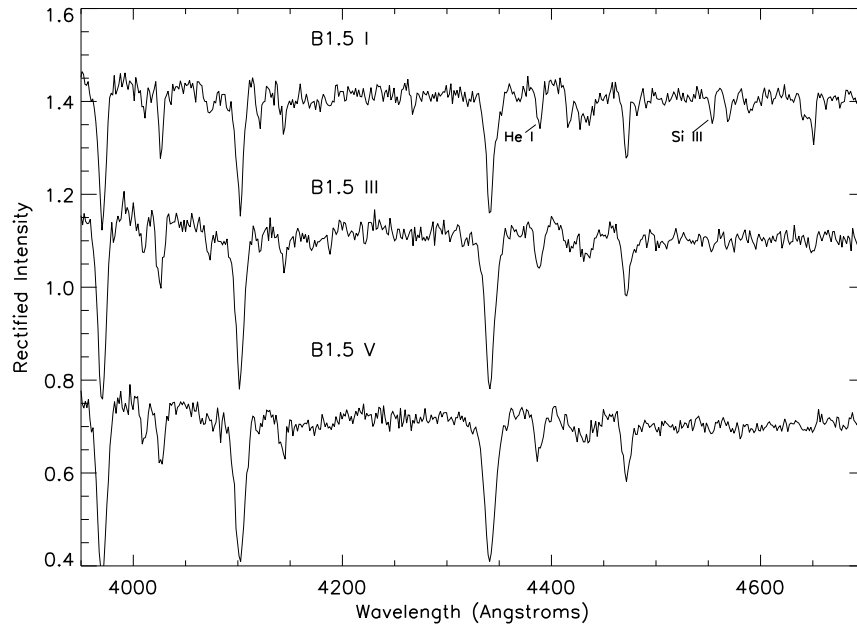


Fig. 5.— Luminosity sequence of B1.5 stars – class I supergiant (top), class III giant (middle), and class V dwarf (bottom) – showing the normalized continuum intensity vs. wavelength. The B1.5 I star is ID-61 in Table 3, the B1.5 III star is ID-67 in Table 3, and the B1.5 V star is ID-82 in Table 3. The spectra exhibit a clear evolution in their Si4552 to He4387 line ratios: Si4552 is strongest for the supergiant, weak but detectable for the giant, and almost nonexistent for the dwarf.

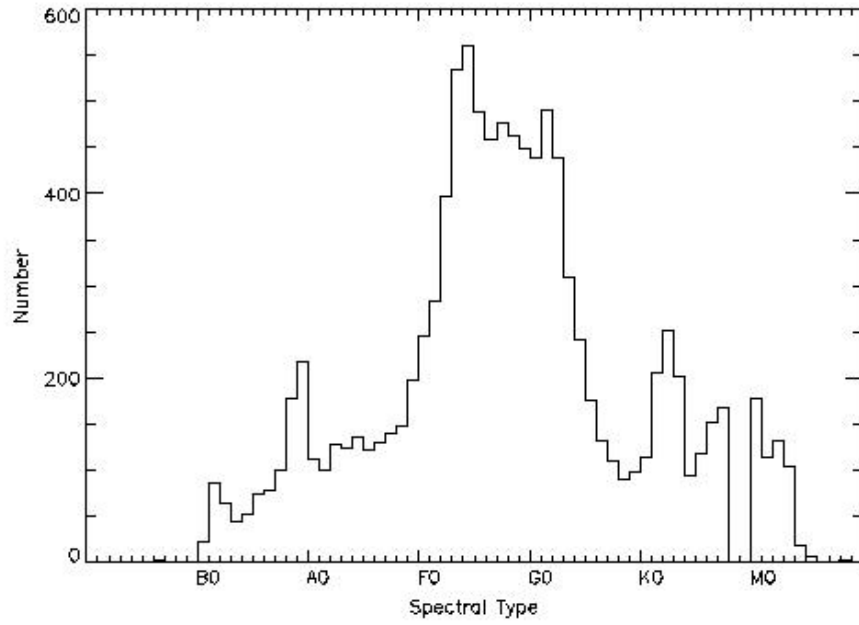


Fig. 6.— Spectral type distribution of sources. The rise in number from B stars to F stars is likely a consequence of the cluster mass function. The drop in the number of G5–M0 stars is due to survey incompleteness.

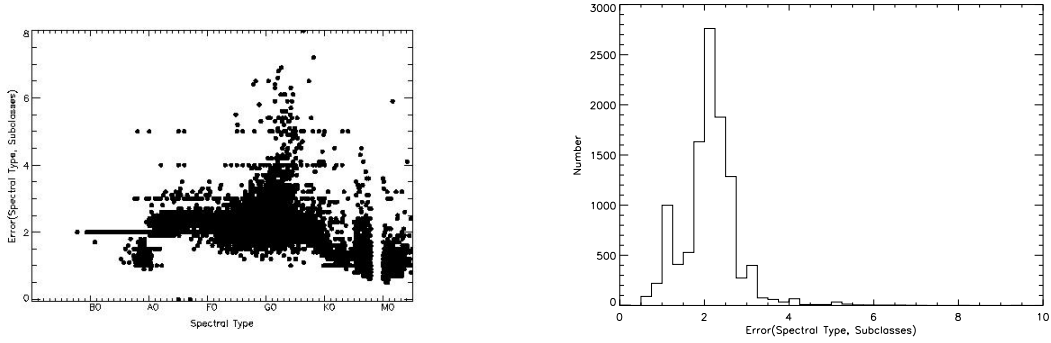


Fig. 7.— Uncertainty in spectral type vs. spectral type (left) and histogram of uncertainties in spectral types. The uncertainties in spectral types are given in subclasses. The gap between K7 and M0 occurs because there are no K8 or K9 stars in the standard MK spectral classification system.

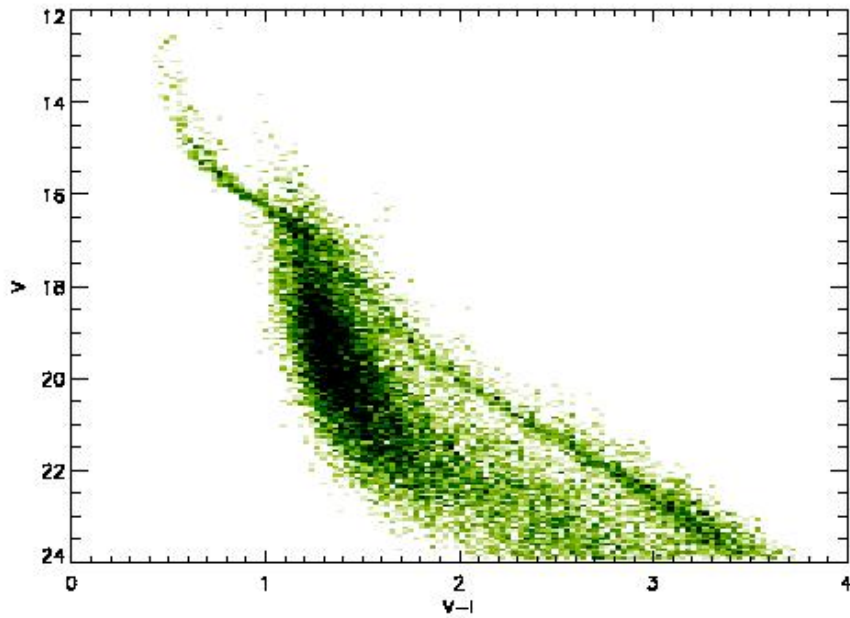


Fig. 8.—  $V/V-I$  color-magnitude Hess diagram for all stars detected with our photometry. The positions of  $h$  and  $\chi$  Persei stars are clearly identifiable as a narrow locus stretching from the top-left to lower-right region of the plot. With the possible exception of a region with  $V-I \sim 1.1-1.6$ , the locus of cluster stars is easily distinguishable from the background field star population.

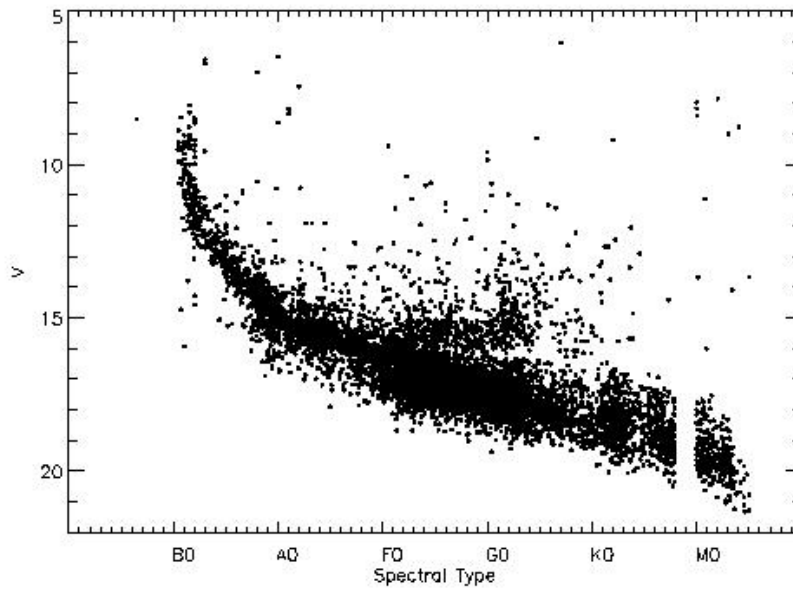
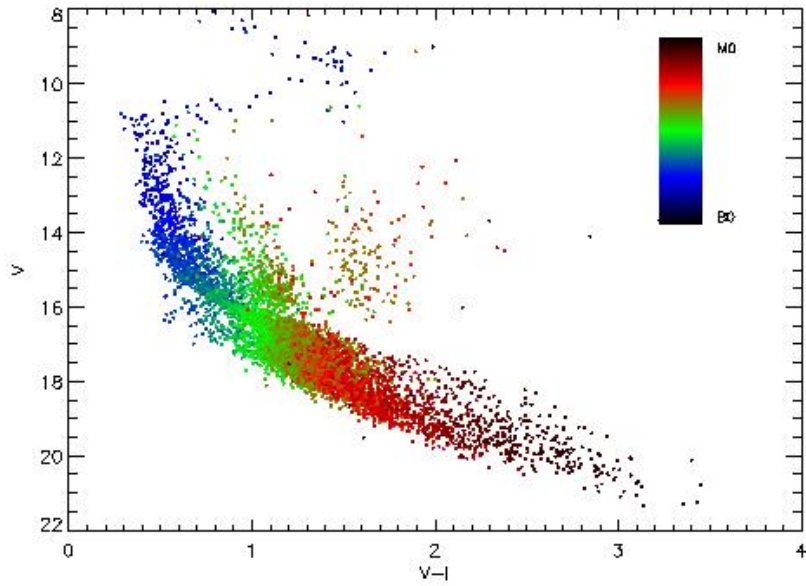


Fig. 9.— (Top)  $V/V-I$  color-magnitude diagrams of stars with optical spectra color-coded by spectral type. (Bottom) Observational Hertzsprung-Russell diagram for the same population.

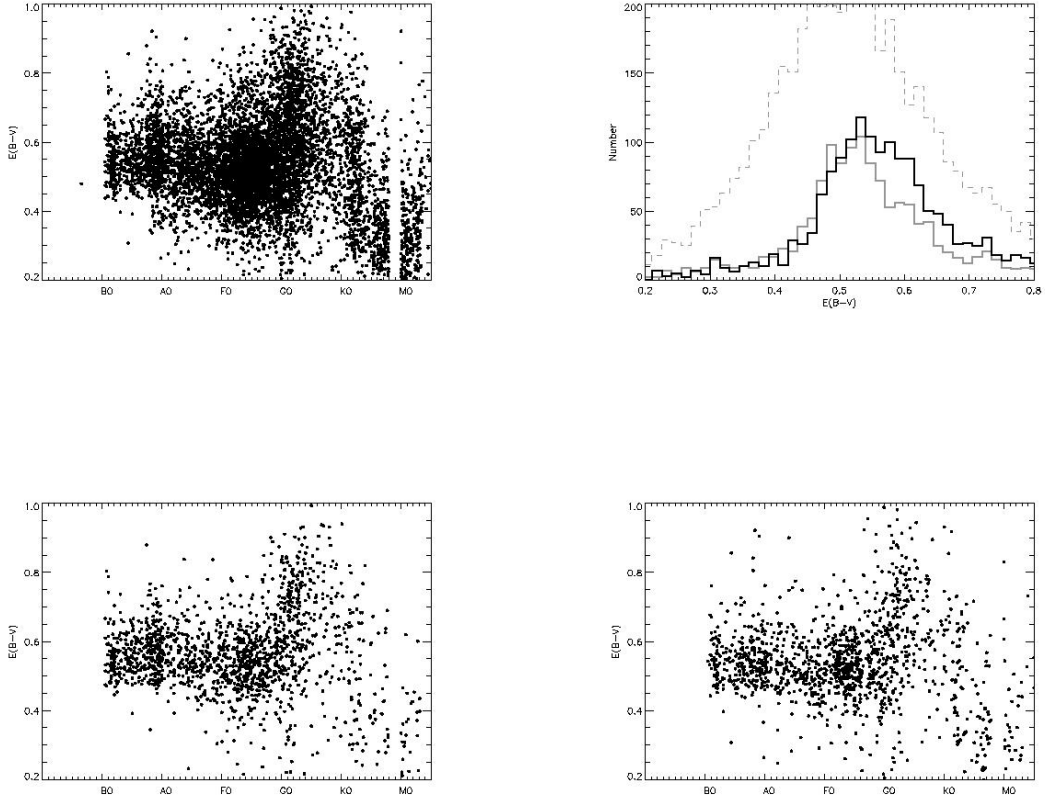


Fig. 10.— Reddening distribution for spectroscopically observed stars. (Top-left) The distribution of  $E(B-V)$  vs. spectral type for all stars on the field. (Top-right) Histogram plot of  $E(B-V)$  for stars in the h Per core-dominated region ( $< 10'$ ; thick black line),  $\chi$  Per core-dominated region ( $< 10'$ ; thick grey line), and low-density halo region (dashed grey line). (Bottom panels) The reddening distributions for the h Per core region (left) and  $\chi$  Per core region (right).

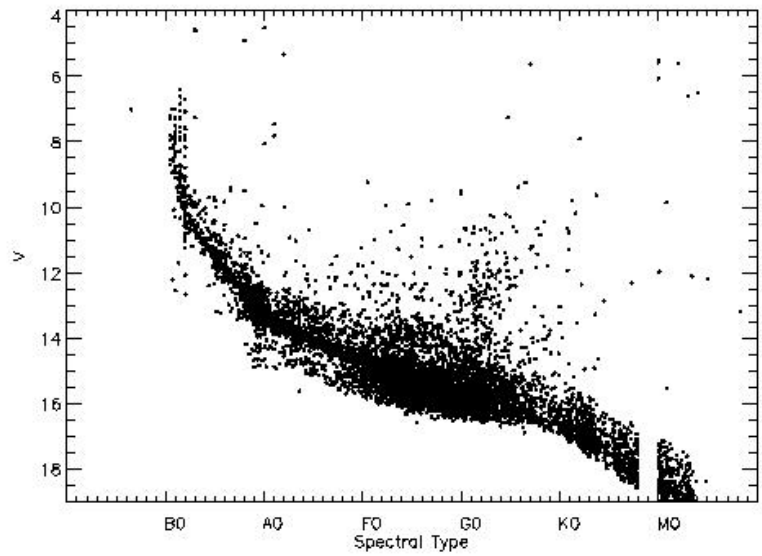
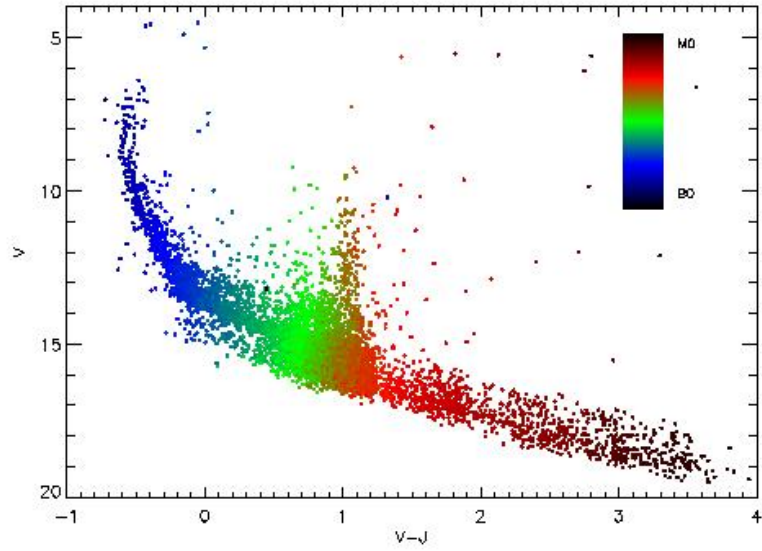


Fig. 11.— The dereddening  $V/V-J$  color-magnitude diagram (top) and the dereddened  $V$  vs. spectral type HR diagram (bottom).

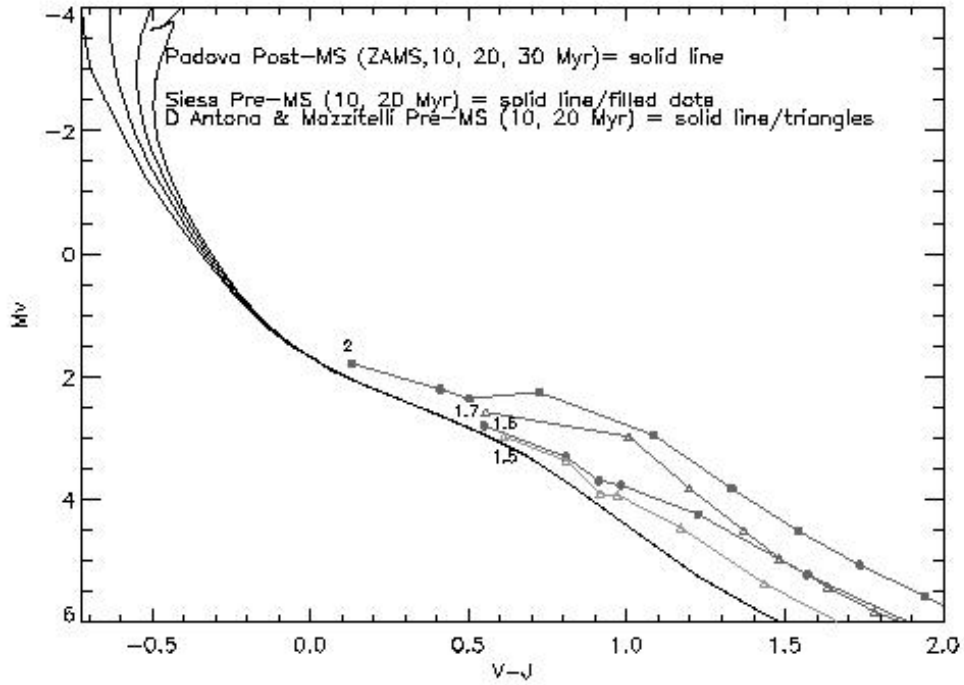


Fig. 12.— Comparing isochrones from Marigo et al. (2008), D’Antona and Mazzitelli (1994), and Siess et al. (2000) to illustrate the age independence of the luminosity of late B to early A stars. The numbers identify the most massive star yet to reach the main sequence for each pre-main sequence isochrone.

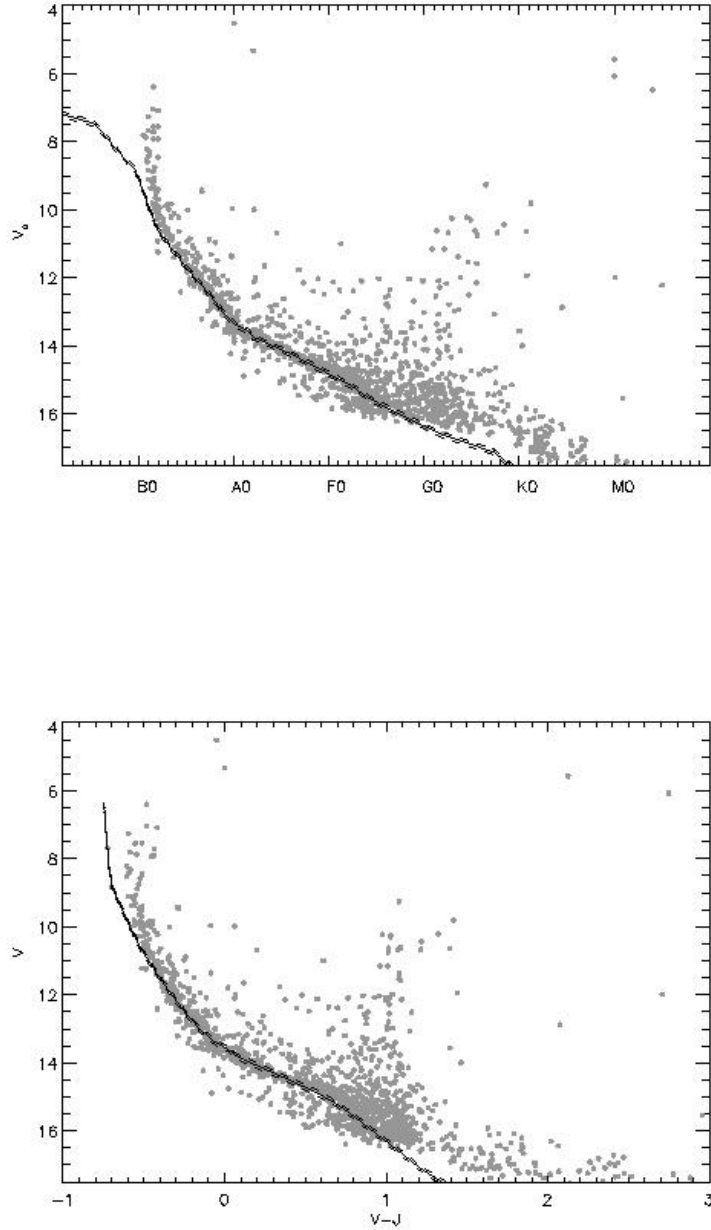


Fig. 13.— (Top)  $V$  vs. spectral type plot of stars within  $10'$  of the  $\chi$  Persei center. (Bottom)  $V$  vs.  $V-J$  color-magnitude diagram of the same stars. The solid line in both plots corresponds to the zero-age main sequence with a distance modulus of  $dM = 11.85$ . Dashed lines show the zero-age main sequence for  $dM = 11.77$  and  $11.93$ . Main sequence fitting is performed between B5 and A5 spectral types and  $V-J = -0.3-0.5$ .

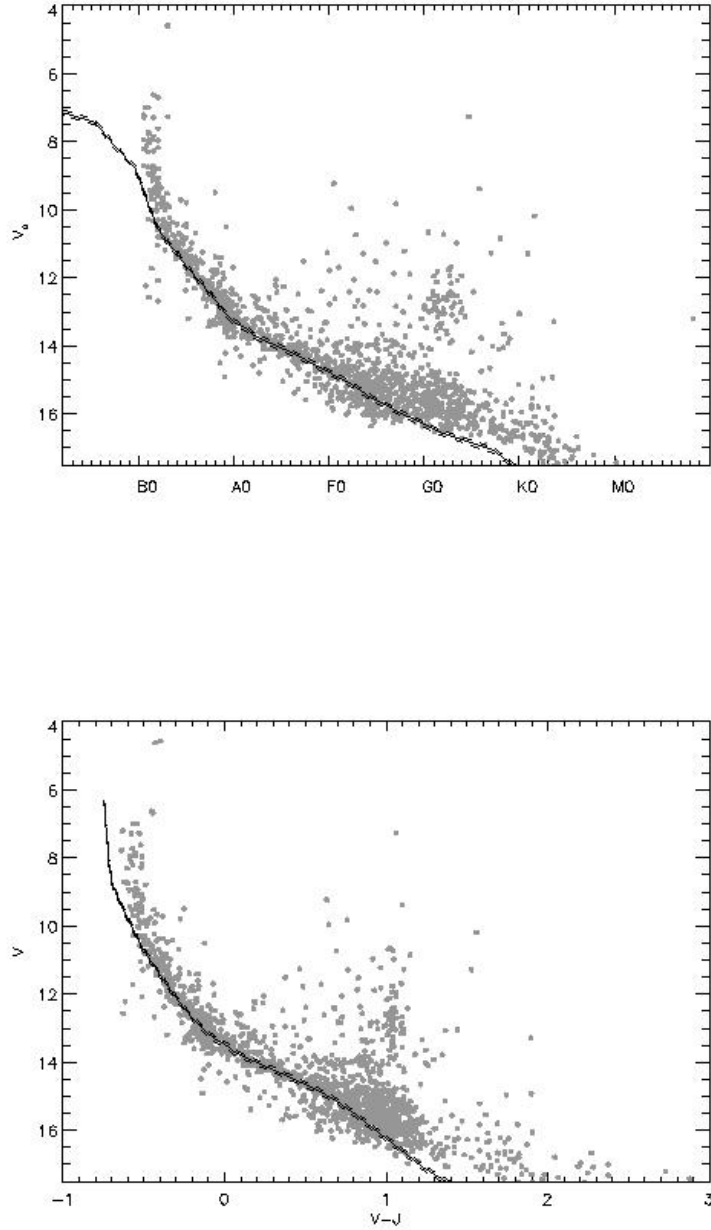


Fig. 14.— Same as previous plot except for stars within  $10'$  of the  $\eta$  Persei center with a distance modulus of  $dM = 11.8$  (thick line) and extrema of  $dM = 11.72$  and  $11.88$ .

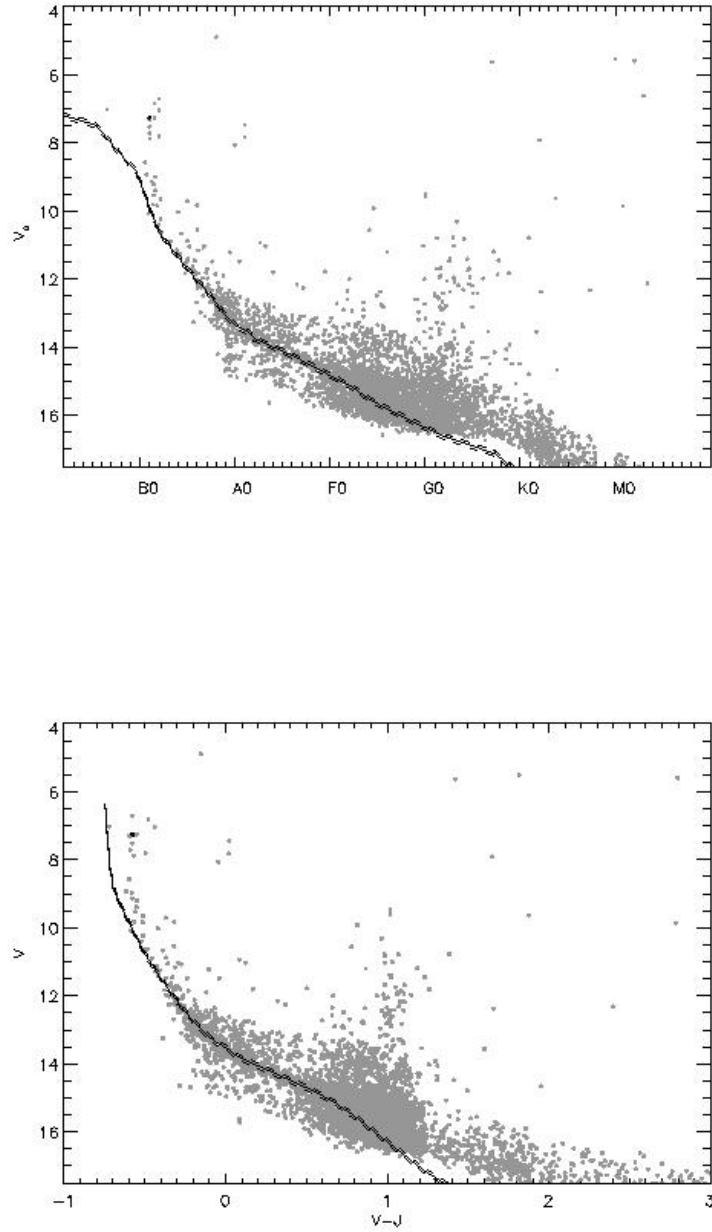


Fig. 15.— Same as previous plot except for stars beyond 10' from the  $\eta$  and  $\chi$  Persei centers, the halo population, with a distance modulus of  $dM = 11.85$  (thick line) and extrema of  $dM = 11.77$  and  $11.93$ .

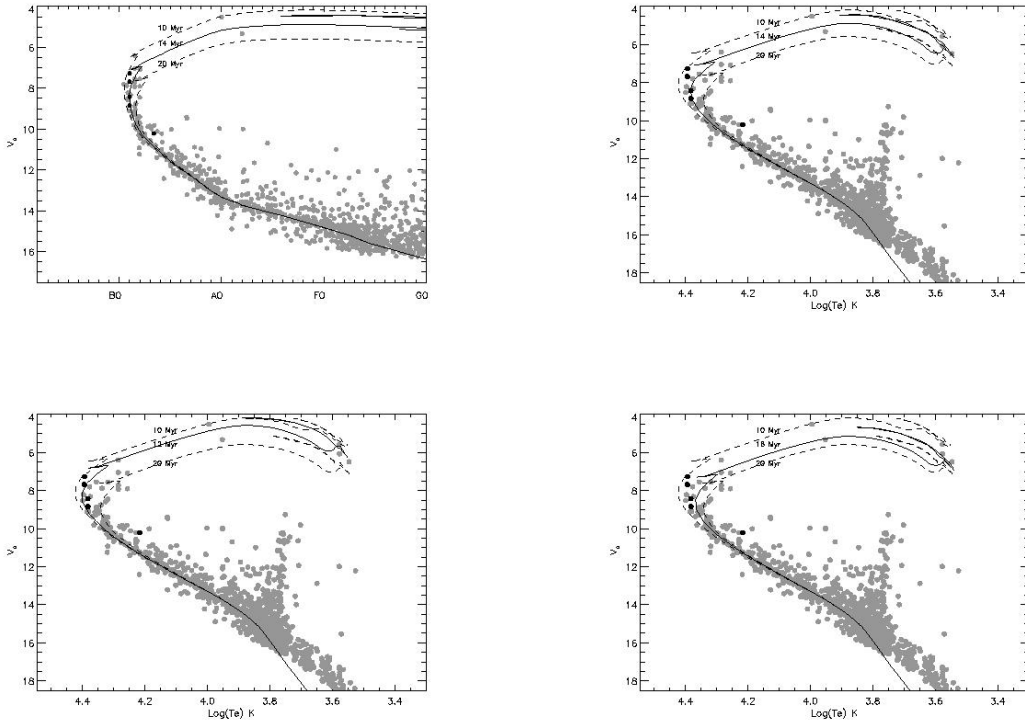


Fig. 16.— (Top Panels) Dereddened  $V$  vs. spectral type (left) and dereddened  $V$  vs.  $\log(T_e)$  (right) HR diagrams showing the main sequence turnoff for  $\chi$  Persei. Black dots indicate the positions of Be stars. Overplotted are the Padova post-main sequence isochrones corresponding to ages of 10 and 20 Myr (dashed lines) and 14 Myr (solid line). (Bottom Panels) The dereddened  $V$  vs.  $\log(T_e)$  diagrams replacing the 14 Myr isochrone with 12 Myr and 16 Myr isochrones.

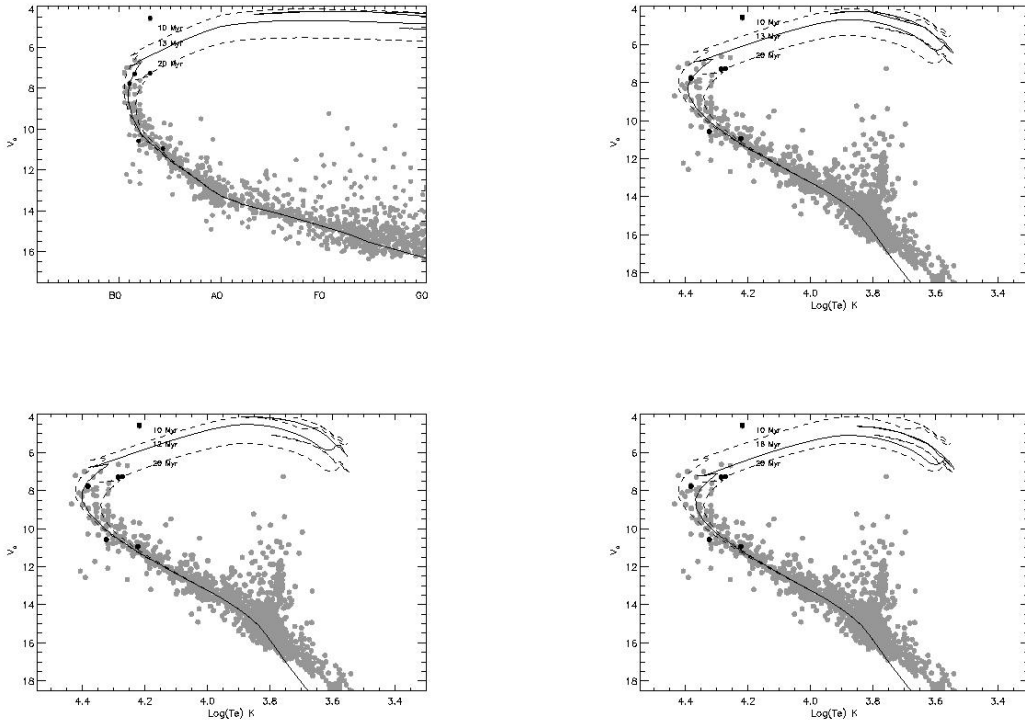


Fig. 17.— (Top Panels) Dereddened  $V$  vs. spectral type (left) and dereddened  $V$  vs.  $\log(T_e)$  (right) HR diagrams showing the main sequence turnoff for h Persei. Black dots indicate the positions of Be stars. Overplotted are the Padova post-main sequence isochrones corresponding to ages of 10 and 20 Myr (dashed lines) and 13 Myr (solid line). (Bottom Panels) The dereddened  $V$  vs.  $\log(T_e)$  diagrams replacing the 13 Myr isochrone with 12 Myr and 16 Myr isochrones.

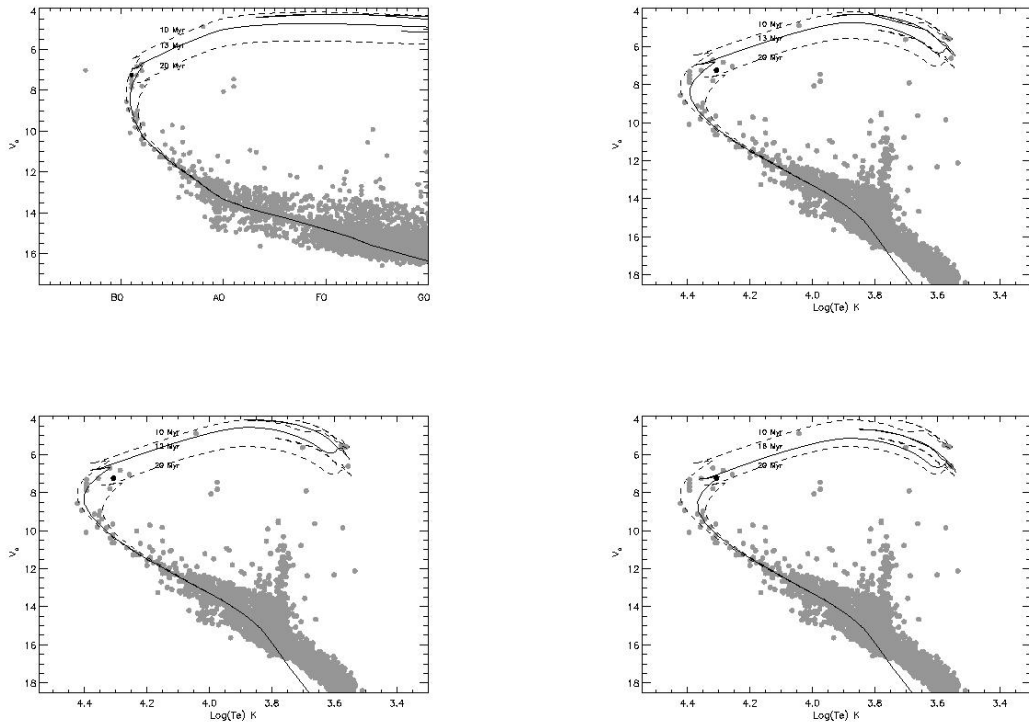


Fig. 18.— Same as Figure 17 except for stars in the low-density regions surrounding the h Persei and  $\chi$  Persei cores ( $> 10'$  away from the cluster centers).

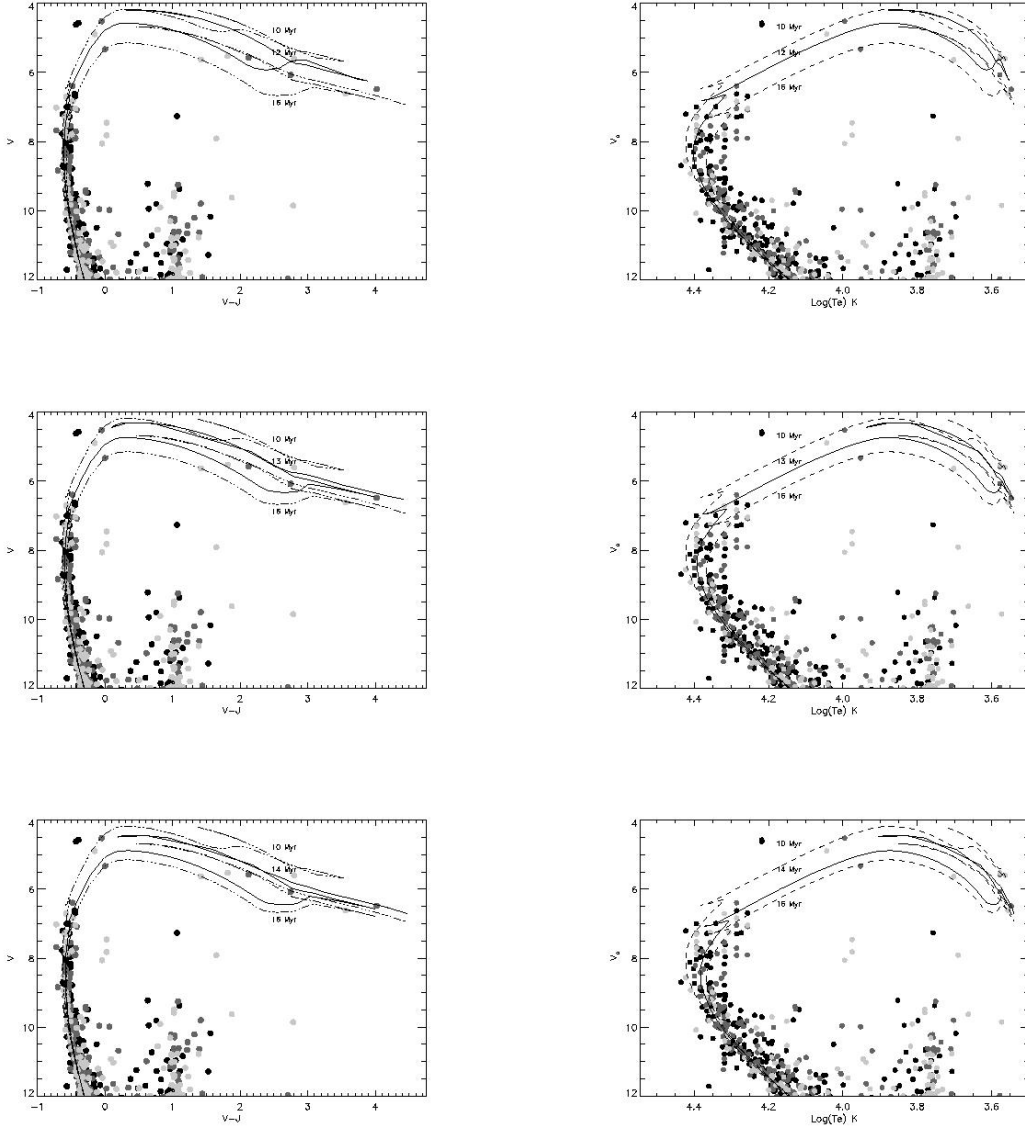


Fig. 19.— (Left Panels) dereddened  $V$  vs.  $V-J$  and (Right Panels) dereddened  $V$  vs.  $\log(T_e)$  comparing the Padova isochrones of 12 Myr, 13 Myr, and 14 Myr (organized from top to bottom; solid lines in all cases) to the positions of red supergiants. Black dots indicate stars in the h Persei core, grey dots indicate stars in the  $\chi$  Persei core, and light-grey indicates halo region stars.

## A. Effective Temperature Scale for Dwarfs, Giants, and Supergiants

Here we describe our adopted effective temperature scales for dwarfs (luminosity class V), giants (class III), and supergiants (class I). As a starting point, we considered the effective temperature scales from Gray and Corbally (2009) because it is the most recent and comprehensive; Bessell et al. (1998) and Kenyon and Hartmann (1995)<sup>9</sup> because they are the most widely cited primary references from the past 15 years; Humphreys and McElroy (1984) because it is also well cited and provides the best sampling with spectral type based on a large dataset; and De Jager and Nieuwenhuijzen (1987) because it also is a well-cited paper with good sampling that treats the spectral type as a continuous, not discrete, variable.

Secondary references provided independent checks on and modifications to these primary references. These references derive temperature scales in one of two ways: 1) estimating temperatures using non-LTE atmospheric models (Massey et al. 2005; Levesque et al. 2005) and 2) deriving a purely empirical scale based on fitting stellar atmosphere models to synthetic MK spectral standards (Gray and Corbally 1994). Where the primary sources disagree, we analyze a range of computed scales from the above secondary sources as well as classic references such as Schmidt-Kaler (1982) and Bohm-Vitense (1981) to arrive at a final calibrated scale.

### A.1. Dwarfs

For O5–B0 dwarfs, sophisticated non-LTE calculations are crucial to accurately determining  $T_e$ . Therefore, we adopt the empirically-derived scale from Massey et al. (2005) for these stars. The Massey et al. (2005) scale departs from the Gray and Corbally (2009) scale by less than  $\approx 500$  K for nearly all subtypes. Because O5–B0 stars have temperatures  $\gtrsim 30,000$  K, these differences are inconsequential ( $\lesssim 1.7\%$ ).

For B0.2–A0 stars, there is generally good agreement between Gray and Corbally (2009), Bessell et al. (1998), Humphreys and McElroy (1984) and De Jager and Nieuwenhuijzen (1987) for most subclasses. However, there are serious disagreements between these authors for B1–B3 stars; these stars are crucial for accurately assessing cluster properties (e.g. the main sequence turnoff) because they cover a wide range in V band magnitudes for our sample. In particular, the Bessell et al. (1998) scale is up to 2500 K hotter than the others. The origin

---

<sup>9</sup>Though Kenyon and Hartmann (1995) identify Bessell and Brett (1988) as a primary source for dwarf stars temperatures and colors, it appears that their  $T_e$  scale is drawn from Bessell (1979) instead, which in turn adopts the interferometrically-determined scale from Code et al. (1976).

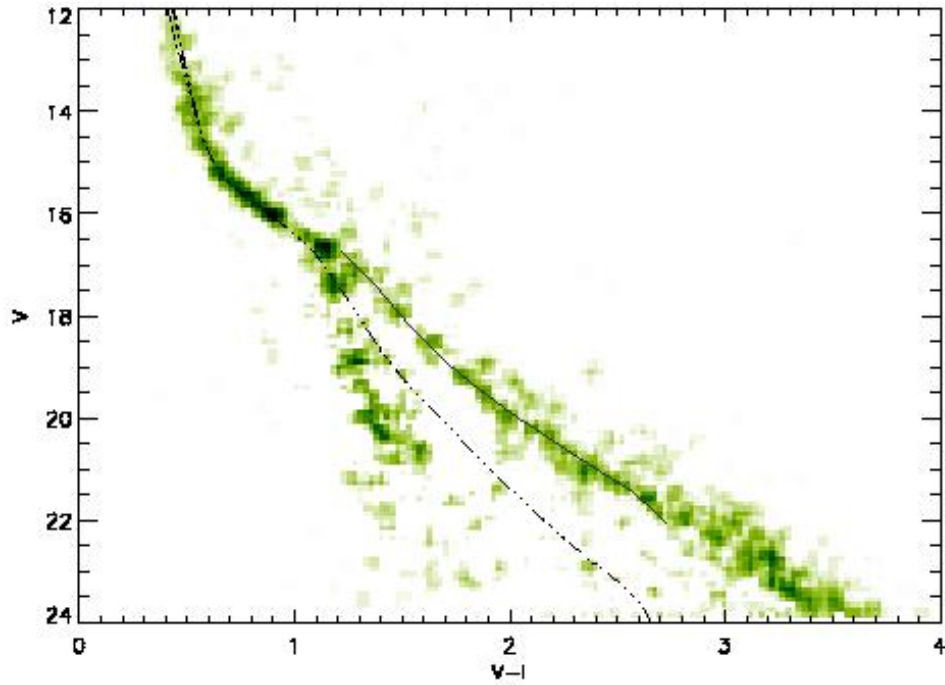


Fig. 20.— The pre-main sequence age determination for  $\chi$  Persei from the  $V/V-I$  color-magnitude diagram. The data for stars within  $7'$  of the cluster center are represented by a box-car smoothed Hess diagram with the background field star population statistically subtracted (green regions). Darker regions correspond to higher density. The black line (dash-three dots) represents (from left to right) the zero-age main sequence and the zero-age main sequence + 14 Myr post-main sequence Padova isochrone. The solid dark grey line represents the 14 Myr pre-main sequence isochrone from Baraffe et al. (1998).

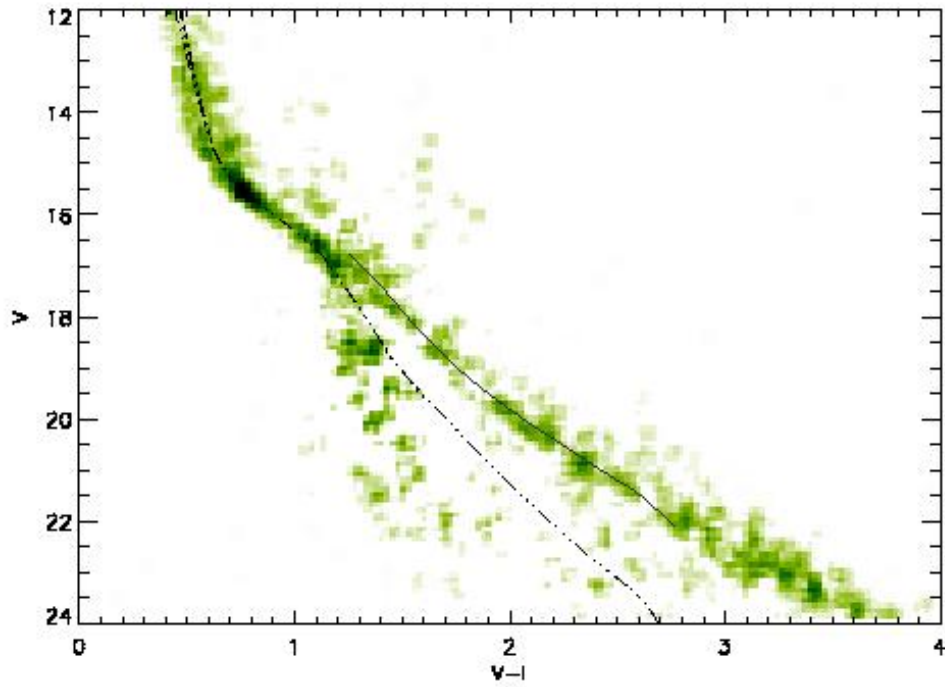


Fig. 21.— Same as previous figure except for stars within 7' of the h Persei center.

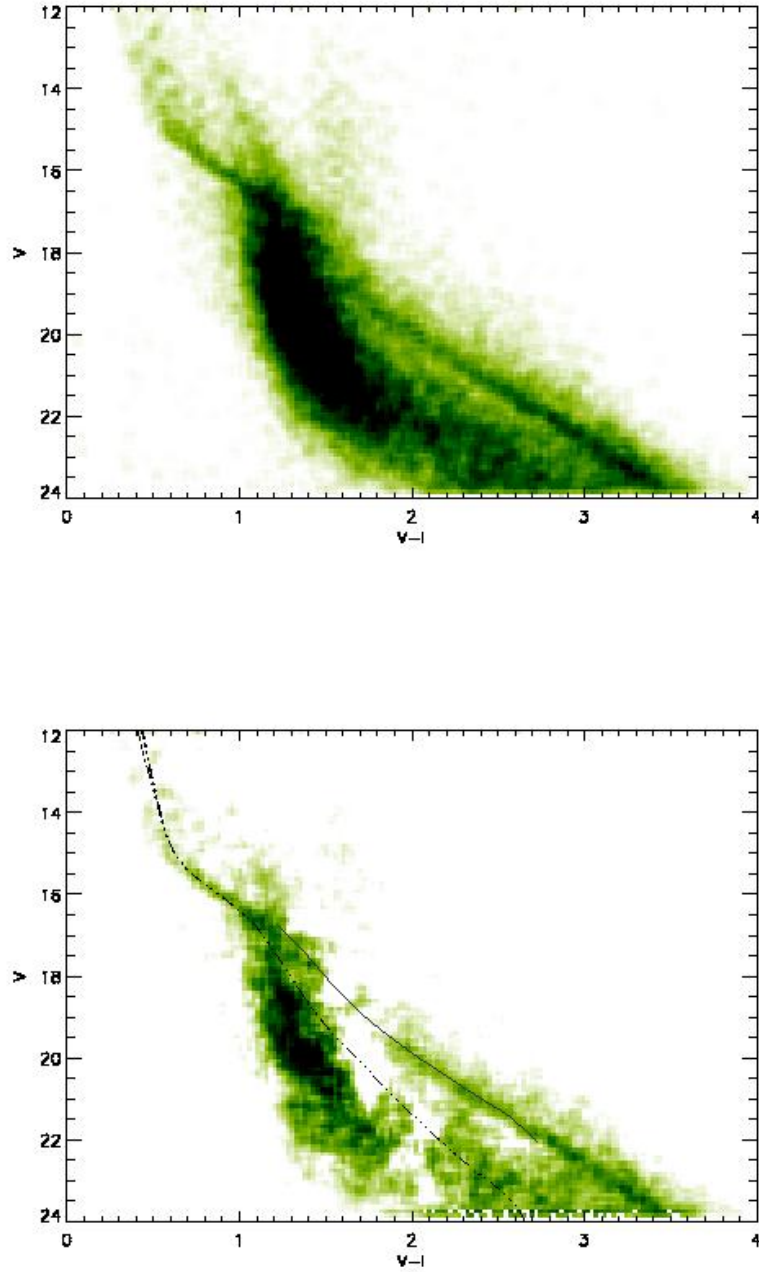


Fig. 22.— (Top panel) The raw box-car smoothed Hess diagram for stars between 10' and 20' from the cluster centers. (Bottom panel) Same as previous figure except for stars between 10' and 20' from the cluster centers.

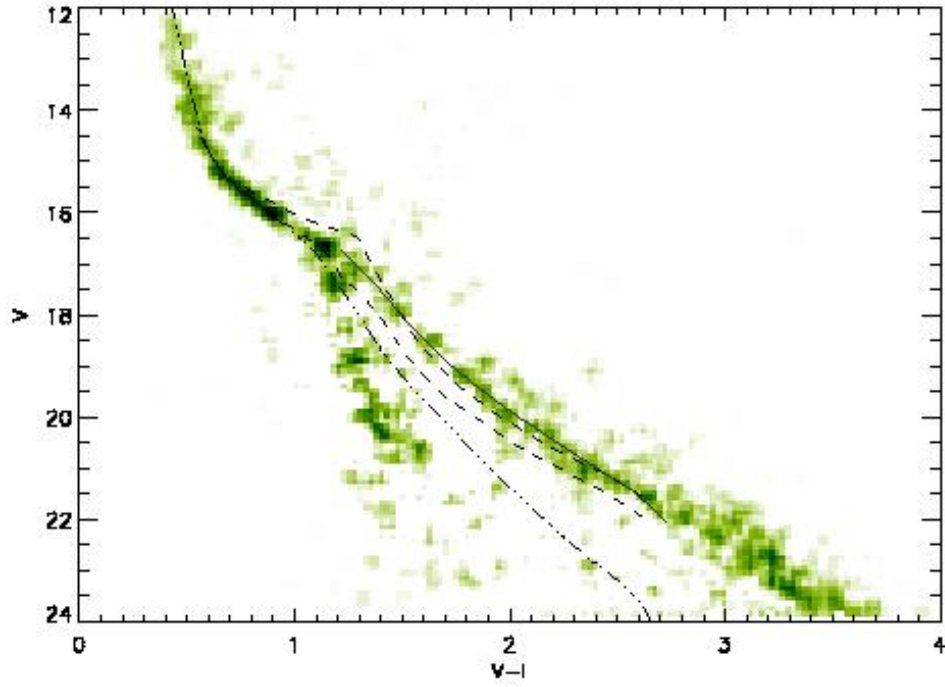


Fig. 23.— Same as previous figures except with the D’Antona and Mazzitelli (1994, 1997) isochrones for 10 Myr and 20 Myr overplotted. The D’Antona and Mazzitelli (1994, 1997) tracks clearly fail to reproduce the observed shape of the pre-main sequence locus.

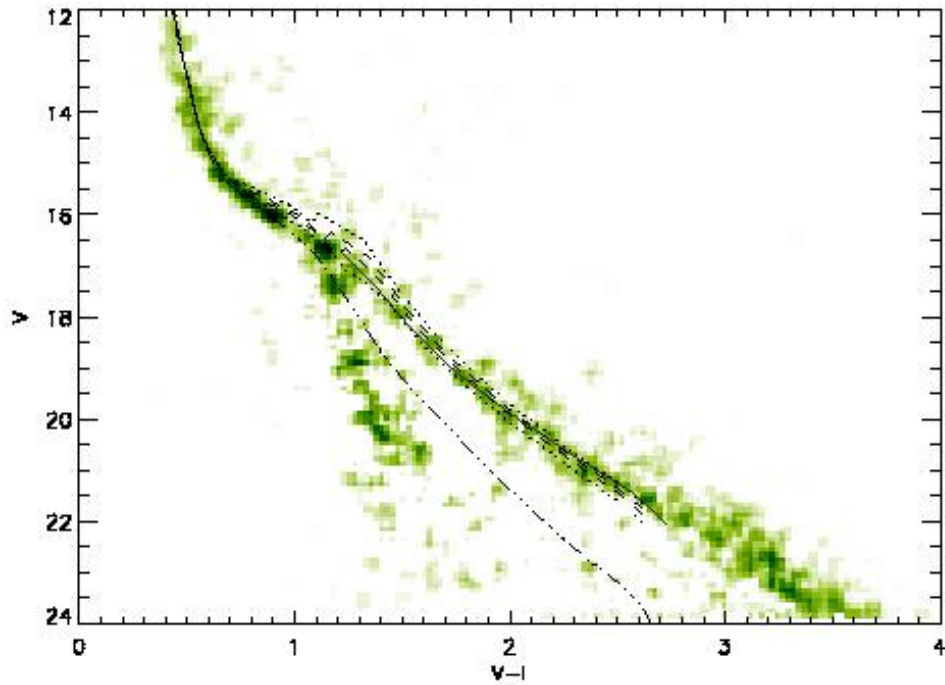


Fig. 24.— Same as previous figure except with the Siess et al. (2000) isochrones for 12 Myr (top dotted line), 14 Myr (top dashed line), 16 Myr (bottom dashed line), and 20 Myr (bottom dotted line) overplotted. The Siess et al. (2000) do better than D’Antona and Mazzitelli (1997) in reproducing the observed shape of the cluster locus but generally overestimate the luminosity of  $\sim 1.5\text{--}2 M_{\odot}$  stars ( $V\text{--}I \sim 1\text{--}1.5$ ).

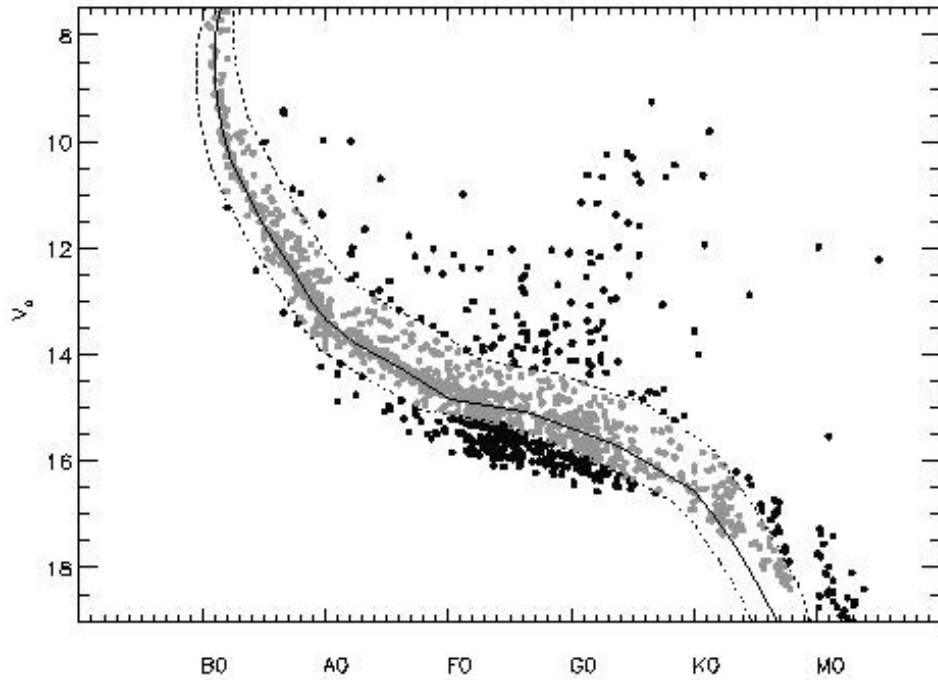


Fig. 25.— The  $V_o$  vs. spectral type HR diagram for  $\chi$  Persei illustrating the region within which we identify spectroscopic members. As described in the text, the boundaries of the locus identifying members (dashed lines) is determined from the dispersion in  $E(B-V)$ , the physical size of the h and  $\chi$  Per region, binarity, and uncertainties in spectral types.

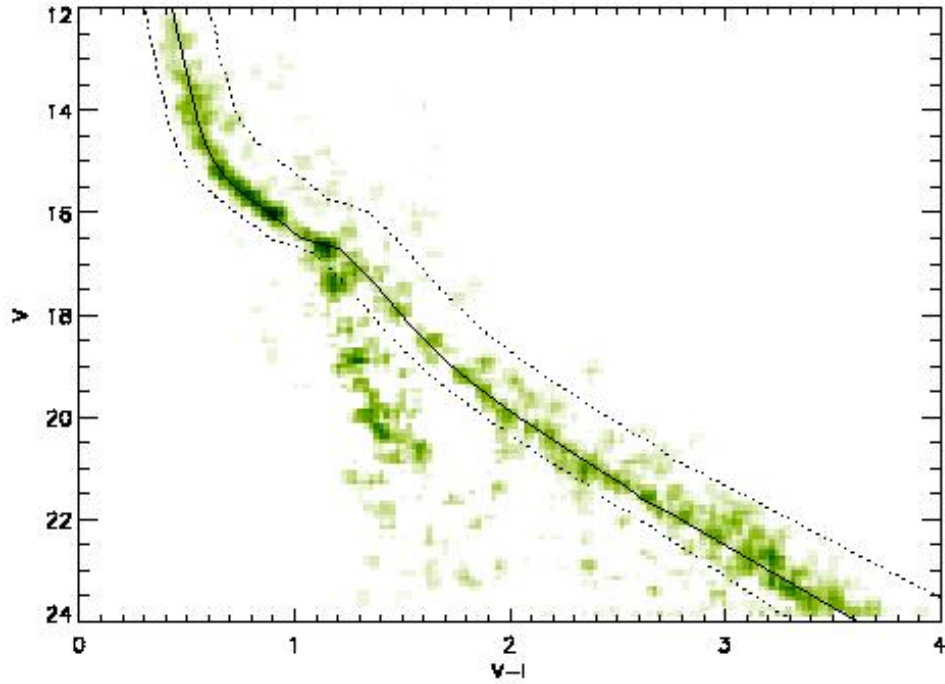


Fig. 26.— Plot of the Hess diagram for  $\chi$  Persei from Figure 20 now illustrating the range of colors and magnitudes identifying candidate members. As described in the text, the boundaries of the locus identifying members (dashed lines) is determined from the dispersion in reddening, binarity, and photometric errors.

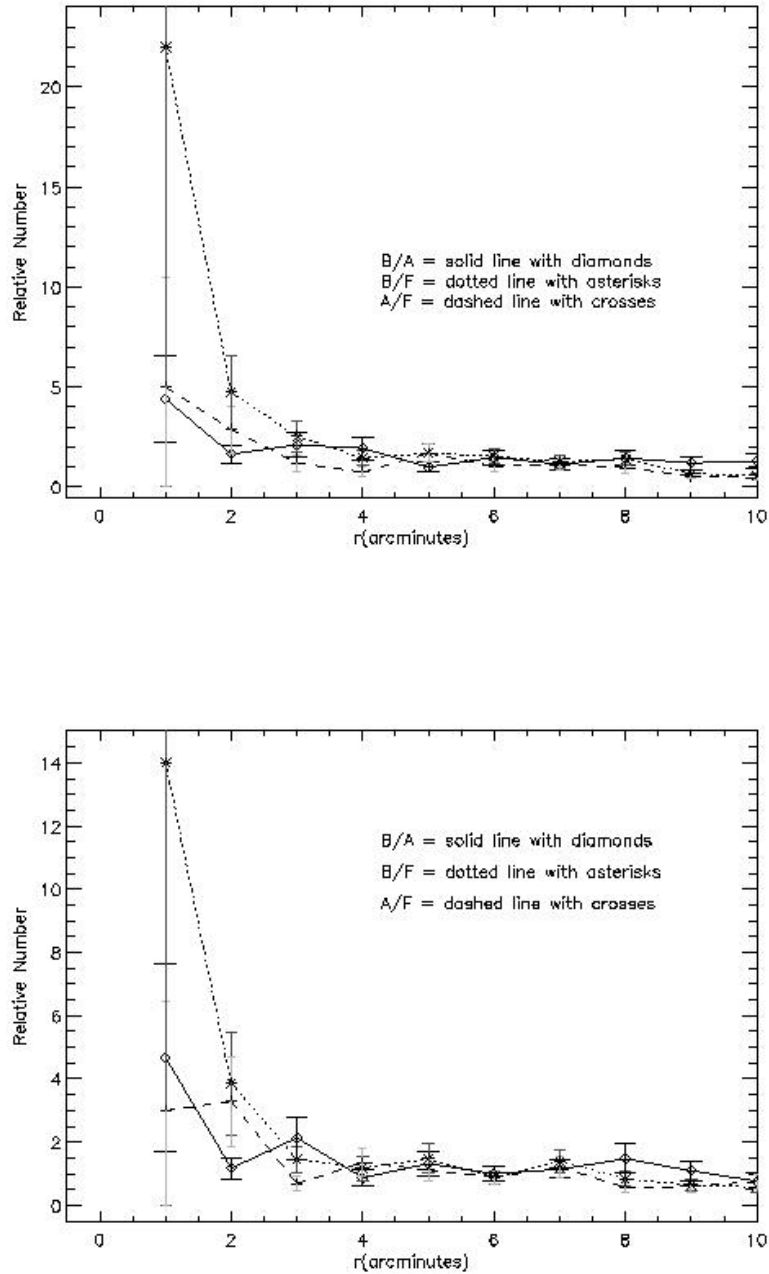


Fig. 27.— The ratio of B to A, B to F, and A to F stars versus distance from the cluster center for  $h$  Persei (top) and  $\chi$  Persei (bottom) illustrating mass segregation in both clusters. In both plots, the wide, black error bars denote the uncertainty in the ratio of B to A stars, the medium-sized grey error bars identify the B to F star ratio, and the narrow light-grey error bars identify the A to F star ratio.

of Bessell et al.’s scale is in a IAU conference proceedings paper, Crowther (1997). Figure 1 of Crowther (1997) shows that its temperature scale is systematically higher for B0.5–B2 stars than other references listed as well as older scales from Schmidt-Kaler (1982) and Bohm-Vitense (1981). Moreover, the B0.5–B1.5 scale from Humphreys and McElroy (1984), De Jager and Nieuwenhuijzen (1987), Gray and Corbally (2009), and Gray and Corbally (1994) agree against Crowther (1997) by *nearly identical amounts*.

Given this information, we adopt the scale from Humphreys and McElroy (1984) sampling in spectral type from B0.2 to B1.5. Similarly for B3 stars, all authors except for Gray and Corbally (2009) agree. In this case, we adopt the values from Humphreys and McElroy (1984) and Kenyon and Hartmann (1995). For the B2 spectral type, there appears to be complete disagreement with two primary references (Bessell et al. 1998 and Kenyon and Hartmann 1995) listing hot temperatures ( $\sim 21700$  K) and two listing cooler temperatures ( $\sim 19500$ – $19700$  K; Gray and Corbally 2009 and Humphreys and McElroy 1984). The average of these values is  $\approx 20700$  K, which is also very close to the value given by De Jager and Nieuwenhuijzen (1987) so we adopt it.

The temperature scale for B4–A0 stars shows strong agreement between various authors. We simply adopt a scale from Gray and Corbally (2009), Bessell et al. (1998), and Kenyon and Hartmann (1995) for these spectral types, taking the Kenyon and Hartmann (1995) value by default unless the other two disagree against Kenyon and Hartmann (1995) by more than several 100 K.

For dwarf stars later than A0, only three of our primary references have published values: Gray and Corbally (2009), Kenyon and Hartmann (1995), and De Jager and Nieuwenhuijzen (1987). With the exception of A5–A7 stars, these references show excellent agreement. We adopt the Gray and Corbally (2009) values by default and add the Kenyon and Hartmann (1995) for spectral types where Gray and Corbally (2009) lacks entries.

## A.2. Giants and Supergiants

As with the dwarf star  $T_e$  scale, we adopt results from Massey et al. (2005) for all O5–B0 giants and supergiants. For B1–M0 stars, the primary references listing  $T_e$  vs. spectral type for evolved stars are De Jager and Nieuwenhuijzen (1987), Humphreys and McElroy (1984), and Gray and Corbally (2009). The references show good agreement for stars later than  $\sim$  B4; small disagreements again show up in the B1–B3 range. For these stars we adopt the middle value if all three references disagree and the more frequent value if two of the three agree against the third.

The  $T_e$  scale for M supergiants is notoriously hard to calibrate: values from different authors often wildly disagree. To complicate matters, most  $T_e$  scales yield red supergiant that are far redder than post-main sequence isochrones would allow, preventing the stars’ luminosities and colors from being used to estimate cluster ages. The most recent calibrations from Levesque et al. (2005) substantially revise the temperature scale upward; the post-main sequence isochrones easily extend to these new temperatures. Even though we do not consider Levesque et al. (2005) to be a primary reference, we adopt their  $T_e$  scale for M supergiants almost verbatim for several reasons. First, the data are drawn from high signal-to-noise spectrophotometry of galactic supergiants and compared to the NMARCS stellar atmosphere models, which we consider to be robust. Second, the lead author (R. Humphreys) of the primary reference for the  $T_e$  scale that Levesque et al.’s replaces refereed the latter paper, which increases our confidence that Levesque’s scale is an improvement. Where Levesque et al. (2005)’s sampling becomes sparser (e.g. earlier than M0), we adopt the values listed in Gray and Corbally (2009), which is are drawn from other recent work whose calibration agrees with Levesque et al. (2005)’s where they overlap.

In Tables , we list our entire  $T_e$  scale along with the Johnson-Cousins-Glass colors drawn from the sources discussed in Section 2. We consider this Table to be an updated and more expansive version of similar tables presented by other authors (e.g. Kenyon and Hartmann 1995; Bessell 1990; Bessell and Brett 1988; Bessell et al. 1998; Bessell 1979; De Jager and Nieuwenhuijzen 1987; Humphreys and McElroy 1984; Gray and Corbally 2009).

### A.3. Further Discussion

Though our  $T_e$  scale is not drawn from a uniform sample, we consider it to be robust as it is less susceptible to small measurement errors or biases unique to a given paper. Moreover, we can identify general trends in different authors’  $T_e$  calibrations by comparing their results to our table. For example, where we determine Gray and Corbally (2009) to be less accurate, they always predicts cooler temperatures than the ones we adopt; when Bessell et al. (1998) is the outlier they almost always predicts hotter temperatures. Interestingly, De Jager and Nieuwenhuijzen (1987) appears to be the most accurate source as the majority of other references almost never disagree against it.

Our adopted scales slightly differ from that from Slesnick et al. (2002). Slesnick et al. (2002) used Kilian et al. (1992) for all stars earlier than B3 and Humphreys and McElroy (1984) for everything else, a scale that yields higher temperatures for early B stars. If we adopt the calibration used by Slesnick et al. (2002), our derived reddening is slightly higher and MS turnoff ages are younger by  $\approx 1$  Myr. However, adopting this calibration lead to

a very slight but perceptible systematic offset in the dereddened V vs. V-J,H, K and V vs. spectral type loci of cluster stars. It also may induce a small but systematic shift in reddening for B0–B3 stars compared to later-type stars.

Recent studies determining effective temperatures for individual B stars from stellar atmosphere modeling indicates that our cooler  $T_e$  scale is more accurate. In particular, more recent non-LTE stellar atmosphere modeling by Crowther, the source of the hotter  $T_e$  scale for evolved stars used in Bessell et al. (1998), revises the  $T_e$  for supergiants downwards to almost complete agreement with our adopted scale (Crowther et al. 2006). The only clear systematic difference between our two scales is that Crowther et al.’s temperatures for B0.5–B1I supergiants are  $\sim 2000$ – $2500$  K hotter than our entries. The temperatures are already very hot ( $\sim 25000$  K). Our sample includes only 7 supergiants with spectral types between B0.4 and B1: B1.5–B3 supergiants are far more frequent. Therefore, if Crowther’s scale is more correct the disagreement should have only a minimal impact on our analysis.

Other recent determinations for less evolved stars support our adopted scale. Specifically, Fitzpatrick and Massa (2005) determined fundamental parameters – e.g.  $T_e$ ,  $[m/H]$ ,  $R/R_\odot$ , and  $\log(g)$  – for galactic B and early A dwarfs and giants. Their derived temperatures for early B stars agree with our adopted scale against the determinations adopted by Slesnick et al. (2002). If anything, our scale is still too hot for B3 V stars by  $\approx 1000$  K. In summary, we consider our  $T_e$  scale to be a slight improvement over Slesnick et al. (2002)’s, though they used the best available scale at the time, which can clearly yield good estimates for  $h$  and  $\chi$  Per properties.

## **B. The metallicity of $h$ and $\chi$ Persei: Previous Estimates, Uncertainties, and Its Effect on Distance Moduli and Stellar Ages**

There is significant disagreement over the clusters’ metallicities in the literature. Some authors find that  $h$  and  $\chi$  Per stars have a solar metallicity (e.g. Dufton et al. 1990; Smartt and Rolleston 1997), while others finding a subsolar metallicity ( $Z = 0.01$  Southworth et al. 2004a,b). The Southworth et al. (2004a) results present a challenge to our assumption that  $h$  and  $\chi$  Persei have a near-solar metallicity, and we now directly address this issue by explaining why a near-solar metallicity ( $Z = 0.019$ ) is more likely than a subsolar one ( $Z = 0.01$ ).

Southworth et al. (2004a) and Southworth et al. (2004b) derive the metallicity for two  $h$  Persei eclipsing binary systems, V615 Per and V618 Per, and one  $\chi$  Persei star (V621 Per) by comparing the derived masses and radii for each binary component with predictions from Granada isochrones (Claret 1995). However, comparisons with the Padova isochrone

predictions yield a metallicity for 2 of the 4 h Persei stars that is slightly higher than  $Z=0.01$ . Venn et al. (2002) find that V621 Per has a nearly solar abundance of metals. In support of their conclusion that h and  $\chi$  Persei have a subsolar metallicity, Southworth et al. cites non-LTE modeling of B giants/supergiants by Vrancken et al. (2000), which yield similar results. However, Vrancken et al. (2000) note that non-LTE modeling of evolved B stars *systematically* yield low metallicities: it is not clear whether whether this difference is physical or whether it reflects uncertainties in the modeling assumptions.

The most convincing argument that h and  $\chi$  Persei stars typically have a near-solar metallicity comes from analyzing the colors and luminosities of their M supergiants. Figure 28 shows  $V$  vs.  $\log(T_e)$  and  $V$  vs.  $V-J$  diagrams for  $Z=0.01$  isochrones. The best-fit distance moduli are systematically smaller by  $\approx 0.25$  mags and range from 11.55 for h Persei to 11.60 for  $\chi$  Persei and the halo population (Figure 29). As the Figure 28 panels clearly show, subsolar metallicity isochrones are unable to produce M supergiants with observed red  $V-J$  colors and inferred cool effective temperatures. In particular, *none* of the subsolar metallicity isochrones are able to reproduce the observed effective temperatures of most M supergiants. The  $V-J$  colors of at least two and perhaps four M supergiants are too red for the isochrones by up to 1.5 magnitudes. In contrast, the solar metallicity isochrones are clearly able to produce stars with these properties. Based on these comparisons, h and  $\chi$  Persei is unlikely to have a substantially subsolar metallicity.

Even if h and  $\chi$  Per did have  $Z \sim 0.01$  as argued by Southworth et al. (2004a), the resulting changes in age estimates are small. As can be inferred from Figure 28, even the  $Z = 0.01$  isochrones show that h and  $\chi$  Persei’s main sequence turnoff age is clearly older than 10 Myr and younger than 20 Myr. In fact, the best-fit turnoff age is only  $\approx 1-2$  Myr greater because the overall lower luminosity of metal-poor stars is partially offset by their smaller distance moduli. Thus, the systematic errors in age due to h and  $\chi$  Persei’s metallicity are  $\lesssim 10\%$  of the clusters’ ages.

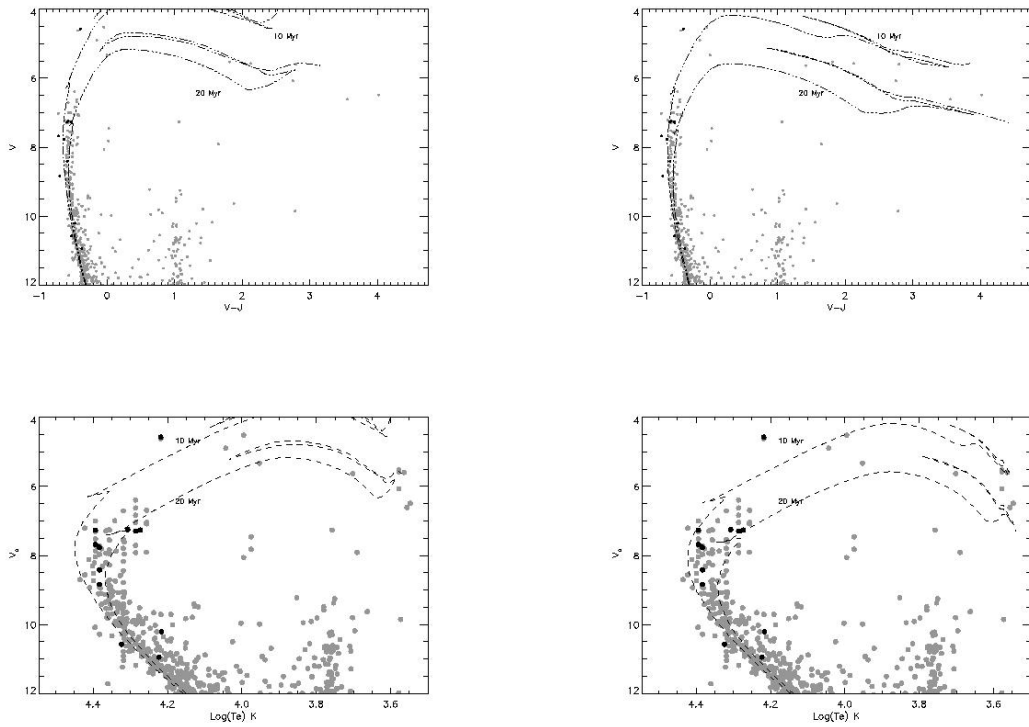


Fig. 28.— V vs. V- J (top panels) and V vs.  $\log(T_e)$  (bottom panels) diagrams for all stars with spectra and V band photometry, illustrating how subsolar metallicity (left panels) and solar metallicity (right panels) isochrones compare to the colors and temperatures of red supergiants.

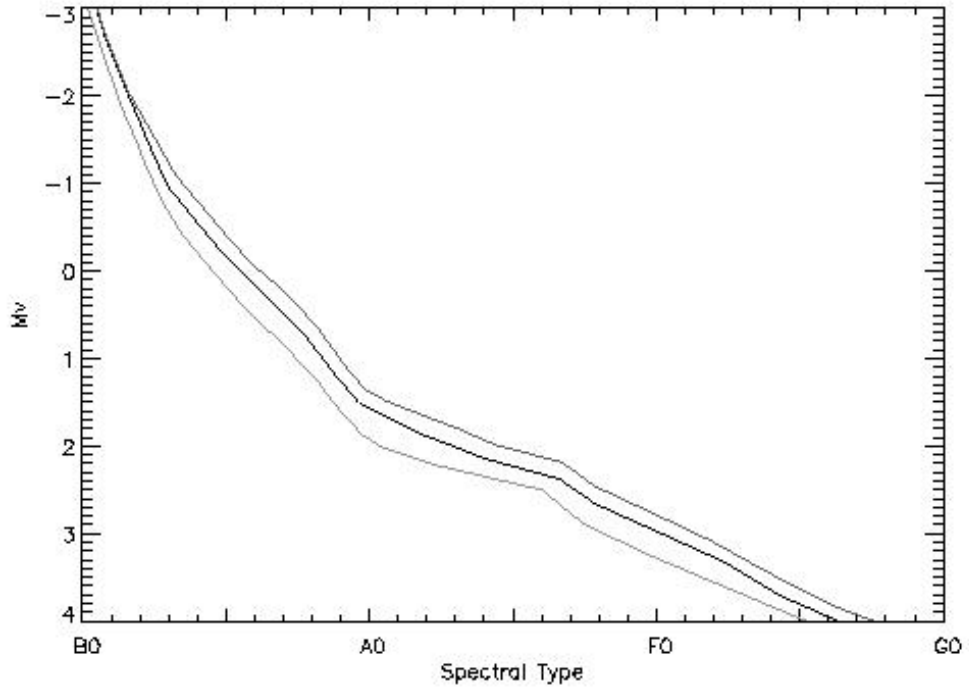


Fig. 29.— Comparison between Padova isochrones with a subsolar, solar, and supersolar metallicity. In order for the main sequence to line up, the distance modulus for the subsolar metallicity isochrone must be decreased by 0.25 mags.